

# **Pulse sequences for multi-frequency selective NMR excitation in inhomogeneous magnetic fields**

by

Gabriel Seyoum, B. Eng

A thesis submitted to the Faculty of Graduate and Postdoctoral Affairs

in partial fulfillment of the requirements for the degree of  
**Master of Applied Science in Biomedical Engineering**

Ottawa-Carleton Institute for Biomedical Engineering (OCIBE)

Department of Systems and Computer Engineering

Carleton University

Ottawa, Ontario, Canada, K1S 5B6

September 2011

© Copyright 2011, Gabriel Seyoum



Library and Archives  
Canada

Published Heritage  
Branch

395 Wellington Street  
Ottawa ON K1A 0N4  
Canada

Bibliothèque et  
Archives Canada

Direction du  
Patrimoine de l'édition

395, rue Wellington  
Ottawa ON K1A 0N4  
Canada

*Your file* *Votre référence*  
*ISBN: 978-0-494-83121-2*  
*Our file* *Notre référence*  
*ISBN: 978-0-494-83121-2*

**NOTICE:**

The author has granted a non-exclusive license allowing Library and Archives Canada to reproduce, publish, archive, preserve, conserve, communicate to the public by telecommunication or on the Internet, loan, distribute and sell theses worldwide, for commercial or non-commercial purposes, in microform, paper, electronic and/or any other formats.

The author retains copyright ownership and moral rights in this thesis. Neither the thesis nor substantial extracts from it may be printed or otherwise reproduced without the author's permission.

**AVIS:**

L'auteur a accordé une licence non exclusive permettant à la Bibliothèque et Archives Canada de reproduire, publier, archiver, sauvegarder, conserver, transmettre au public par télécommunication ou par l'Internet, prêter, distribuer et vendre des thèses partout dans le monde, à des fins commerciales ou autres, sur support microforme, papier, électronique et/ou autres formats.

L'auteur conserve la propriété du droit d'auteur et des droits moraux qui protège cette thèse. Ni la thèse ni des extraits substantiels de celle-ci ne doivent être imprimés ou autrement reproduits sans son autorisation.

---

In compliance with the Canadian Privacy Act some supporting forms may have been removed from this thesis.

While these forms may be included in the document page count, their removal does not represent any loss of content from the thesis.

Conformément à la loi canadienne sur la protection de la vie privée, quelques formulaires secondaires ont été enlevés de cette thèse.

Bien que ces formulaires aient inclus dans la pagination, il n'y aura aucun contenu manquant.

  
**Canada**

The undersigned recommend to  
the Faculty of Graduate and Postdoctoral Affairs  
acceptance of the thesis

**Pulse sequences for multi-frequency selective NMR  
excitation in inhomogeneous magnetic fields**

Submitted by

Gabriel Seyoum, B. Eng

In partial fulfillment of the requirements for  
the degree of Master of Applied Science in Biomedical Engineering

---

Chair, Dr. Howard Schwartz, Department of Systems and Computer Engineering

---

Thesis Supervisor, Dr. Andrew E. Marble

Carleton University  
September 2011

## Abstract

The aim of this thesis is to investigate pulse sequences to improve spatial and spectral selectivity of a single pixel magnetic resonance scanner. The conventional Magnetic Resonance Imaging (MRI) scanners are expensive, bulky, places restrictions on sample geometry and as such are not widely applicable. An alternative is portable, single sided Nuclear Magnetic Resonance (NMR), in which open access single sided magnet design have reduced system cost and complexity. These types of devices can be employed for non-destructive testing of various small and bulky materials. The challenge of using this type of system is the presence of inhomogeneous magnetic field which obscures measurement information. This thesis proposes experimental techniques to improve the Signal to Noise Ratio (SNR) of this Single Pixel Scanner (SPS) so that the measurement results represent progress towards those of traditional scanners. This thesis introduces a pulse sequence for multi-frequency selective NMR excitation in inhomogeneous fields. In this pulse sequence, the composite pulse Radio Frequency (RF) envelope contains many superimposed sinusoids each exciting a pair of narrow signal spectra at a specific frequency. These spectra are then phase corrected, and co-added to enhance SNR of the SPS. This novel method can be applied in NMR spectroscopy to help observe time dependent phenomenon such as diffusion, which would otherwise be obscured when using this type of hardware.

## **Acknowledgements**

I would like to express my sincere gratitude to my supervisor Dr. Andrew E. Marble, professor in the Department of Systems and Computer Engineering at Carleton University who has supported me throughout my thesis with his patience, guidance, enthusiasm, and immense knowledge. I dedicate this work to the following people: my late father, who instilled in me the importance of obtaining higher education; to Angela and my children John and Michael who inspired me to obtain a Master's degree in Engineering; and to my mother, brothers and sisters who supported me to pursue graduate studies at Carleton University.

# Table of Contents

Abstract.....	iii
Acknowledgements.....	iv
Table of Contents.....	v
List of Tables.....	vii
List of Figures.....	viii
List of Abbreviations.....	x
List of Symbols.....	xi
Chapter 1.0 Introduction.....	1
1.1 Problem statement.....	1
1.2 Thesis contribution.....	2
1.3 Thesis organization.....	2
Chapter 2.0 Background on NMR.....	3
2.1 Excitation and the Bloch equation.....	9
2.2 Relaxation.....	10
2.2.1 T1 relaxation.....	10
2.2.2 T2 relaxation.....	11
2.3 NMR pulse sequences.....	13
2.4 Diffusion.....	16
2.5 Imaging.....	18
2.6 Parameters that affect the NMR signal quality.....	19
2.6.1 NMR scans.....	20
2.6.2 Phase cycling.....	20
2.6.3 Multi-echo averaging.....	20
2.7 Spectral resolution.....	21
2.8 MR hardware.....	23
2.8.1 Conventional.....	24
2.8.2 Single sided MR hardware.....	26
2.9 MR in inhomogeneous magnetic fields.....	27
2.9.1 Mobile single sided NMR.....	28
2.9.2 Selective excitation.....	29
Chapter 3.0 Hardware design for single sided NMR.....	32
3.1 Magnet designs for SPS.....	35
3.1.1 Relatively homogenous field magnets.....	38

3.2 Probe and transmitter-receiver unit.....	41
3.2.1 Probe.....	42
3.2.2 Transmitter-receiver protection circuitry.....	43
3.3 Linear positioning system.....	46
3.3.1 Linear motion system components.....	46
3.3.2 Motion controller.....	47
3.4 NMR measurement calibration.....	48
3.5 Observing NMR signal.....	48
3.6 Finding the gradient of homogeneous field magnets.....	51
3.7 Pulse width effects.....	53
Chapter 4.0 Experimental results.....	55
4.1 Imaging.....	56
4.1.1 Finding spatial resolution of homogeneous field magnets.....	60
4.2 Spectral resolution.....	63
4.2.1 NMR excitation by multi-frequency selective pulse.....	63
4.2.2 Graphical illustration of frequency shifted NMR excitation...	65
4.2.3 Phase correction of NMR spectra.....	68
4.2.4 Experimental results of single frequency excitation.....	73
4.2.5 Experimental results of multi-frequency excitation.....	75
4.2.6 Measuring diffusion with multi-frequency selective pulse.....	94
Chapter 5.0 Conclusions and future work.....	96
5.1 Conclusions.....	96
5.2 Future work.....	97
References.....	99

## List of Tables

4.0	Spatial resolution for various RF pulse widths.....	61
4.1	Single frequency excitation: Maximum signal intensity data.....	93
4.2	Multi-frequency excitation: Maximum signal intensities data.....	93

## List of Figures

2.0	The Zeeman diagram.....	5
2.1	Net equilibrium magnetization aligned with $\bar{B}_0$ field.....	7
2.2	Motion of a magnetic dipole under the influence of magnetic field.....	8
2.3	Precessional motion around the effective magnetic field.....	10
2.4	The return of z magnetization component.....	11
2.5	Signal decay due to $T_2$ relaxation.....	12
2.6	NMR system response.....	13
2.7	A simple pulse sequence.....	14
2.8	Spin echo.....	15
2.9	CPMG spin echoes and the $T_2$ envelope.....	15
2.10	$^1\text{H}$ NMR spectrum of Acetaldehyde.....	22
2.11	Conventional MR hardware block diagram.....	24
2.12	The RF path.....	26
2.13	Single sided MR hardware block diagram.....	27
2.14	RF pulse width effect on excitation.....	30
3.0	The complete hardware setup of SPS.....	33
3.1	NMR Spectrometer.....	34
3.2	Lakeshore 460 3-channel Gaussmeter.....	34
3.3	Magnets arrangement for SPS.....	35
3.4	1D magnetic field profiles of SPS.....	36-37
3.5	The whole width 2D magnetic field profile of SPS.....	38
3.6	1D field profile and the sensitive volume.....	39
3.7	2D profile of relatively homogeneous field magnets.....	40-41
3.8	The probe.....	42
3.9	NMR probe circuit diagram.....	43
3.10	SPS's transmitter-receiver unit.....	44
3.11	The transmitter-receiver protection circuitry.....	45
3.12	The $\lambda/4$ circuit.....	45
3.13	Linear motion system.....	47
3.14	Motion controller.....	47
3.15	$\bar{B}_0$ field mapping software.....	48
3.16	Measurement setup using relatively homogeneous field magnets.....	49
3.17	The CPMG of mineral oil sample.....	49
3.18	Mineral oil signal after ensemble averaging.....	50
3.19	Mineral oil magnitude plot after ensemble averaging.....	51
3.20	Diffusion measurement of water.....	52
3.21	The excitation profile of SPS.....	54
4.0	The ideal, expected edge response plot and 1D continuous scan.....	55
4.1	Contours corresponding to two different pulse lengths.....	56
4.2	The not best fitted edge response curves.....	57
4.3	Mineral oil edge response best fit curves.....	58-59
4.4	Mineral oil edge response best fit curves put together.....	59

4.5	Point Spread Function of 64 $\mu$ s pulse.....	61
4.6	The plot of spatial resolution versus pulse length.....	62
4.7	Illustration of multi-frequency selective NMR excitation.....	64
4.8	The rectangular RF pulse.....	65
4.9	Message transmission through variations in the carrier's amplitude.....	66
4.10	Convolving the rectangular function with a cosine carrier signal.....	67
4.11	NMR excitation by frequency shifts when $n = 1$ .....	67
4.12	Total spectra of NMR excitation by frequency shifts.....	68
4.13	Relationship between FID and the phase of a signal.....	69
4.14	Phase errors in NMR spectra.....	69
4.15	An echo evoked by single frequency rectangular RF pulse excitation.....	73
4.16	The spectrum of single frequency excitation.....	74
4.17	Single frequency excitation magnitude plot.....	74
4.18	Simulation result: The 3-frequency excitation.....	77
4.19	Experimental result: The 3-frequency phase adjusted echo.....	78
4.20	Experimental result: The 3-frequency not phase corrected spectra.....	78
4.21	Experimental result: The 3-frequency phase corrected spectra.....	79
4.22	Experimental result: Three spectra co-added.....	79
4.23	Simulation result: The 7-frequency excitation.....	80
4.24	Experimental result: The 7-frequency phase adjusted echo.....	81
4.25	Experimental result: The 7-frequency not phase corrected spectra.....	81
4.26	Experimental result: The 7-frequency phase corrected spectra.....	82
4.27	Experimental result: Seven spectra co-added.....	82
4.28	Simulation result: The 15-frequency excitation.....	83
4.29	Experimental result: The 15-frequency phase adjusted echo.....	84
4.30	Experimental result: The 15-frequency not phase corrected spectra.....	84
4.31	Experimental result: The 15-frequency phase corrected spectra.....	85
4.32	Experimental result: Fifteen spectra co-added.....	85
4.33	Simulation result: The 31-frequency excitation.....	86
4.34	Experimental result: The 31-frequency phase adjusted echo.....	87
4.35	Experimental result: The 31-frequency not phase corrected spectra.....	87
4.36	Experimental result: The 31-frequency phase corrected spectra.....	88
4.37	Experimental result: Thirty-one spectra co-added.....	88
4.38	Simulation result: The 63-frequency excitation.....	89
4.39	Experimental result: The 63-frequency phase adjusted echo.....	90
4.40	Observing Hahn echoes with multi-frequency pulse sequence.....	90
4.41	Experimental result: The 63-frequency not phase corrected spectra.....	91
4.42	Experimental result: The 31-frequency phase corrected spectra.....	91
4.43	Experimental result: Sixty-three spectra co-added.....	92
4.44	Maximum signal intensity versus number of frequencies excited.....	93
4.45	Spectral broadening due to diffusion.....	94

## List of Acronyms

ADC	Analog Digital Converter
AM	Amplitude Modulation
BNC	Bayonet Neill Concelman
CP	Carr Purcell
CPMG	Carr Purcell Meiboom Gill
DANTE	Delays Alternating with Nutations for Tailored Excitation
FID	Free Induction Decay
EMF	Electromotive Force
FT	Fourier Transform
FWHM	Full Width Half Maximum
GUI	Graphical User Interface
MOUSE	Mobile Universal Surface Explorer
MR	Magnetic Resonance
MRI	Magnetic Resonance Imaging
NdFeB	Neodymium Iron Boron
NMR	Nuclear Magnetic Resonance
PC	Personal computer
PSF	Point Spread Function
PGSE	Pulsed Gradient Spin Echo
RF	Radio Frequency
SGSE	Steady-Gradient Spin-Echo
SGSTE	Steady-Gradient Stimulated-Echo
SNR	Signal-to-Noise Ratio
SPS	Single Pixel Scanner
STE	Standard Stimulated Echo
STRAFI	Stray Field Imaging

## List of Symbols

$A_r, A_m, A_c$	Amplitude of rectangular pulse, message, and carrier signals
$\vec{B}_0$	Static Field
$\vec{B}_1$	RF magnetic field
$\vec{B}_{\text{eff}}$	Effective magnetic field
$\vec{B}$	Total magnetic field
$\Delta\vec{B}_0$	Local field offset
$c(t)$	Carrier signal
$C$	Capacitance
$\text{CH}_3\text{CHO}$	Acetaldehyde
$\text{C}_2\text{H}_6\text{OH}$	Ethanol
$D$	Diffusion coefficient
$1\text{D}, 2\text{D}$	One, two dimensional
$\Delta E$	Energy gap between two quantum states
$f_m$	Frequency of the message signal
$\Delta f$	Frequency spacing
$\varphi_{ij}$	Phase correction angle
$\vec{G}$	Gradient magnetic field
$\text{H}_z$	Hertz
$\rho$	Spin density
$\Gamma$	FWHM
$\hbar$	Plank constant
$^1\text{H}$	Hydrogen
$\hat{i}, \hat{j}, \hat{k}$	Unit vectors in x, y, z direction
$I$	Measured intensity
$I_0$	Maximum peak intensity
$\vec{J}$	Angular momentum
$K$	Boltzmann constant
$k_x$	Reciprocal space vector
$L$	Inductance
$m(t)$	Message signal
$\vec{M}$	Magnetization
$\vec{M}_x, \vec{M}_y, \vec{M}_z$	x, y, and z components of magnetization
$\vec{M}_0$	Initial magnetization
$N$	Total number of spins
$n$	Spectrum data points
$N_\uparrow$	Number of nuclei that are pointing up

$N_{\downarrow}$	Number of nuclei that are pointing down
$q_{\text{num}}$	Quantum number
$\theta$	Flip angle
$\delta_1$	Chemical shift
$\gamma$	Gyromagnetic ratio
$\lambda / 4$	Quarter wave length
$\Omega$	Ohm
$S(t)$	NMR signal
$\vec{\tau}$	Torque
$\tau$	Time
$T$	Tesla
$T_{\text{emp}}$	Temperature
$T_{\text{inh}}$	Decay time due to inhomogeneity
$T_1$	Longitudinal relaxation
$T_2, T_2^*$	Transversal relaxation
$t_p$	Pulse length
$\vec{\mu}$	Magnetic dipole moment
$V$	Volt
$\omega$	Angular frequency
$\omega_1$	Radio frequency
$\omega_0, \nu_0, f_0$	Larmor frequency
$\omega_{\text{oscillation}}$	Frequency of oscillation
$\omega_s$	Offset frequency
$y(t)$	Amplitude modulated signal
$Z_T$	Effective input impedance

# Chapter 1.0 Introduction

There have been growing interests in MR (Magnetic Resonance) machines that operate in low magnetic field. Traditional Magnetic Resonance Imaging (MRI) scanners are quite expensive and bulky as such not widely applicable. An emerging alternative is portable, single sided Nuclear Magnetic Resonance (NMR), in which open access single sided magnet design have reduced system cost and complexity. In this thesis, a unilateral magnet array is assembled from three permanent magnets to create a static magnetic field suitable for bulk or 'single pixel' MR measurements. This type of device is suitable for non-destructive testing of small as well as bulky objects. Unlike conventional magnetic resonance hardware, the single pixel scanner generates a grossly inhomogeneous static magnetic field, which obscures sample information in the measurements when standard pulse sequences are used. This thesis investigates Nuclear NMR pulse sequences for use in the inhomogeneous field of this instrument.

## 1.1 Problem statement

Magnetic resonance measurement quality can be determined by spatial resolution in MR imaging and spectral resolution in NMR spectroscopy. Both of these resolutions are affected by the homogeneity of the static magnetic field  $\vec{B}_0$  generated by the hardware. A second factor affecting these qualities is the character of the Radio Frequency (RF) pulses used to elicit a signal from the sample under study. The goal of this thesis is to investigate pulse sequences which (a) improve spatial selectivity and (b) improve spectral selectivity of a Single Pixel Scanner (SPS).

## **1.2 Thesis contributions**

The major contribution of this thesis is developing a pulse sequence for multi-frequency selective NMR excitation. In frequency shifted excitation, the RF pulse envelope is modulated sinusoidally by shifting its frequency allowing excitation of narrow spectra at specific frequency. The multi-frequency selective composite RF pulse is introduced which contains many superimposed sinusoids where each selects a pair of narrow spectra excitation at specific frequency. The individual spectra are noisy, due to the inhomogeneity of the instrument's static field. These spectra are phase corrected, and co-added to enhance the Signal to Noise Ratio (SNR) of single sided NMR system leading to measurement results that represent progress towards those of traditional scanners. This thesis also exhibits the effect of RF pulse width increase on spatial resolution when the scanner is used for imaging applications; it is demonstrated that high resolution MR imaging is possible using long duration RF pulse.

## **1.3 Thesis organization**

Chapter 2.0 introduces background on NMR phenomenon such as excitation, relaxation, diffusion, and chemical shift including some of the most common pulse sequences. The major differences between SPS and the conventional MR hardware are examined in details. The multi-echo averaging and MR imaging principles are also presented here. Furthermore, this section briefly introduces Stray Field Imaging (STRAFI) and the first mobile NMR device called the Mobile Universal Surface Explorer (MOUSE). Finally, it goes on to present literature review on selective excitation in inhomogeneous magnetic fields.

Chapter 3.0 investigates the hardware components of SPS; it also examines the design and construction of NMR probe and quarter wavelength protection circuitry. The magnetic field profiles of SPS have been analyzed extensively in order to maximize the field homogeneity of the scanner used. This section includes system calibration, observing spin echoes of mineral oil sample, mapping the excitation profile of SPS, and finding the gradient of homogeneous field magnets.

Chapter 4.0 defines theories of multi-frequency selective NMR excitation, phase correction of NMR spectra and high resolution MR imaging. Various graphical analogies and equations have been utilized to describe the postulates of these methods. It also provides all the experimental results. The imaging procedure proved the suitability of SPS for high resolution imaging. The experimental results that are obtained through the use of rectangular and multi-frequency composite pulse has been compared to determine which method provides a higher SNR. Moreover, the multi-frequency selective pulse sequence was employed to analyze spectra broadening due to diffusion.

Chapter 5.0 summarizes the main points of the thesis, and outlines some useful recommendations. This section also discusses the application of the proposed techniques and its limitations.

## **Chapter 2.0 Background on NMR**

NMR is the study of magnetic properties of atomic nuclei. NMR spectroscopy allows non-invasive microscopic analysis of liquids and solids and it has become a standard tool in many areas such as biomedical imaging, materials studies, and for analyzing the structural properties of various molecules. The conventional MR imaging device has several advantages compared to other imaging methods: no ionizing radiation,

non-invasive, and great contrast resolution for distinguishing adjacent soft tissues. The first measurements of the proton magnetic moment were conducted by Estermann, Frish and Stern in 1932 followed by a confirming experiment in 1937 [1]. In 1937 Isidor Rabi first described and measured NMR in molecular beams [2]. In 1946 Felix Bloch and Edward Purcell independently developed NMR techniques for use on liquids and solids [3, 4]. Shaw and Elskens in 1950 used proton NMR to investigate the water content of vegetable materials [5] and Odebold and Lindstrom in 1955 obtained proton NMR signals from a number of mammalian samples [6]. Ernest Anderson in 1966 introduced pulsed NMR in combination with Fourier Transform (FT) [7]; this technique is the foundation of most modern NMR experiments. In 1971 Raymond Damadian demonstrated a technique using NMR to distinguish between tumors and healthy tissue [8]. In 1973 Lauterbur was able to reconstruct an image from test tubes of water using filtered back-projection [9]. Mansfield and Grannell were also recognized in 1973 for reconstructing an image from interleaved layers of camphor and cardboard [10].

Certain atomic nuclei, when polarized in an external static magnetic field, have a range of discrete energy levels, and can absorb and emit electromagnetic radiation with a frequency corresponding to the energy difference between these levels. Hydrogen atom is a primary choice for MR imaging, since the human body contains high concentration of it and the image contrast comes most often from the degree of water mobility. Furthermore, hydrogen is the most sensitive naturally occurring nucleus to magnetic resonance.

Nuclear spin quantum number ( $q_{\text{num}}$ ) is very useful for characterizing NMR behavior of atomic nuclei. For hydrogen ( $^1\text{H}$ ) which has  $q_{\text{num}} = \frac{1}{2}$  in the presence of an external magnetic field two spin states exist  $+1/2$  (spins that points along the magnetic

field direction up  $\uparrow$ ) and  $-1/2$  (down  $\downarrow$ ). Since this is a quantum phenomenon, there are no possible states in between. In the absence of an external magnetic field and at thermal equilibrium exactly one half of population of nuclei will be pointing up and the other half pointing down. NMR signal intensity is proportional to the population difference of the two states [11]. When an external magnetic field is applied, the two spin states develop corresponding energy level  $\Delta E$ . Thermal agitation causes random transitions between states and at thermal equilibrium Boltzmann distribution can be used to calculate the relative population difference at various energy levels, where  $T_{\text{emp}}$  is being the measuring temperature and  $K$  the Boltzmann constant. The  $N_{\uparrow}$ , and  $N_{\downarrow}$  represents the number of nuclei in the spin orientation.

$$\frac{N_{\uparrow}}{N_{\downarrow}} = e^{\Delta E / K T_{\text{emp}}} \quad (2.0)$$

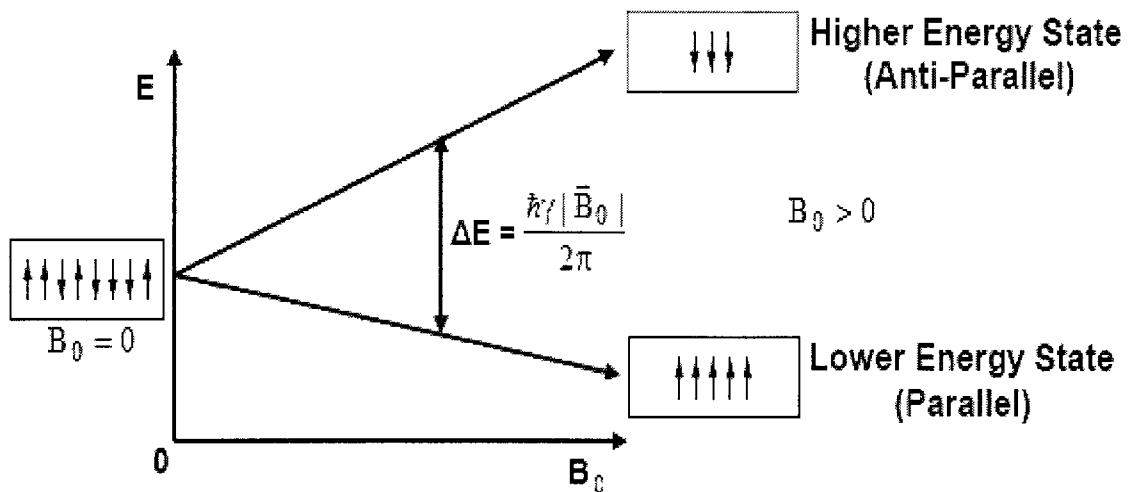


Figure 2.0: The Zeeman diagram

The energy gap between the two quantum states is proportional to the strength of the external magnetic field, and increases as the field strength is increased. Figure 2.0 is

the Zeeman diagram and it illustrates that two spin states have the same energy when the external field is zero, but diverge as the field increases. Nuclear spins can be bumped from the lower energy state to the higher by introducing a photon with the correct Larmor frequency  $\omega_0$ . In equation 2.1  $\hbar$  represents a plank's constant.

$$\Delta E = \frac{\hbar\gamma|\vec{B}_0|}{2\pi} = \hbar f_0 \quad (2.1)$$

The equation 2.0 can be rewritten as  $\frac{N_{\uparrow}}{N_{\downarrow}} = e^{\frac{\hbar\gamma|\vec{B}_0|}{2\pi}/KT_{\text{emp}}}$

The angular momentum of elementary particles is limited to discrete values [12] and is quantized and its amplitude is given by

$$|\vec{J}| = (h/2\pi)\sqrt{q_{\text{num}}(q_{\text{num}} + 1)} \quad (2.2)$$

Spinning nuclei have angular momentum  $\vec{J}$  that give rise to magnetic dipole moment  $\vec{\mu}$  and the gyromagnetic ratio  $\gamma$  is a constant for any given nuclide.

$$\vec{\mu} = \gamma\vec{J} \quad (2.3)$$

The NMR experiment measures a large ensemble of spins derived from a huge number of molecules and the net magnetic moment  $\vec{M}$  of a macroscopic sample is the sum of all individual magnetic moments  $\vec{\mu}$ . Due to the magnetic field induced population difference there is a net component of  $\vec{M}$  parallel with  $\vec{B}_0$  along the Z axis as shown in figure 2.1

$$\vec{M} = \sum_{i=1}^n \vec{\mu}_i \quad (2.4)$$

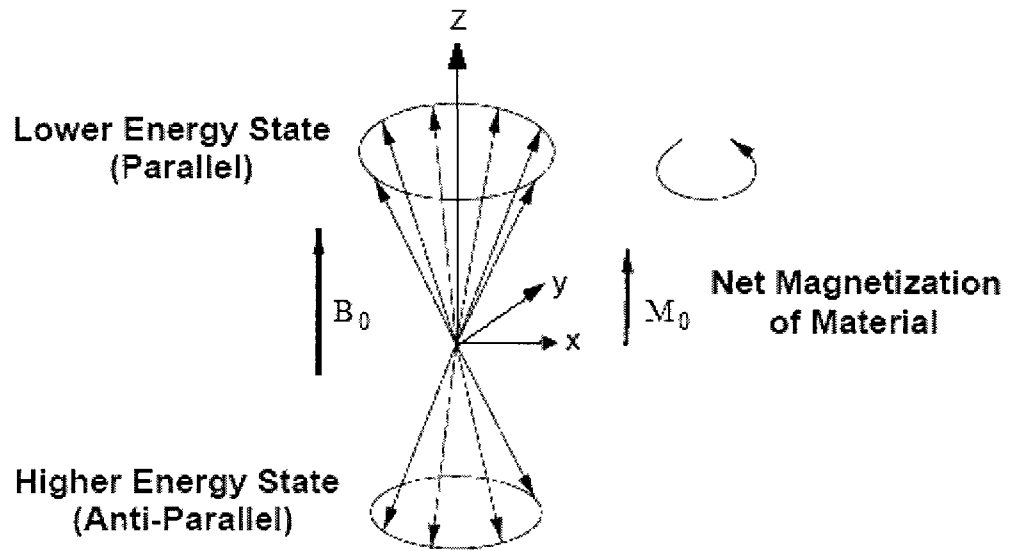


Figure 2.1: Net equilibrium magnetization aligned with  $\vec{B}_0$  field

The net magnetization  $\vec{M}$  behaves as a bar magnet. If  $\vec{M}$  is tipped away from the z-axis, the static field imposes a torque on the magnetization vector which attempts to re-align  $\vec{M}$  with z. Due to the spin angular momentum present in  $\vec{M}$ , the magnetization precesses like a spinning top, and traces a circular path about the applied magnetic field [13].

$$\vec{\tau} = \partial \vec{J} / \partial t, \quad \vec{\tau} = \vec{M} \times \vec{B}_0 \quad (2.5)$$

The effect of static magnetic field on the magnetic moment could be explained by classical mechanics which describe when force is exerted on spinning object it tends to move at right angle to the force. The precessional motion is illustrated by figure 2.2 and differential equation of 2.6; the rate of precession in equation 2.7 is known as Larmor frequency of the nucleus and it describes the resonant precessional frequency of a nuclear magnetic moment in applied static magnetic field.

$$\partial \vec{M} / \partial t = \gamma \partial \vec{J} / \partial t = \gamma \vec{\tau} = \gamma (\vec{M} \times \vec{B}_0) \quad (2.6)$$

$$\omega_0 = \gamma |\vec{B}_0| \quad (2.7)$$

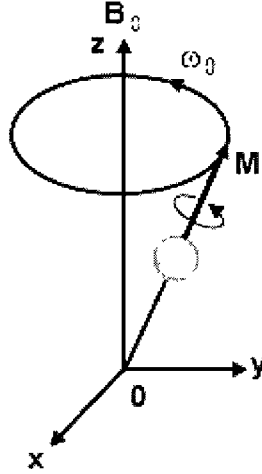


Figure 2.2: Motion of a magnetic dipole under the influence of magnetic field

At thermal equilibrium the magnitude of the longitudinal magnetization can be described by equation 2.8, where  $N$  is the total number of nuclear spins in per unit volume,  $K$  is Boltzmann constant and  $T_{\text{emp}}$  is absolute temperature.

$$\vec{M} = N \gamma^2 \hbar^2 \vec{B}_0 / 4K T_{\text{emp}} \quad (2.8)$$

Sensitivity depends on various factors such as sample volume, gyromagnetic ratio  $\gamma$ , natural abundance of nucleus under study, noise, relaxation parameters and magnetic field strength [12]. At thermal equilibrium the population difference is proportional to  $\gamma^2 |\vec{B}_0|$  and inversely proportional to absolute temperature thus higher magnetic field and lower sample temperature improves sensitivity. The rate at which magnetization precesses is also proportional to  $\gamma |\vec{B}_0|$  and noise is known to grow with the frequency.

The sensitivity of spin 1/2 system nuclides can be described by equation 2.9 [14]

$$\text{Sensitivity} \approx \gamma |\vec{B}_0| |\vec{M}| \propto N |\vec{B}_0|^2 / T_{\text{emp}}, \quad \text{Noise} \propto \sqrt{\gamma |\vec{B}_0|} \quad (2.9)$$

## 2.1 Excitation and the Bloch equation

At thermal equilibrium there are no net x and y components of  $\vec{M}$  and NMR signal cannot be detected. If an oscillating (RF) magnetic field  $\vec{B}_1$  is applied along the x-axis, at the Larmor frequency, the magnetization vector  $\vec{M}$  will rotate around  $\vec{B}_1$  and have a component along the y-axis. As  $\vec{M}$  precesses about z-axis, it results in changing magnetic field which can be detected by the voltage it induces in a receiver coil [15]. The voltage is the NMR signal which is recorded during a measurement.

It is possible to completely transform the z magnetization to y magnetization if the duration of the pulse is sufficiently long and this pulse is often referred as  $90^\circ$  pulse [16]. The time evolution of magnetization in a magnetic field can be described by the Bloch equation of 2.11 [3].

$$\vec{B}(t) = \vec{B}_0 + \vec{B}_1(t), \text{ where } |\vec{B}_1| \ll |\vec{B}_0| \quad (2.10)$$

The  $\vec{B}_1$  field will perfectly rotate  $\vec{M}$  about x only if it is applied at the Larmor frequency. If a different frequency is used,  $\vec{B}_1$  is said to be off resonance. In general, off resonance conditions will exist because the static field  $\vec{B}_0$  is not uniform, either due to imperfections in the magnets producing it, or due to distortions resulting from nearby nuclei. Local field offsets can be characterized as  $|\Delta\vec{B}_0| = \Delta\omega_0 / \gamma$  [17] where  $\Delta\omega_0$  is the change in the local Larmor frequency due to local field inhomogeneity  $|\Delta\vec{B}_0|$ . In this case, the total magnetic field  $\vec{B}_{\text{eff}}(t)$  contains an additional term of the local magnetic field effects and is then given by equation 2.11 and in this case, as shown in figure 2.3 magnetization  $\vec{M}$  rotates around  $\vec{B}_{\text{eff}}(t)$ .

$$\vec{B}_{\text{eff}}(t) = \Delta\vec{B}_0 + \vec{B}_1(t) \quad (2.11)$$

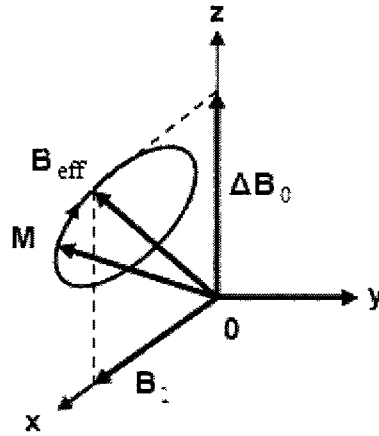


Figure 2.3: Precessional motion around the effective magnetic field

## 2.2 Relaxation

Processes that bring the magnetization back to thermal equilibrium are categorized into T1 relaxation that describes the return of the z-component of longitudinal magnetization to its equilibrium value and T2 relaxation that describes the decay of transverse magnetization. These relaxations are caused by several time dependent interactions between nuclear spins and their thermal environment.

### 2.2.1 T1 relaxation

Longitudinal magnetization returns to equilibrium exponentially according to the T1 relaxation time. This is a thermally driven process which occurs as spins exchange energy with their environment, and is also known as spin-lattice relaxation. Figure 2.4 and equation 2.12 illustrates the return of the z-component of magnetization to the equilibrium value, after population inversion arising from a  $180^\circ$  pulse, one which has rotated the magnetization around the x-axis so that it points along the z direction.

$$M_z(t) = M_0(1 - e^{-t/T_1}) + M_z(t_0) e^{-t/T_1} \quad (2.12)$$

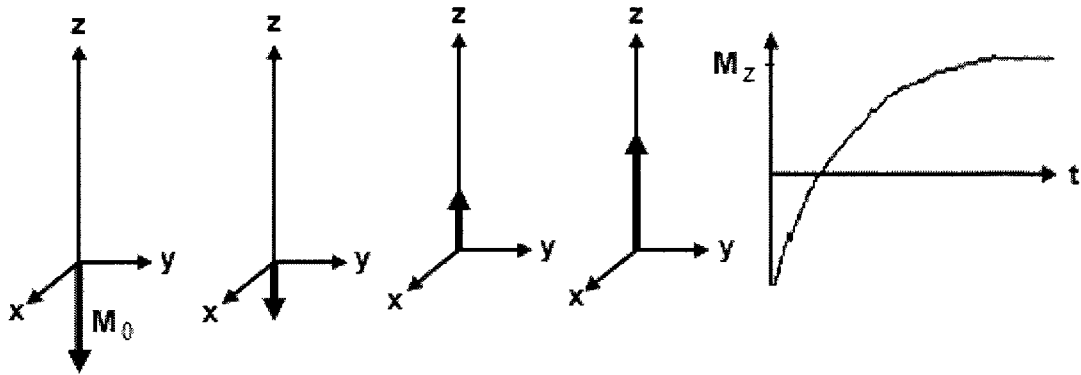


Figure 2.4: The return of z magnetization component

## 2.2.2 T2 relaxation

Spins in the transverse plane also exchange energy with one another, resulting in a loss of coherence within the spin ensemble making up  $\vec{M}_0$ . The loss of coherence results in a spread of phases within the transverse plane, causing a loss of detectable signal, as seen in figure 2.5. This signal loss is exponential, and characterized by time constant  $T_2$

Dephasing due to random spin-spin interactions is irreversible. Spins can also lose coherence due to magnetic field inhomogeneity; the spread of resonant frequencies resulting from the inhomogeneity ultimately results in signal cancellation. This process is characterized by an exponential decay time  $T_{inh} = 1/\gamma |\Delta\vec{B}_0|$ , where  $|\Delta\vec{B}_0|$  is the field inhomogeneity across the sample. The dephasing of spins due to field variation is reversible using a  $180^\circ$  refocusing pulse. The Carr-Purcell-Meiboom-Gill (CPMG) [18] technique is often applied to temporarily limit the contribution of magnetic field inhomogeneity as such  $T_2$  is composed of intrinsic  $T_2^*$  and dephasing.  $T_2$  describes how fast phase coherence is lost between spins and it represents the lifetime of the signal in the transverse plane and it is the relaxation time that is responsible for the line width of

an NMR signal. In a perfectly homogeneous magnetic field  $T_2^* = T_2$ , but  $T_2^*$  is shorter than  $T_2$  when the field is inhomogeneous [19].

$$\frac{1}{T_2^*} = \frac{1}{T_2} + \frac{1}{T_{inh}} = \frac{1}{T_2} + \gamma |\Delta \bar{B}_0| \quad (2.13)$$

In  $T_2$  relaxation the excited magnetization in the  $x$ - $y$  plane decays according to equation 2.14, it is part of the solution to the Bloch equation.

$$M_{x,y}(t) = M_{x,y}(t_0) e^{-t/T_2} \quad (2.14)$$

Equation 2.15 contains precession, relaxation and equilibrium components and it is the phenomenological description of time evolution of local magnetization [20].

$$\partial \bar{M}(t) / \partial t = \gamma (\bar{M}(t) \times \bar{B}(t)) - (M_x(t)\hat{i} + M_y(t)\hat{j})/T_2 - (M_z(t) - M_0)\hat{k}/T_1 \quad (2.15)$$

In the equation 2.16,  $T_2^*$  is employed to determine the line width of the signals at have maximum, which is the Full Width at Half Maximum (FWHM) [19].

$$FWHM = \frac{1}{\pi T_2^*} \quad (2.16)$$

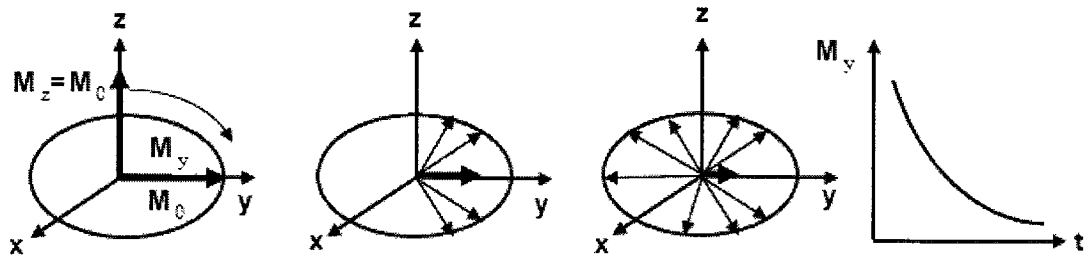


Figure 2.5: Signal decay due to  $T_2$  relaxation

## 2.3 NMR Pulse sequences

Pulse sequences are series of RF pulses used to manipulate nuclear spins to produce NMR signal. Figure 2.6 illustrates the NMR system response. In pulsed magnetic resonance, a short duration burst of RF voltage with frequency  $\omega_0$  is applied to a coil, resulting in a pulsed  $\vec{B}_1$  field applied to the sample. The frequencies excited by the pulse depend on its frequency content, as determined by the FT of the pulse shape. Short pulses are required for uniform excitation of large bandwidths, whereas long pulses lead to selective excitation. In this section some of the basic pulse sequences that are commonly used will be discussed.

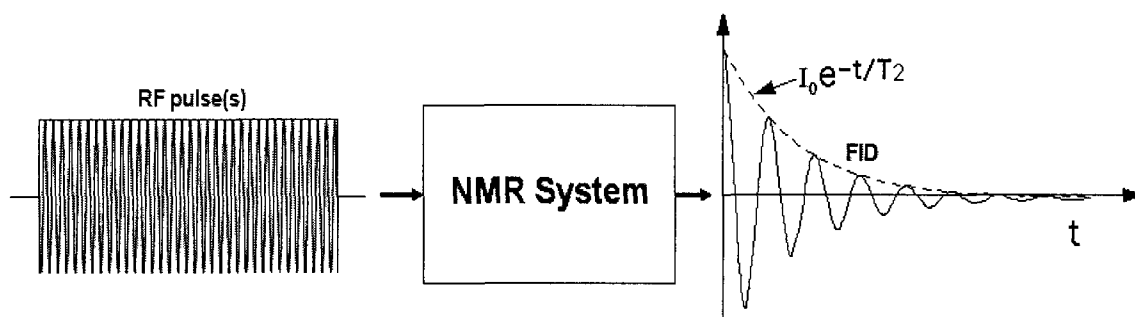


Figure 2.6: NMR system response

The simplest NMR experiment for recording proton spectra can be accomplished using only a  $90^\circ$  RF pulse along the x-axis followed by data acquisition as shown in figure 2.7 [21]. This RF pulse creates transverse magnetization along the y-axis and phase coherence is generated following the  $90^\circ$  pulse. The overall flip angle through which  $\vec{M}_0$  is rotated during the pulse time  $t_p$  is given by  $\gamma |\vec{B}_1| t_p$ . The  $\vec{B}_1$  field strength and the rotation speed of the magnetization can be described by equation 2.17.

$$\omega_1 = \gamma |\vec{B}_1| \quad (2.17)$$

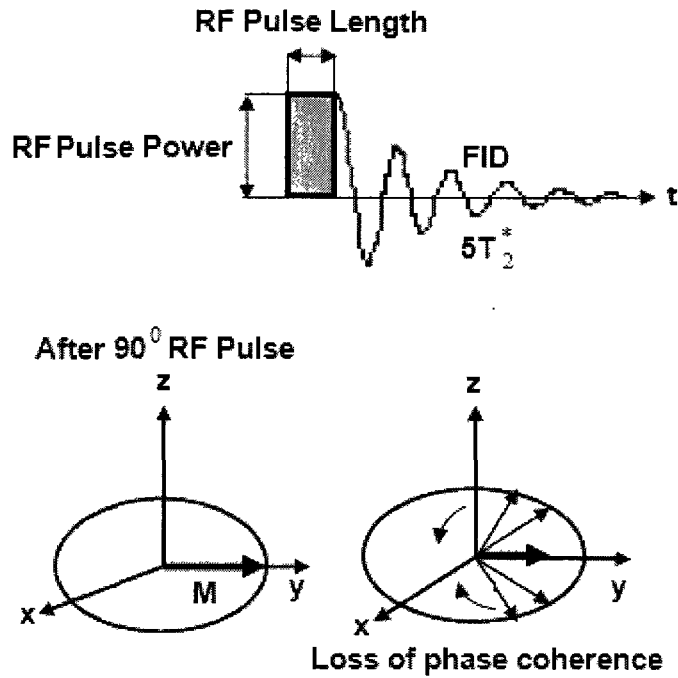


Figure 2.7: A simple pulse sequence

After some period of time spins at different spatial position acquire different phases due to variation in magnetic fields, leading to  $T_2^*$  decay and obscuring measurement information. The spin echo technique was introduced by Hahn to reverse the loss of phase coherence by reversing the spin phases using a  $180^\circ$  pulse [22]. A diagram of the process is shown in figure 2.8. Some  $\tau$  time after the initial  $90^\circ$  pulse, the spins have lost coherence and no signal can be observed. After a  $180^\circ$  pulse is applied, the spins reverse orientation in the transverse plane. Those that lagged the resonant frequency in phase are now ahead, and those that lead are now behind. After another period  $\tau$ , the spins re-align, and an 'echo' forms. The spins again lose coherence with  $T_2^*$ , however additional  $180^\circ$  pulses can be applied to continuously refocus the magnetization. Over time, the amplitude of the echoes decays with  $T_2$ , until signal is no

longer observable. This process is illustrated in figure 2.9. The overall procedure is known as CPMG, after Carr, Purcell, Meiboom and Gill, the inventors of this pulse sequence [18, 23].

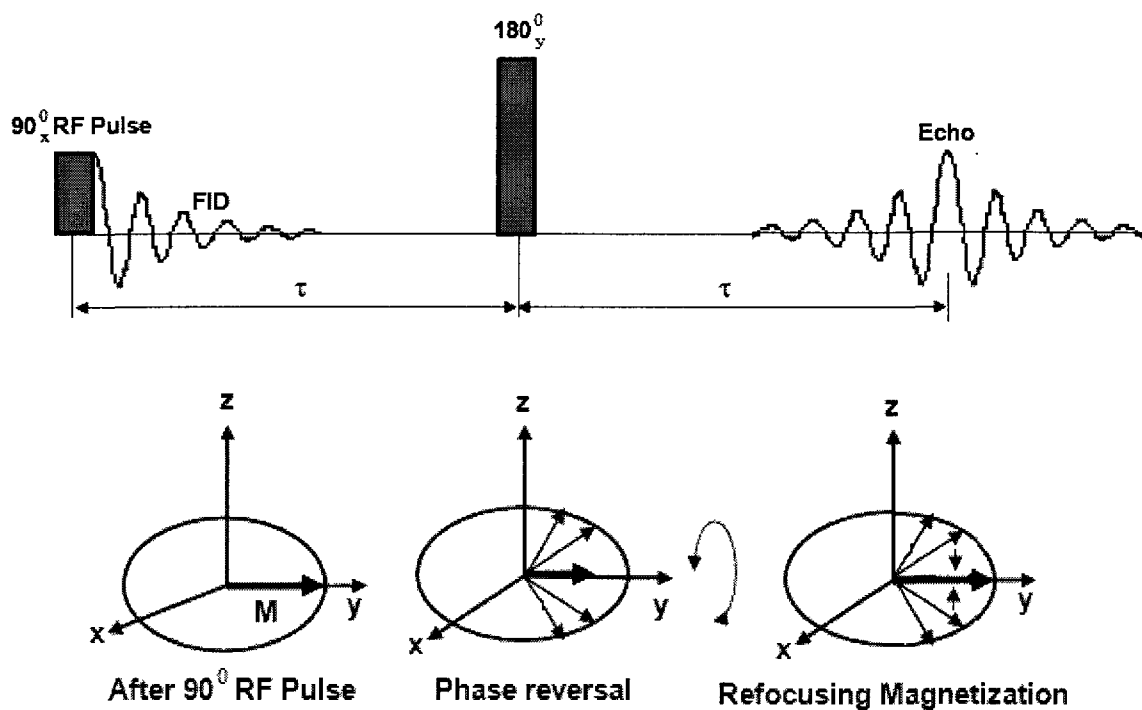


Figure 2.8: Hahn echo

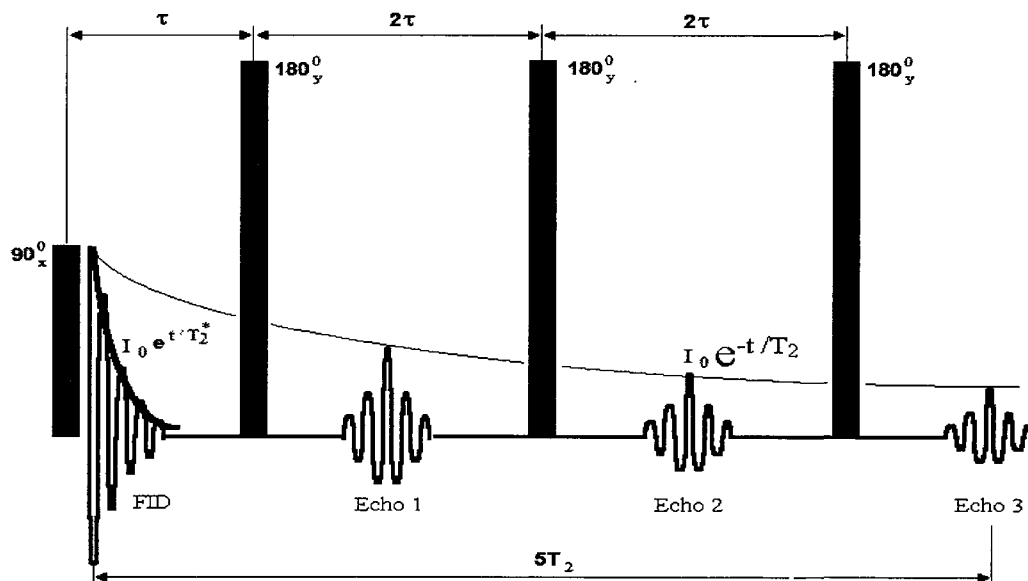


Figure 2.9: CPMG spin echoes and the  $T_2$  envelope

## 2.4 Diffusion

Diffusion describes random, translational motion of ions, molecules or atoms in a solution [24] and can be characterized by coefficient  $D$ . Molecular motion due to diffusion will cause a loss of phase coherence in a sample when magnetic field inhomogeneities are present, resulting in decreased observable NMR signal. Factors that affect diffusion coefficient are: molecular shape, molecular size, solvent viscosity and sample temperature [25]. Magnetic field gradients of equation 2.18 can be used to trace molecular disturbances [26] and it is possible to make diffusion and flow measurements by indirectly labelling the position of NMR active nuclei through their Larmor frequency. To first order, the total external magnetic field at position  $\vec{r}$  is  $\vec{B}(\vec{r}) = \vec{B}_0 + \vec{r} \cdot \vec{G}$  and spins precess with angular frequency  $\omega(\vec{r}) = \gamma |\vec{B}(\vec{r})|$ .

$$\vec{G} = \frac{\partial B_z}{\partial x} \hat{i} - \frac{\partial B_z}{\partial y} \hat{j} - \frac{\partial B_z}{\partial z} \hat{k} \quad (2.18)$$

Several pulse sequences can be used to measure diffusion depending upon the nature of the system under study. Hahn in 1950 studied self diffusion occurring in a system at equilibrium [27]. In 1954 experimental work by Carr and Purcell (CP) demonstrated self diffusion of molecules and flow of molecules can be separated in NMR measurements [28]. Pulsed Gradient Spin Echo (PGSE) and Standard Stimulated Echo (STE) sequences provide the basic foundation for understanding diffusion in NMR. PGSE is a modified Hahn spin echo pulse sequence [29] whereas STE contains three  $90^\circ$  pulses [30]. For this work, pulsed field gradients are not available, and modified versions of these sequences are needed to work with a constant gradient. Steady Gradient Spin Echo (SGSE) and Steady Gradient Stimulated Echo (SGSTE) are constant gradient

diffusion measurement techniques that are often used with single sided magnets. The SGSE uses a  $90^0$  RF pulse followed by  $180^0$  whereas the SGSTE contain three  $90^0$  RF pulses. The normalized signal attenuation equation of SGSE is given by 2.19 [31], where  $\tau$  is the duration between pulses and  $2\tau$  is a time at which an echo is formed,  $T_2$  is the transverse relaxation time,  $\gamma$  gyromagnetic ratio,  $G$  is the constant gradient strength, and  $D$  the diffusion coefficient.

$$I = I_0 \exp(-2/3\gamma^2 G^2 \tau^3 D) \exp(-2\tau/T_2) \quad (2.19)$$

The term  $\exp(-2/3\gamma^2 G^2 \tau^3 D)$  describes signal attenuation as a result of diffusion.  $I$  is the measured intensity and  $I_0$  the maximum peak intensity. With a strong magnetic field gradient  $G$  the diffusion term dominates the relaxation time making the term  $\exp(-2\tau/T_2)$  in equation 2.19 to be negligible [32] allowing the above equation to be simplified to equation 2.20 and for an isotropic solution the plot of  $\ln(I/I_0)$  versus  $b$  gives straight line whose slope equals  $-D$  [28].

$$\ln(I/I_0) = -2/3\gamma^2 G^2 \tau^3 D = -bD \quad (2.20)$$

In the following SGSTE equation 2.21  $\tau_1$  and  $\tau_2$  are the time intervals between the  $90^0$  RF pulses and an echo is formed after  $2\tau_1$  plus  $\tau_2$  time.  $T_1$  and  $T_2$  are the longitudinal and transverse relaxation [33].

$$I = I_0 \exp(-\gamma^2 G^2 \tau_1^2 (\tau_2 + 2/3 \tau_1) D) \exp(-2\tau_1/T_2 - \tau_2/T_1) \quad (2.21)$$

Neglecting relaxation, the SGSTE equation can also be simplified to

$$\ln(I/I_0) = -\gamma^2 G^2 \tau_1^2 (\tau_2 + 2/3 \tau_1) D \quad (2.22)$$

Many systems  $T_1$  is significantly longer than  $T_2$  [34] and comparison of SGSE and SGSTE using equation 2.19 and 2.21 reveals the attenuation of the SGSTE is dependent on  $T_1$  making SGSTE diffusion sequence a method of choice in systems that are characterized by short  $T_2$ .

## 2.5 Imaging

Single sided NMR scanners are useful for imaging of materials in a non-destructive way, for instance, during the tree sawing process imaging of water in wood could provide information on the dryness of woods [35, 36], or imaging of oil and water in well cores may produce vital information to the oil industry [37-39]. The NMR signal that is induced on the receiver coils follows the Faraday's law of induction of equation 2.23, where EMF is the Electromotive Force,  $N$  the number of coil turns and  $\phi$  magnetic flux [40].

$$\text{EMF} = -N \partial\phi / \partial t \quad (2.23)$$

The magnitude of the induced current depends on the orientation of the magnetization vector and the detected signals have a maximum intensity when all the nuclei have been rotated by a  $90^\circ$  with respect to the static magnetic field. The received NMR signal can be expressed by the equation 2.24 [41], where  $M(\vec{r}, t) \approx M_x(\vec{r}, t) + iM_y(\vec{r}, t)$  is transverse magnetization.

$$S_r(t) = k \int \frac{\partial}{\partial t} M(\vec{r}, t) d\vec{r} \quad (2.24)$$

The SPS device is designed to provide NMR information maintained in a single pixel of a MR imaging. For constant magnetic field gradient and ignoring the effects of

diffusion, flow, chemical shift and  $T_2$  relaxation, the 1D NMR imaging principle can be expressed by equation 2.25, where the initial value of magnetization is proportional to the spin density  $\rho(\vec{r})$  of the sample at the position  $\vec{r}$ . In the 1D case,  $\vec{B} = \vec{B}_0 + \vec{G}_x$ , and  $\omega_0 = \gamma |\vec{B}|$ . Higher spin density produces stronger signal.

$$S(t) = \int \rho(x) e^{-i\omega_0 t} dx = e^{-i\gamma |\vec{B}_0| t} \int \rho(x) e^{-i\gamma \vec{G}_x t} dx \quad (2.25)$$

Spin density  $\rho(x)$  can also be calculated by taking the inverse FT of the NMR signal  $S(t)$  and the reciprocal space vector  $k$  is defined as  $k_x = \gamma G_x t / 2\pi$  [42].

The above analysis assumes the sample is entirely within a static field with a constant gradient. The Fourier components of the image are sampled as a function of time, and the resulting image is obtained by Fourier transform. It is also possible to build up an image, one pixel at a time, by exciting only a small region, corresponding to one pixel, recording the pixel intensity, moving the scanner, and repeating. It is this approach that is used later in the thesis.

## 2.6 Parameters that affect the NMR signal quality

In pulse NMR experiment a spectrum is obtained when an excitation pulse is succeeded by detection of Free Induction Decay (FID) and Fourier transformation. In this work, pulse NMR is not feasible, as the  $T_2^*$  of the instrument used was too short to observe an FID signal after  $90^\circ$  pulse. For this reason, all measurements were based on one or more echoes, observed through the CPMG sequence. The NMR signal induced by the precessing magnetization is very weak and corrupted with thermal noise. Several experimental parameters govern the measurement SNR.

## 2.6.1 NMR scans

It is usual practice to acquire many scans which are subsequently averaged to improve the quality of the detected signal. For additive Gaussian white noise, SNR improves in proportion to the square root of the number of scans [43].

$$\text{SNR} \propto \sqrt{\#\text{ofScans}} \quad (2.26)$$

## 2.6.2 Phase cycling

Aside from thermal noise, NMR measurements are corrupted by other factors such as baseline artifacts present in the receiver Analog to Digital Converter (ADC) and noise from acoustic ringing in the RF coil due to the strong current of the applied pulses [44]. It is possible to cancel undesirable signals during NMR measurement by alternating the phase of the RF pulse and adding or subtracting the NMR signal at the receiver. Phase cycling is a technique that involves repeating the execution of a pulse sequence with identical timings and pulse tip angles but with well thought and justified changes to the phases of the RF pulse. It is an important technique in NMR and describes an application of pulses with different phases to eliminate artifacts that have different phase behavior than the real NMR signal.

## 2.6.3 Multi-echo averaging

In addition SNR can be improved through multi-echo averaging techniques [45]. A CPMG measurement generates many echoes, although their amplitudes decay with  $T_2$ , each has the same shape and they can be ensemble averaged to generate one representative echo for the measurement. The number of possible echoes is limited by  $T_2$

and echo time,  $\tau$ . In principle, hundreds of echoes can be acquired and averaged in one measurement, dramatically improving the SNR.

## 2.7 Spectral resolution

A powerful aspect of NMR is the spectral information contained in the recorded signal. The resonance frequency depends on the strength of the applied static field and gyromagnetic ratio of the nucleus, however the field strength to be considered is not exactly the strength of the applied magnetic field, but locally modified by surrounding nuclei within a molecule. The Zeeman interaction describes the interactions between spins and magnetic field [46] and slight variations in the resonant frequency gives detailed information about the molecular structure in which the atom resides. In organic molecule more than a single line is observed and the splitting of lines is caused by the chemical shift due to the Zeeman interaction and spin to spin couplings [47, 27], for instance the splitting of the lines in  $C_2H_6OH$  to  $CH_3$ ,  $CH_2$ , and  $OH$  causes three lines to be observed. The difference between the applied magnetic field and the field at the nucleus is termed nuclear shielding or often referred as chemical shift and it is usually expressed as parts per million and calculated using equation 2.27 where  $\omega_s$  is the offset frequency [28].

$$\delta_i = \frac{\omega_s - \omega_0}{\omega_0} \times 10^6 \quad (2.27)$$

Chemical shift forms the foundation for NMR chemical spectroscopy where the spectrum can provide information about the chemical composition of a sample and its bonding arrangements. Figure 2.10 shows the effect of chemical shift in  $^1H$  NMR spectra of

Acetaldehyde  $\text{CH}_3\text{CHO}$  where higher chemical shift reflects light shielding and the heavily shielded hydrogen atom in  $\text{CH}_3$  have lower chemical shift value [48].

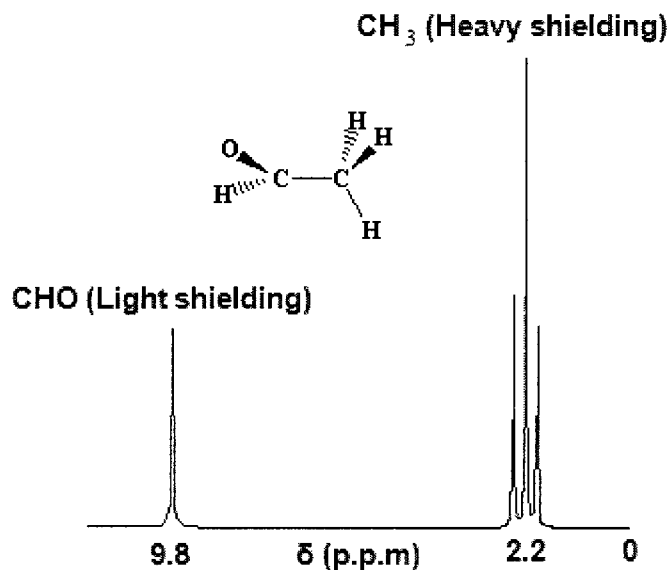


Figure 2.10:  $^1\text{H}$  NMR spectrum of Acetaldehyde [29]

Spectral resolution can be determined by transverse relaxation time of the spins and it is a measure of how well one is able to separate signals within spectra. When magnetic field inhomogeneities are larger than the chemical shift, the NMR lineshape reflects the magnetic field distribution, and chemical shift information is lost [49]. In conventional NMR systems, high spectral resolution is achieved by carefully shimming the  $\vec{B}_0$  field to be as homogeneous as possible, to within fractions of a ppm. In an inhomogeneous field, such as the system used for this thesis, spectral resolution is approximately equal to the bandwidth of the applied RF pulses. This means that any phenomenon occurring on a time scale longer than the RF pulse cannot be observed in the signal spectrum. This includes not only chemical shift, but also molecular motion, due to fluid flow or self diffusion.

Chemical shift resolved NMR spectra were observed by Perlo et al. for the first time outside a portable single-sided magnet [50]. Spectral hole-burning is a high resolution experimental method proven to be quite useful tool for investigating NMR active nuclei population decay, energy transfer processes, optical dephasing and spectral diffusion [51]. Sigmund and Halperin demonstrated hole burning NMR diffusometry technique in large magnetic field gradients [52] and the experimental result provided micron scale resolution in one dimension diffusion studies. Todica and Blümich also performed a similar experiment using modified Hahn echo technique to discriminate the molecular dynamics of relaxation and diffusion by making use of the strong magnetic field gradient [53].

## **2.8 MR Hardware**

The conventional MR hardware has closed magnet design involving the use of large magnets with strong and homogeneous magnetic fields. The typical magnet shape is a solenoid, with the sample inserted in the middle. The solenoid shape is used as it facilitates generation of a highly homogeneous static field. Although, MR machines with high field strength inherently provide a better SNR compared to low field units [54] they are expensive to buy as well as to operate and are not easily portable. Furthermore, sample access is limited, as the material or subject being examined must fit in the bore of the magnet. For many applications portable NMR sensors, built from permanent magnets offer several advantages over conventional one [41, 55]. Furthermore, open or single sided magnet geometries which project a MR compatible magnetic field to one side of the magnets remove sample size restrictions. The disadvantage is that a homogeneous field cannot be generated out in space, and this type of magnet has an inherently

inhomogeneous  $\vec{B}_0$  field. This section briefly describes conventional MR hardware, and contrasts this with the single sided magnet used for this thesis.

### 2.8.1 Conventional

Conventional MR hardware generates the static magnetic field  $\vec{B}_0$  using a superconducting solenoidal coil bathed in liquid Helium in order to maintain the current thus the field strength. Field corrections are made using shim coils which allow a highly uniform magnetic field to be obtained [56]. In the figure 2.11 configuration the sample is fitted inside of the RF coil which provides the  $\vec{B}_1$ .

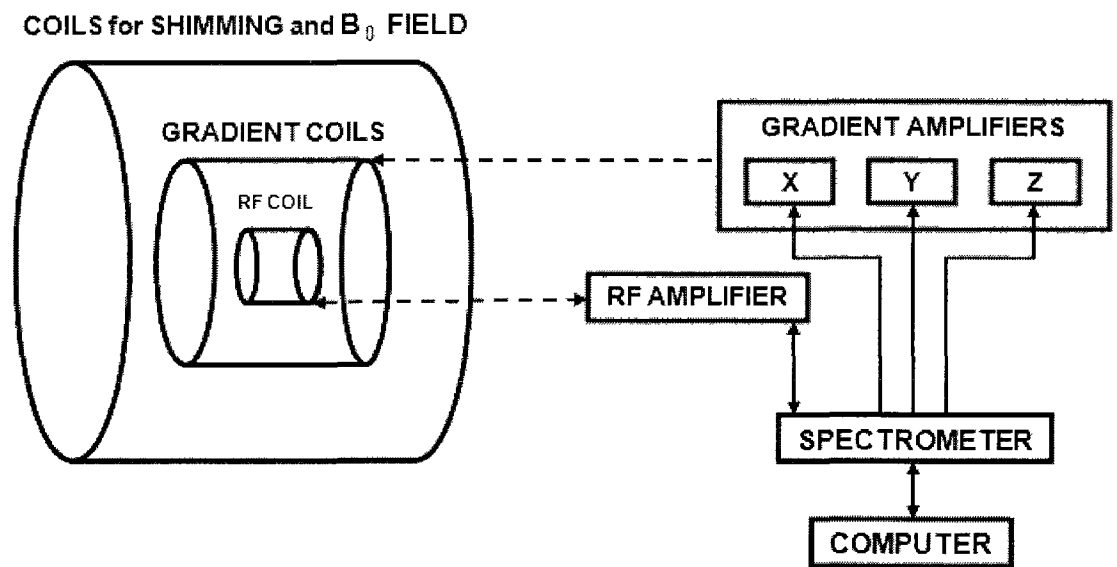


Figure 2.11: Conventional MR hardware block diagram

Gradient magnetic field provides the means to spatially encode the  $^1\text{H}$  NMR signals and the typical conventional imaging system employs three gradient coils designed to produce linearly varied magnetic fields in the three spatial directions across the imaging volume.

In pulse NMR the nuclei are excited by intense pulse of RF radiation and the RF coil is used to deliver the orthogonal  $\vec{B}_1$  field and to pick up the NMR signal [57]. There are many RF coil designs depending on the nature and shape of the sample under investigation. Surface coil design provides the possibility of the receiver system brought closer to the patients. Phased array, solenoid, and quadrature coil are the other design alternatives. The birdcage coil provides the best field homogeneity of all RF imaging coils and it has been the method of choice due to its ability to achieve circular polarization with homogeneity under several conditions [58, 59].

A spectrometer provides the RF pulses, controls the gradients, and amplifies and digitizes the recorded MR signal. The spectrometer is programmed, and recorded data is analyzed on a PC.

A block diagram of the spectrometer is shown in figure 2.12. The RF pulses generated by the spectrometer are amplified and fed to the probe (RF coil) through crossed diodes. After the pulse, the diodes turn off, isolating the receive chain from the transmitter. The detected NMR signal passes from the coil, through a circuit which protects the receiver from the high power RF pulse, and into a low noise pre-amplifier. The signal is then split into two demodulated in quadrature, and digitized by the ADC and fed into the computer memory [60]. In single channel detection FT cannot tell the difference between negative and positive frequencies relative to the carrier frequency [61], therefore the spectrometer uses quadrature detection to distinguish the magnetization rotational direction

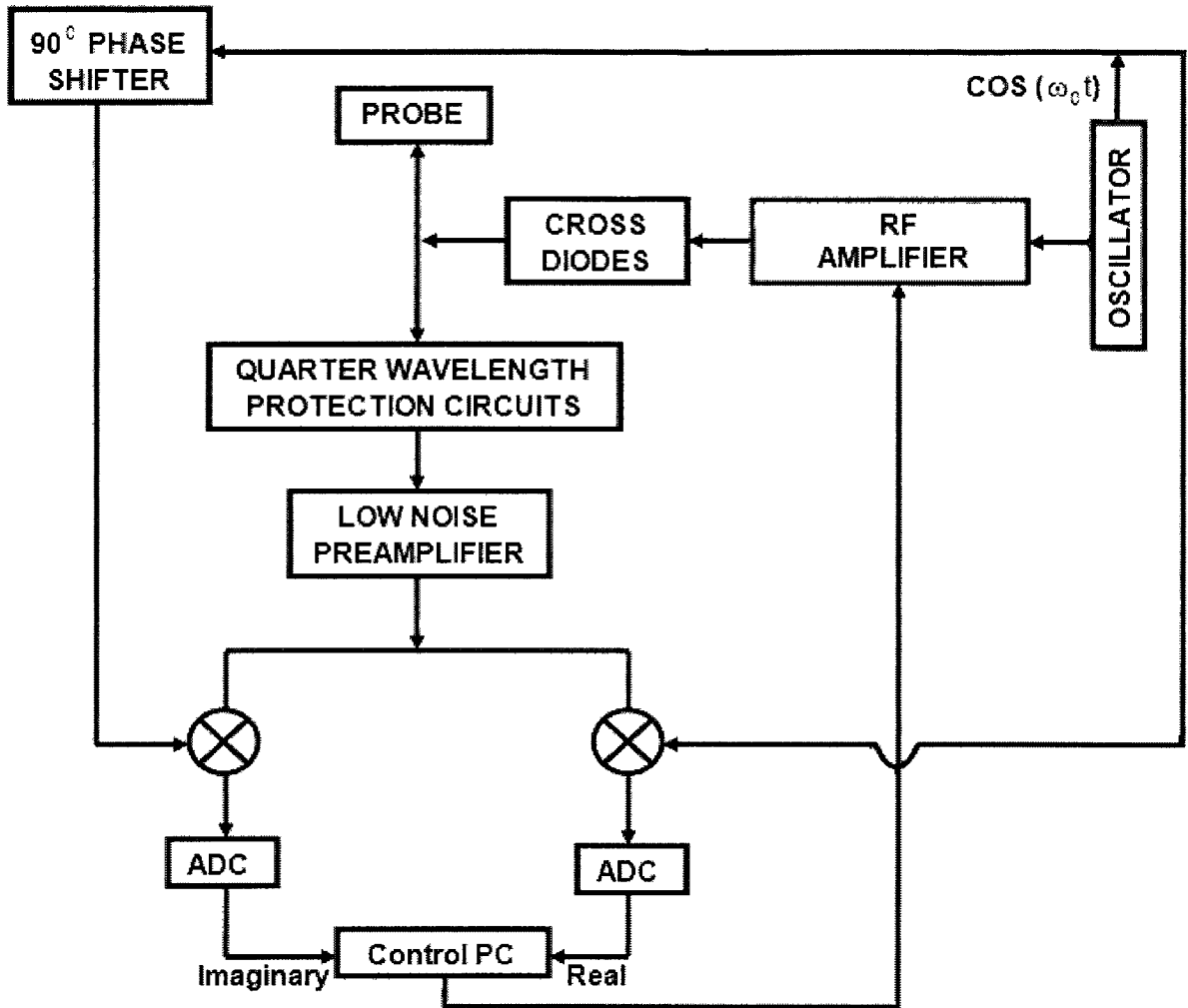


Figure 2.12: The RF path

### 2.8.2 Single sided MR hardware

Permanent bar magnets are ideal for building small compact low field MR scanners with open magnets design and field strength below 1T. The field created by the spin of bar magnets is always on full strength and costs nothing to maintain, however it is difficult to build high field strength conventional MR machine using this type of magnets. The benefit of not having to put samples under investigation inside the bore of a magnet

is enormous type of; this type of device is single sided, portable with reduced system cost and complexity that allow the possibility of studying bulky objects.

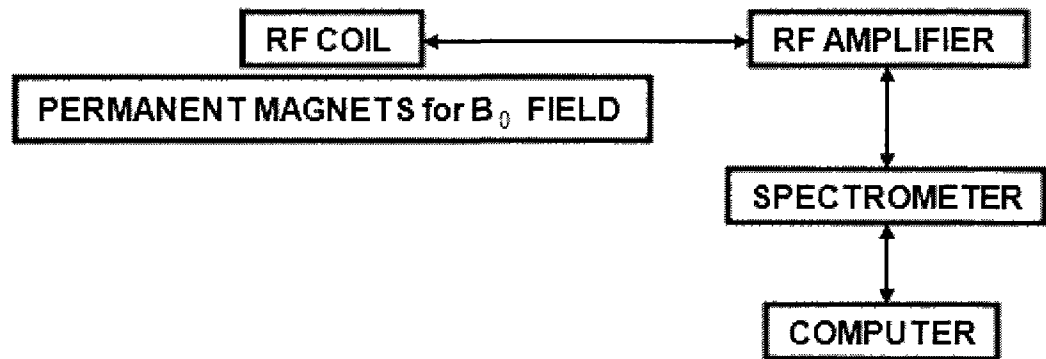


Figure 2.13: Single sided MR hardware block diagram

The typical single sided MR scanner setup, shown in figure 2.13, contains permanent magnets for producing static magnetic field, RF coil, spectrometer along with RF amplifier unit, and desk top computer. The configuration of permanent magnets is designed to produce a static magnetic field suitable for magnetic resonance in the sample volume. The RF coil is generally a surface coil, so the sample can be placed on top of the measurement apparatus. Unlike conventional MR hardware the SPS device does not contain coils for generating gradient fields, here the word gradient field refers to the change of static magnetic field strength over a distance. In a closed solenoidal magnet, the magnetic field is relatively uniform within the sample volume. In an open configuration, the sample is bounded by the magnet on one side and infinity on the other (where the field must go to zero) and as a result the field must be spatially inhomogeneous. Magnets can be arranged to give a region of local field homogeneity (a saddle point) in the sample volume, however strong field gradients will always be present.

## 2.9 MR in inhomogeneous magnetic fields

In this section, background of single sided NMR and selective excitation is explored. The stray field MR principles played an important role to the development of mobile unilateral NMR devices. The first single sided device the NMR MOUSE is discussed here. The journal review on selective excitation exemplifies the significance of choosing a narrow frequency band. Previous works concerning pulse sequences for inhomogeneous fields are examined.

### 2.9.1 Mobile single sided NMR

There has been much research into making MR measurements in ‘stray’ fields. The inhomogeneous fields present to one side of a magnet configurations. These systems are quite useful for some special applications for instance examining automobile tires for defect or checking for the level of fat contents in dairy products [62, 63]. Hurlimann and Griffin [64] employed portable stray field NMR probe for well logging in grossly inhomogeneous  $B_0$  and  $B_1$  fields.

STRAFI (Stray Field Imaging) was first proposed by Samoilenko [65] and it offers high spatial resolution imaging of solids and other systems in which  $T_2$  is short. It is an inexpensive imaging method to implement on an existing broadband solid state spectrometer and its basic principle is to place a sample in a large spatially uniform magnetic field gradient region of a magnet; P. J. McDonald and associates have extensively investigated STRAFI in a wide variety of systems [66-69]. Although the first STRAFI experiments were carried out with superconducting magnets, afterwards similar results were obtained using small portable permanent magnets [55].

During the last decade there has been rapid progress in permanent magnet design for compact NMR systems. The NMR MOUSE which works similarly to SPS is the first small mobile stray field NMR sensor developed by Eidmann et al. [70]. It comprised of a u-shaped magnet along with RF coil in the gap between the poles and weighting less than 1 kg with static magnetic field strength of around 0.5 T and gradient on the order of 10-20 T/m [71]. The magnets arrangement is optimized for a constant magnetic field gradient over an external volume producing a sensitive spot above the RF coils surface. Subsequent designs for the most part focused on modifying the magnet arrangement to improve the sensitive volume. The NMR MOUSE was primarily used to measure  $T_2$  in various samples using the CPMG pulse sequence [72]

## **2.9.2 Selective excitation**

There have been growing interest to find techniques that improve the spatial resolution of NMR imaging or the selectivity of high resolution NMR spectroscopy. Selective excitation in inhomogeneous magnetic field is a spatial localization of signal source; it is achieved by directly analyzing the spectrum of the corresponding excited region. In selective excitation the selected area is directly proportional to the bandwidth of the pulse [73, 74]. A short duration RF pulse often referred as hard pulse would excite a wider area of a sample whereas long pulse (soft pulse) is more selective and excites narrow sample region. The following figure 2.14 describes the relationship between the RF pulse width and the corresponding excitation profile.

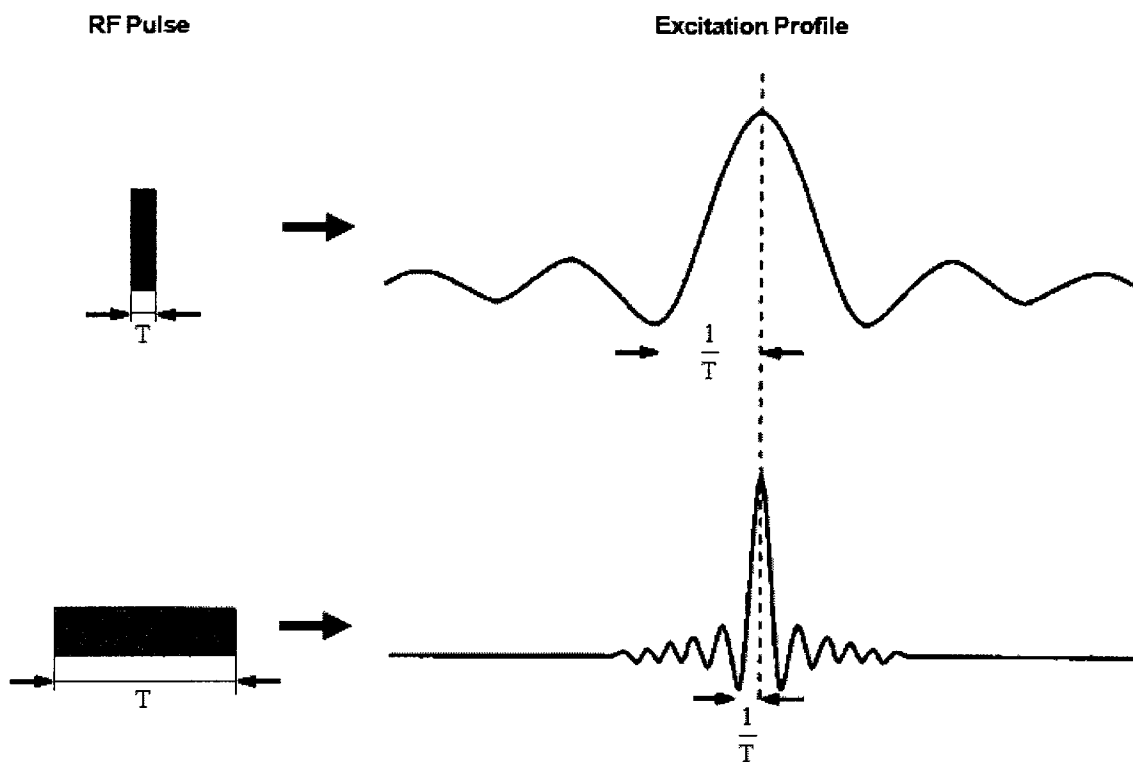


Figure 2.14: RF pulse width effect on excitation  
The excited spectrum corresponds to the Fourier Transform of the pulse shape.

Research has shown more desirable results can be achieved in MR imaging and spectroscopy through the use of selective excitation and this method has been extended into most areas of high resolution NMR including relaxation time measurements, the suppression of unwanted solvent peaks, and slow chemical exchange studies [75].

The first selective excitation techniques were proposed by S. Alexander. The method used relatively weak pulse of long duration to give a  $90^{\circ}$  rotation to the chosen resonance line while leaving the chemically shifted neighbour unaffected with  $360^{\circ}$  rotation [76]. Redfield has extended this technique to solvent peak suppression in FT NMR [77]. Tomlinson and Hill have proposed a general method in which the

frequency spectrum of the excitation may be tailored to any desired pattern. The operator simply defines the desired excitation spectrum in the frequency domain, and the computer calculates the FT of this pattern and uses it to modulate the amplitude or the pulse width of a sequence of RF pulses. This technique has been used extensively in many areas; however it assumes the RF amplifier and probe response to be linear, whereas the conventional transmitters use nonlinear probe and amplifier networks to achieve good isolation between transmitter and receiver [78]. Morris and Freeman 1978 suggested Delays Alternating with Nutations for Tailored Excitation (DANTE) [79] pulse sequence with the minimum modification to a conventional FT spectrometer technique. This selective pulse sequence distributes the power over a series of excitation bands through succession of short high power RF pulses with the flip angle  $\theta \ll 90^\circ$  that are separated by a delay of  $\tau$  seconds and only those resonances that are offset from the transmitter by  $N/\tau$  are excited to a significant extent, where  $N$  is an integer. The excited spectra correspond to total flip angle of  $90^\circ$ . Todica and colleagues applied DANTE pulse sequence technique to obtain a signal in strongly inhomogeneous mobile NMR sensors and by replacing the  $90^\circ$  RF pulse by series of short small flip angle pulses the method reduced the peak of RF excitation power to a minimum [80]. Frank sequence is another low power NMR excitation scheme that consists of constant amplitude, small flip angle pulses, the phases of which are modulated according to a family of polyphase sequences. This technique minimized the peak excitation power while maximizing the NMR response power and portable NMR scanners can benefit from this method [81]. Multidimensional experiments can also benefit from narrow band excitation to reduce the experimental time required to unravel overlapped signals and D. Reichert et al. [82]

experimented with selective excitation to transform 2D spin diffusion for obtaining structural information into its 1D analogue. Schick also discussed the possibility of obtaining high yield intensity signal by selecting a very narrow frequency band [83].

In a low SNR environment, a significant drawback of selective pulses is that they limit the total sample volume being excited. Less excitation translates to fewer signals, and the resulting measurement may be completely obscured by noise. In this thesis, we explore the use of selective pulses to increase the image resolution of a single sided magnet arrangement by limiting the sample volume being excited. A new spectroscopy technique is also developed which combines the resolution advantages of selective pulses with the higher SNR available from broadband excitation. Selective excitation is achieved simultaneously at a large number of resonant frequencies, and the results averaged to give narrow, but high SNR spectra.

## **Chapter 3.0 Hardware design for single sided NMR**

The thesis began by being involved in ordering parts and assembling the complete single sided NMR system from scratch. The magnet array, RF coil, and protection circuitry discussed here were assembled as part of this thesis. The complete experimental setup, shown in figure 3.0 consists of Neodymium Iron Boron (NdFeB) permanent magnet array, a probe with associated tuning and protection circuitry, positioning system, Gaussmeter, spectrometer as well as desktop computer.

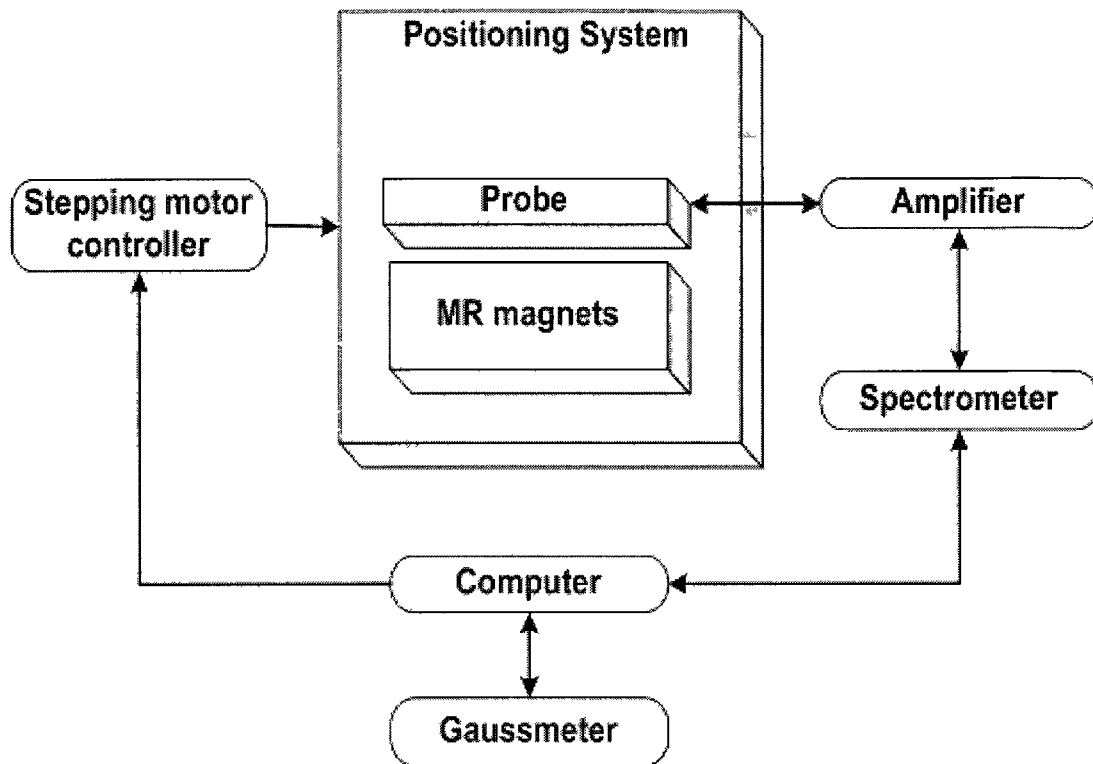


Figure 3.0: The complete hardware setup of SPS

The spectrometer used to control all experiments was a Bruker Minispec, shown in figure 3.1. This benchtop spectrometer is designed for low-field, time domain measurements, and is well suited to single sided NMR experimental control. The ExpSpel software design environment provides the support for many standard and advanced applications including user defined pulses thereby enabling the development of this thesis's pulse sequence for multi-frequency selective NMR excitation [84]. A pulse sequence is written in ExpSpel, then downloaded and executed on the spectrometer.

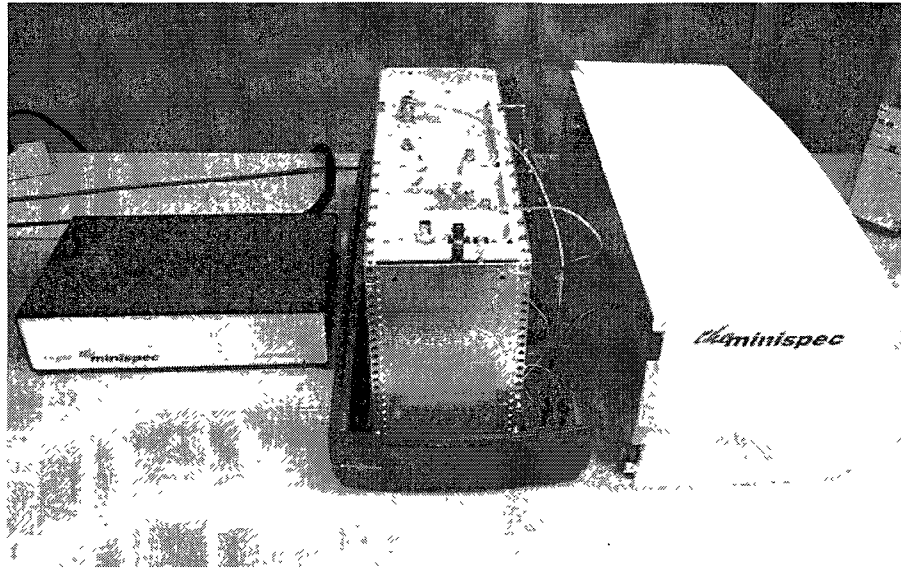


Figure 3.1: NMR spectrometer

The figure 3.2 Lakeshore 460 3-channel Hall effect Gaussmeter allows the measurement of Hall voltage generated by a magnetic field. It is equipped with both parallel and serial computer interfaces for command and data exchange [85]. The Gaussmeter was used for all magnetic field measurements in this thesis.

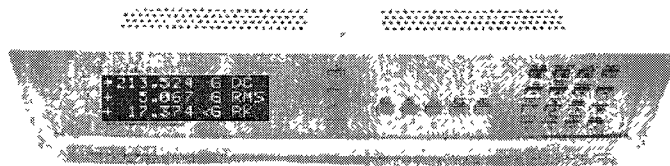
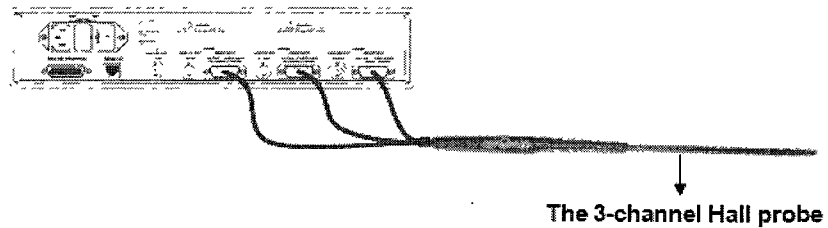


Figure 3.2: Lakeshore 460 3-channel Gaussmeter [85]

### 3.1 Magnet designs for SPS

Figure 3.3 shows a diagram of the magnet array used to provide the  $\vec{B}_0$  field for all measurements. The design follows that of [86] and consists of a 2cm x 5cm x10cm central magnet sandwiched between two 3cm x 5cm x 10cm magnets. The grade N48 magnets were purchased from K&J Magnetics (Jamison, PA). The magnetization directions are indicated in the figure. The 1D magnetic field profiles of this compact device were analyzed while placing the middle magnet at various heights relative to the outer magnets. Magnetic fields were measured via a Lakeshore 460 3-channel Gaussmeter along with 3-axis Hall probe and computer controlled positioning system was used to quantify the magnetic fields that are present at the surface of the three magnet array.

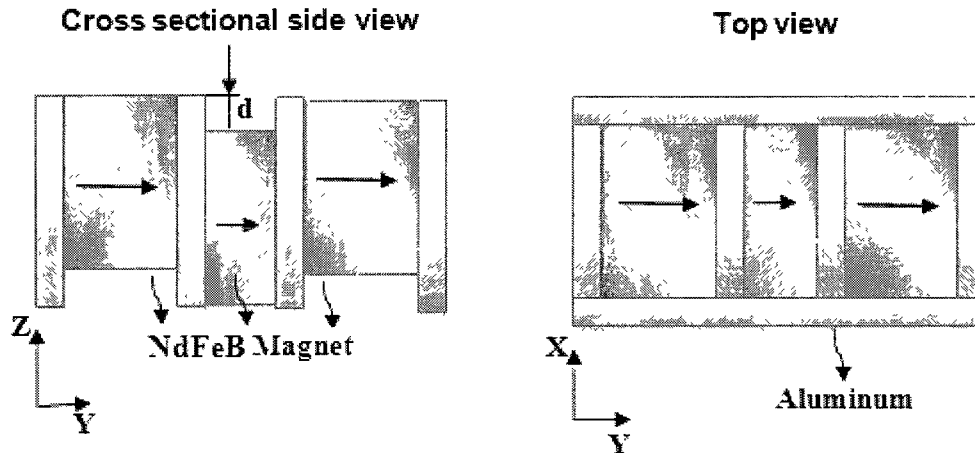
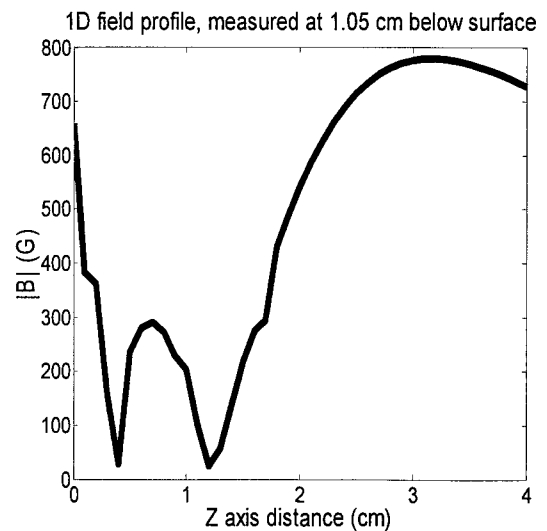
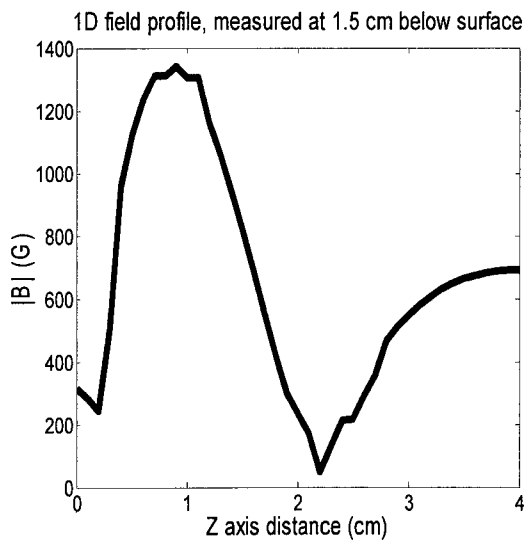


Figure 3.3: Magnets arrangement for SPS

Initially the middle magnet was placed at 1.5 cm depth relative to the outer magnets' surface. The Hall probe was then placed on the centre magnet's surface and a 1D vertical direction field measurement is performed as the probe is being transported away from the magnets by the positioning system. The experimental procedure was

repeated while the middle magnet's location got shifted upwards with step size of 0.05 cm, this continued up until the middle magnet's height has reached 0.3 cm higher than the outer magnets'. A total of thirty seven plots were measured during this experiment. Figure 3.4 shows six example 1D plots for different displacements of the centre magnet, on the other hand figure 3.5 presents the 2D profile when measured across the whole width and center magnet being at 0.4 cm below the surface.

The plots show magnetic field strength, over the centre of the magnet array, as a function of distance from the surface of the magnets. A slower variation in the field strength indicates higher homogeneity. For larger displacements, the field has a local maximum, where the field is relatively homogeneous: the first spatial derivative goes to zero. At a displacement of about 0.4 cm, the field profile has an almost flat region, spanning approximately 1cm. As the central magnet is moved further upward, the field profile has no extrema (last plot). In this case, the field has a constant, relatively uniform gradient (rate of change).



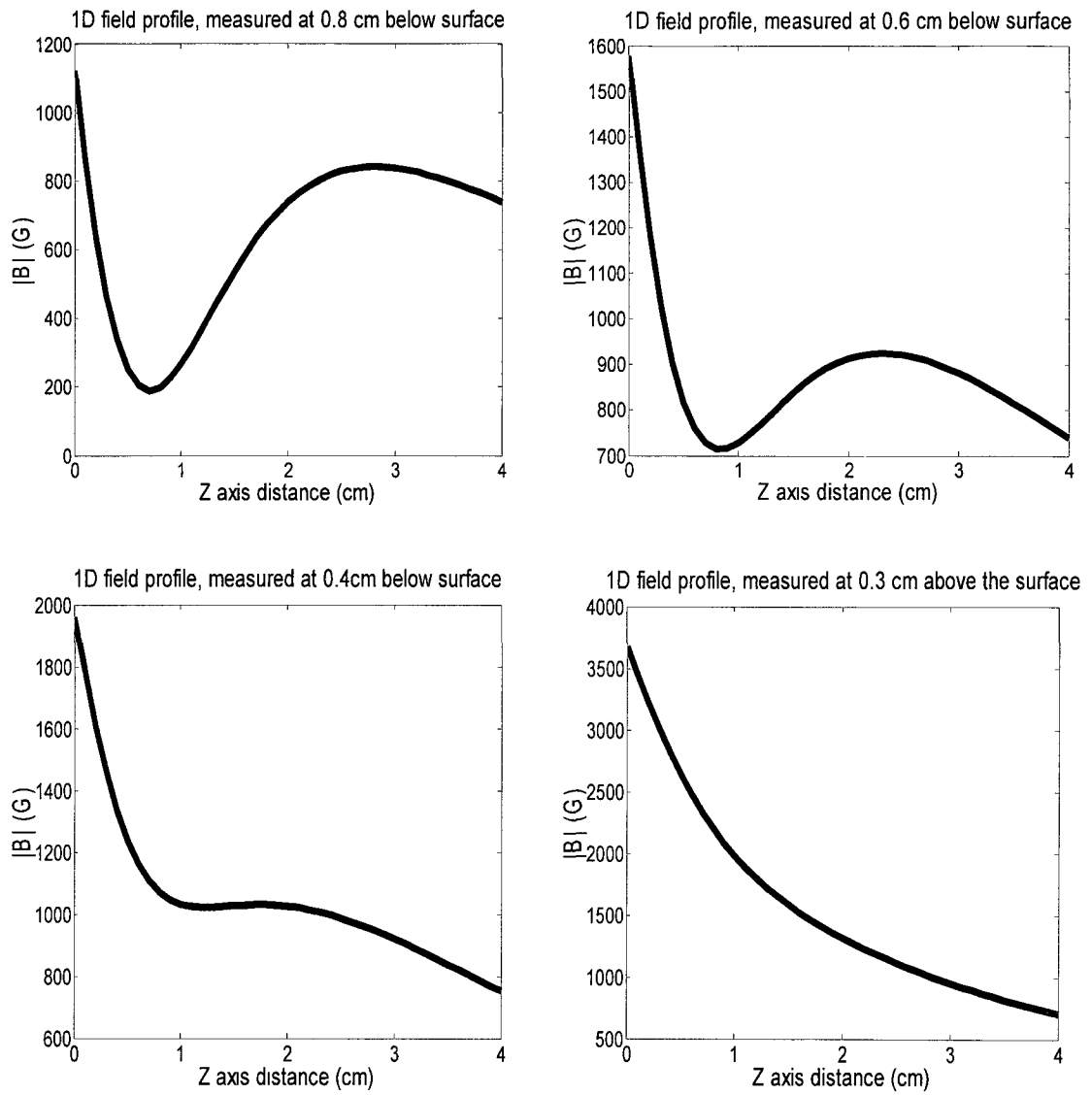


Figure 3.4: 1D magnetic field profiles of SPS

Field profile when measured across the whole width,  $d = 4$  mm below surface

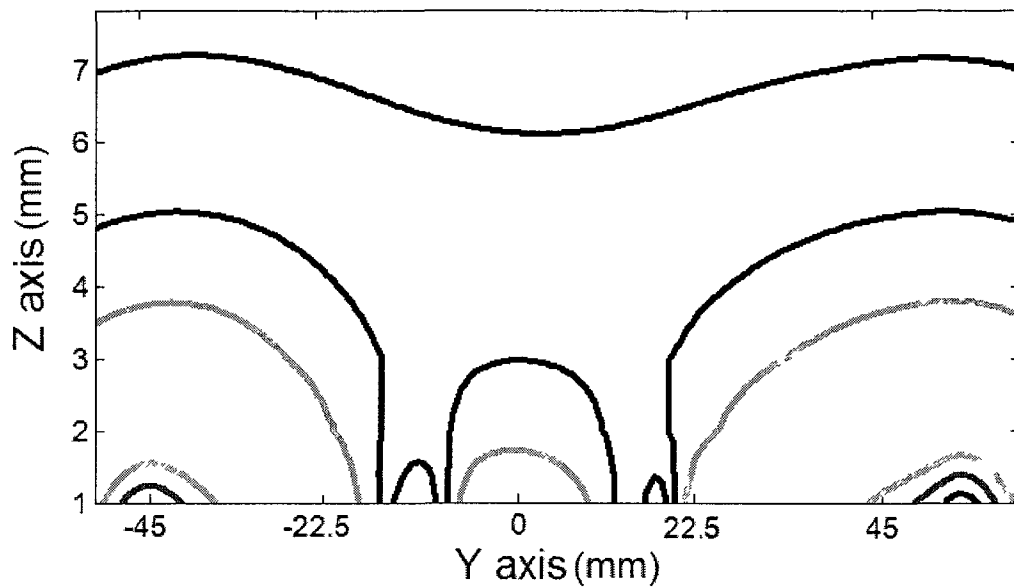


Figure 3.5: The whole width 2D magnetic field profile SPS

### 3.1.1 Relatively homogenous field magnets

The difficulty of mobile unilateral NMR systems is the presence of inhomogeneous magnetic field which obscures measurement information and a relatively homogeneous field magnets design is known to provide a strong single sided NMR signal, facilitating the measurements of various samples. The design has been characterized by a magnets arrangement in which the first and second spatial derivatives of  $\vec{B}_0$  equals zero, resulting in a relatively homogenous field region above the SPS's magnets. Noteworthy, this relative homogeneity is still significantly below the conventional MR scanner, and from a conventional NMR perspective, the field would still be classified as grossly inhomogeneous. From the plots above, we conclude that choosing a displacement of 0.4cm for the centre magnet gives the most relative homogeneous field possible. The field plot for that displacement contains a horizontal

section implying the spatial derivatives of the static magnetic field to be zero at that location [86, 87]. Figure 3.6 shows a picture of the magnet arrangement, with the approximate location of the sensitive volume indicated. In the sensitive regions, the field strength is just over 1000 Gauss, which was determined to correspond to a 4.55 MHz resonance frequency.

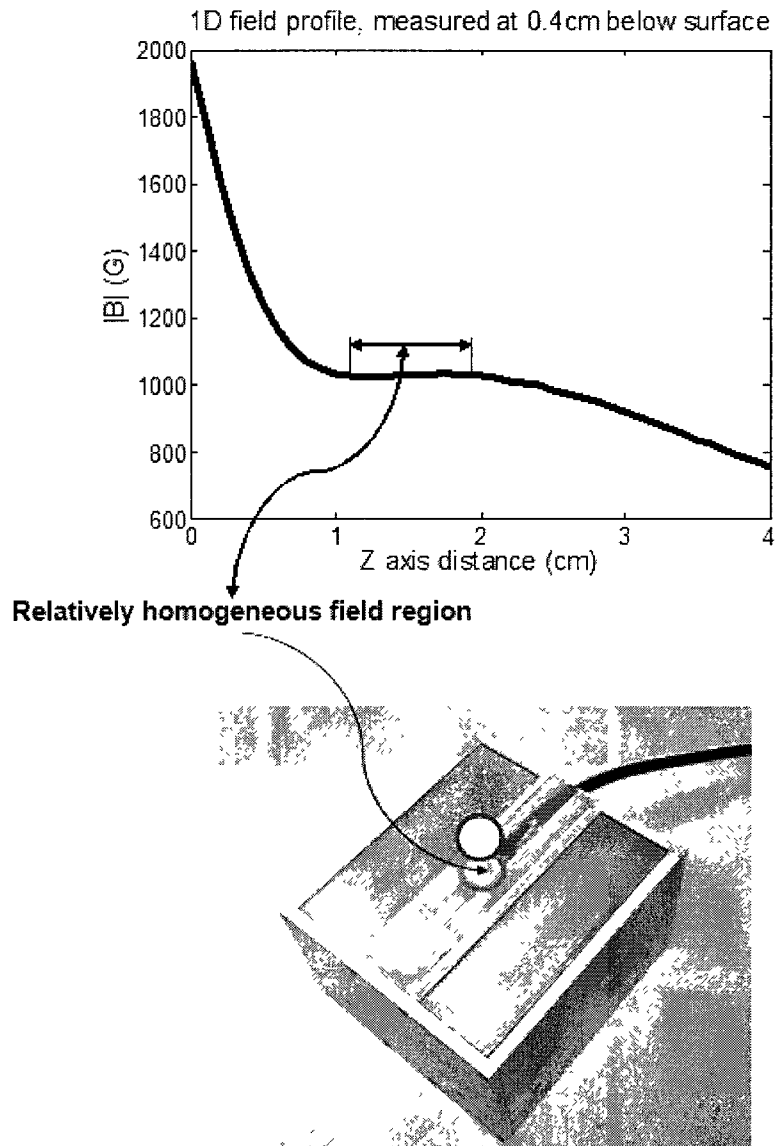
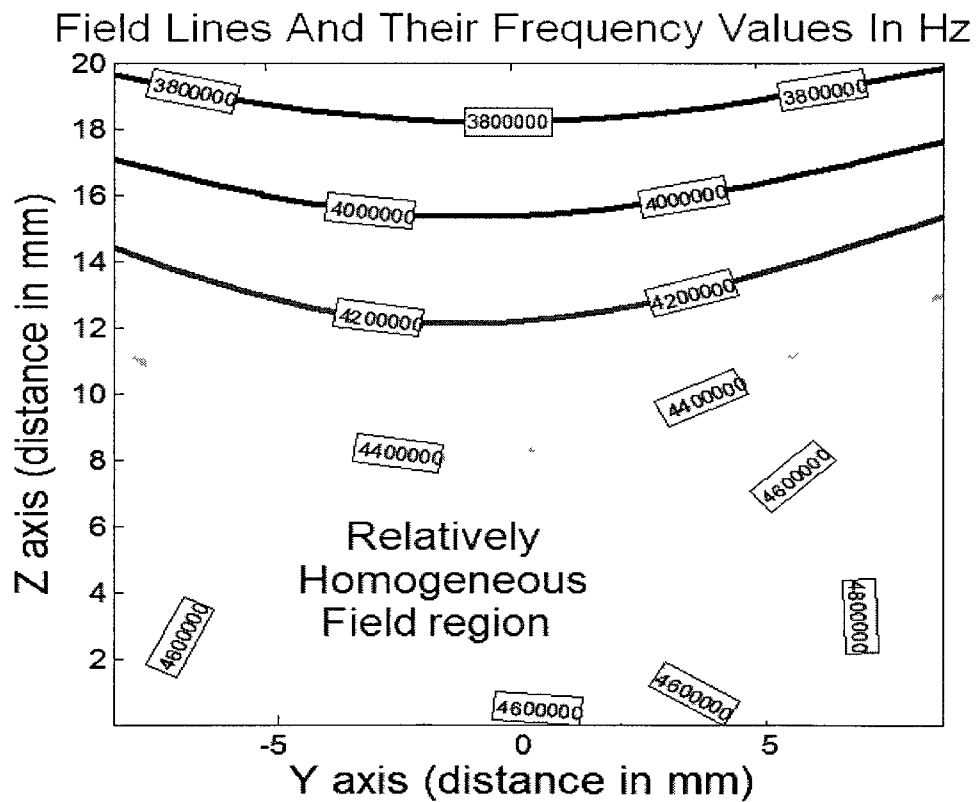


Figure 3.6: 1D field profile and the sensitive volume  
(Centre magnet's height is 0.4 cm below the outer magnets' top)

In figure 3.7, the  $|\vec{B}_0|$  contour map of the field from magnet array provides information about the size of sensitive region. The excitable frequency range is equal to NMR frequency  $\pm$  BW; therefore it is possible to predict the region of stable detectable signals based on the size of RF pulse width. The Y-Z contour lines that enclose the sensitive volume are found within  $\pm 100$  kHz of the saddle point's centre.



## Field Lines And Their Frequency Values In Hz

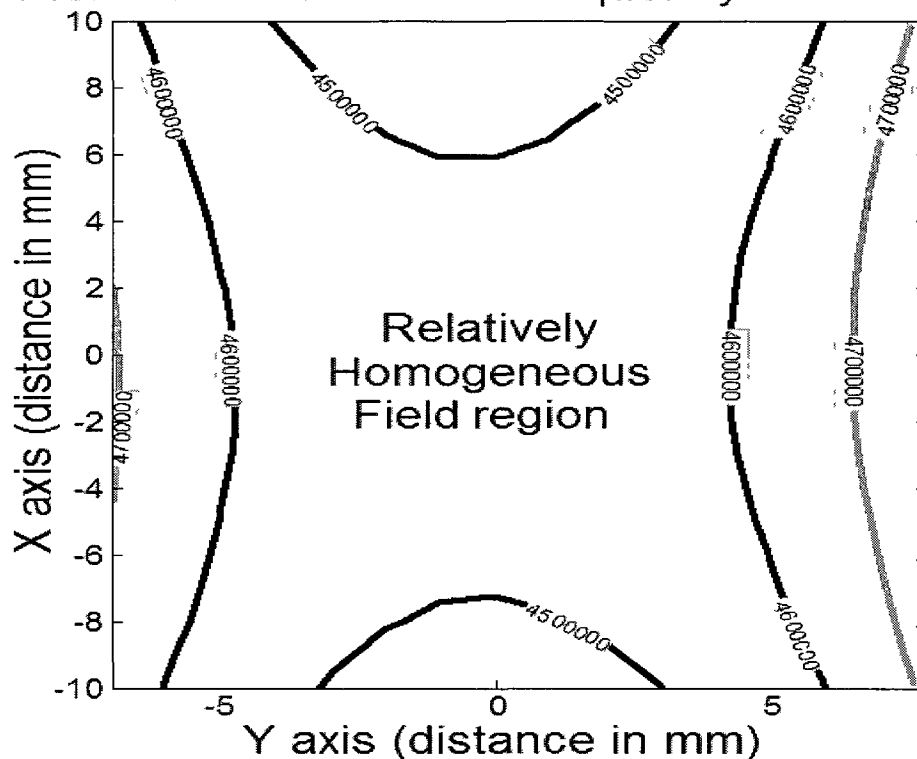


Figure 3.7: 2D profile of relatively homogeneous field magnets (Centre magnet's height is 0.4 cm below the scanner's surface)

### 3.2 Probe and transmitter - receiver unit

The spectrometer unit allows many types of probes to work for wide range of measurement frequencies with highly linear fast signal detection [84]. The SPS's device resonance frequency is calculated using equation  $f_0 = \frac{\gamma}{2\pi} |\vec{B}_0|$ , where the scanner's static magnetic field strength  $|\vec{B}_0|$  is 0.10687T and  $\frac{\gamma}{2\pi}$  for  $^1\text{H}$  atom being 42.58 MHz/T. The

resulting resonant frequency of 4.55 MHz is required to design the tuning and protection circuitry discussed below.

### 3.2.1 Probe

The NMR probe circuit consists of an inductive coil which generates the  $\vec{B}_1$  field, tuned to resonance at the NMR frequency, and matched to a  $50\Omega$  cable. A single cable is used for both signal transmission and reception. The resonance condition is given by equation 3.0 where  $L$  is the inductance,  $C$  the capacitance, and  $\omega_{\text{oscillation}}$  the frequency of oscillation.

$$\omega_{\text{oscillation}} = 1/\sqrt{LC} \quad (3.0)$$

The SPS probe is composed of two coils, capacitors, a cable and plexi glass housing as shown in figure 3.8 the two coils act as a transformer, with the primary connected to the cable and the secondary to the capacitors. The capacitors tune the coil to resonance and the transformer transforms the impedance to  $50\Omega$ .

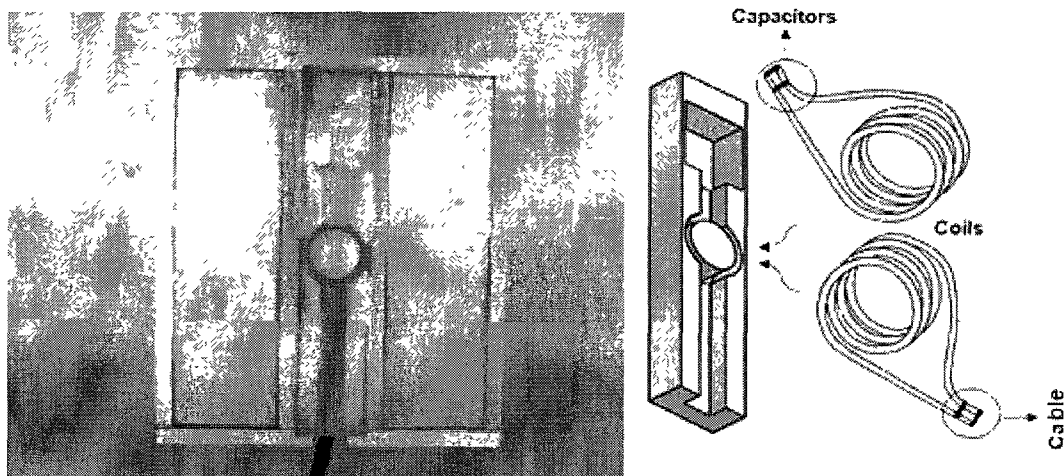


Figure 3.8: The probe

Figure 3.9 describes the circuit diagram of the probe. The thickness and the number of turns in one of the coil that is attached to capacitor equal to 0.45cm, and 5 respectively. The diameter of both coils is 1.4cm, thus the values of the capacitors being around 1125pF. The second coil turns and thickness are 2 and 0.18cm. The resistor R represents the small resistance in the wire. The probe is a tuned device, yet the preamplifier is broadband. To prevent signal loss and obtain the best sensitivity, the probe and preamplifier are both matched to the same effective input impedance  $Z_T$  of  $50\Omega$  corresponding to the characteristic impedance of the coaxial cables employed [87]. Probe tuning was made possible using swept frequency impedance meter and by adding or removing capacitors at the coil terminal to arrive at 4.55MHz Larmor frequency.

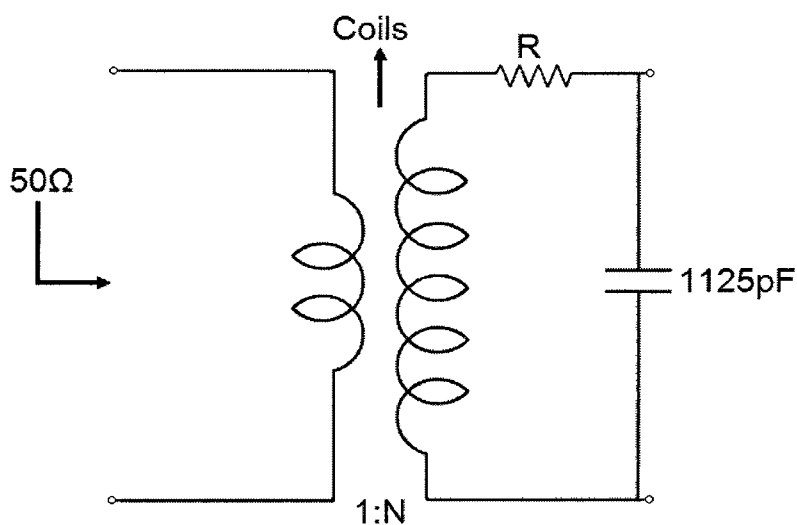


Figure 3.9: NMR probe circuit diagram

### 3.2.2 Transmitter - receiver protection circuitry

A narrowband low-noise amplifier circuit was constructed to condition the NMR signal leaving the probe, before it entered the spectrometer. This newly built receiver unit is shown in figure 3.10 and consists of a 15V power supply unit, quarter wavelength

protection circuits, and low noise RF preamplifier. The high power RF amplifier and the voltage sensitive preamplifier are both connected to the same RF coils and in order to protect the preamplifier from being damaged during high power RF pulse transmission, it is required to implement the simple well known  $\lambda/4$  arrangement of passive transmitter and receiver separation based on wave propagation properties of coaxial cables and the switching capabilities of fast diodes [88].

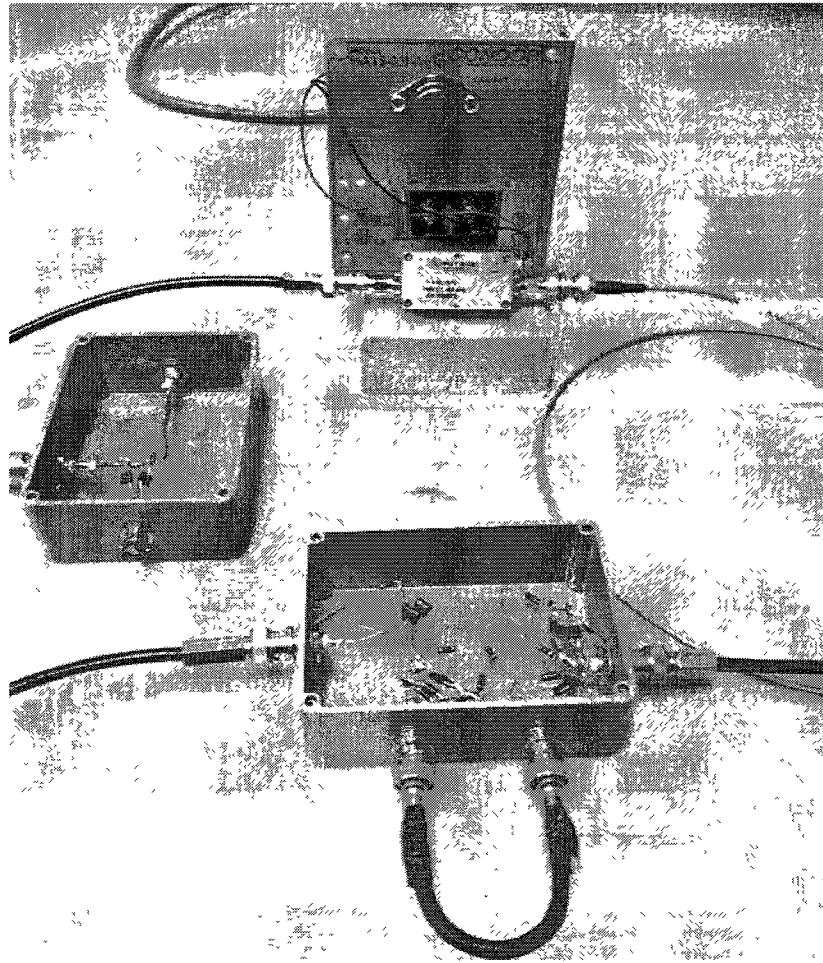


Figure 3.10: SPS's transmitter-receiver unit

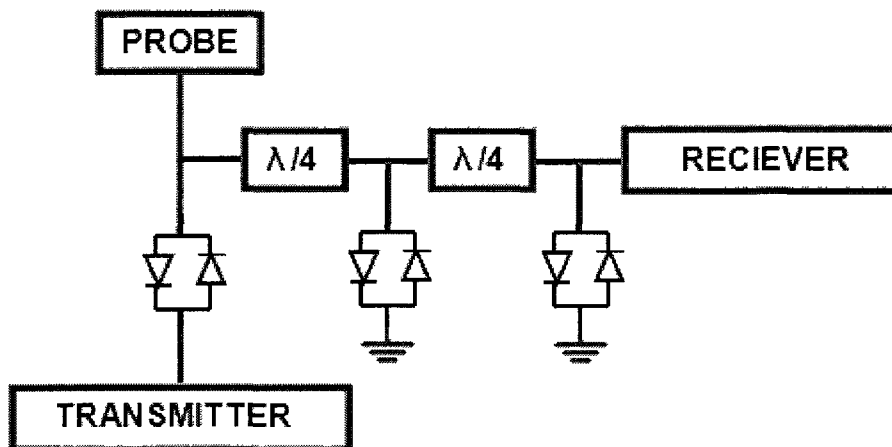


Figure 3.11: The transmitter-receiver protection circuitry

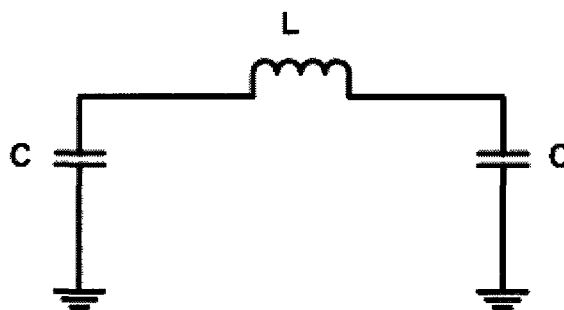


Figure 3.12: The  $\lambda/4$  circuit

Figures 3.11 and 3.12 illustrate the quarter wavelength protection circuit. When the transmitter is on, all diodes conduct. The set of crossed diodes that is located closer to the side of the transmitter would allow the high power RF pulse to go through to the RF coil. The two sets of crossed diodes on the right hand side of the figure become short circuits to ground. Seen through the quarter wavelength circuits, these shorts are impedance transformed to open circuits. The result is that no signal flows to the receiver. On the other hand when the transmitter is off, during the receiving phase all diode switches are open and the NMR signal is prevented from entering the RF power amplifier while being conducted to the preamplifier through quarter wavelength transmission cable

[87]. The values of capacitors and inductors during this circuit design were calculated using equation 3.1 and equation 3.2 where  $Z_T = 50\Omega$  and  $f_0 = 4.55\text{MHz}$

$$L = \frac{Z_T}{2\pi f_0} \quad (3.1)$$

$$C = \frac{1}{2\pi f_0 Z_T} \quad (3.2)$$

### **3.3 Linear positioning system**

The linear positioning system was used to move the hall probe when making magnetic field measurements, and to move the sample when generating the single pixel images shown later. It is composed of linear motion hardware along with motion controller.

#### **3.3.1 Linear motion system components**

The positioning system shown in figure 3.13 contains major components such as carriages, lead screws and motors. A stepper motor is characterized by high torque, low speed and minimum vibration. It is the method of choice for applications requiring quick controlled positioning over a short distance besides it can be accurately driven by control signals without the need for position determinant feedback devices. Motion by stepper motor is created when changes to the polarity of the current that passes through the coils occurs thereby influencing the rotor to which the shaft of the motor is connected [89] and the rotational motion is then transformed into linear movement of a carriage along the lead screw.

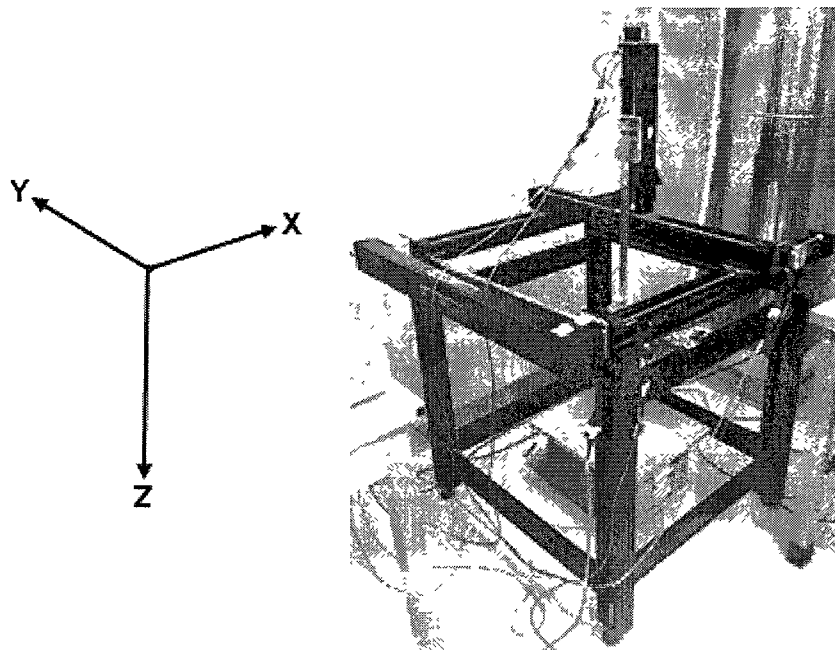


Figure 3.13: Linear motion system

### 3.3.2 Motion controller

Custom built software was designed to manage the positioning system through motion controller shown in figure 3.14. The position system is controlled through commands given by the computer serial port. Position system control was implemented both through ExpSpel, allowing sample movement to be incorporated in NMR imaging experiment, and through figure 3.15 Matlab software for magnetic field mapping.

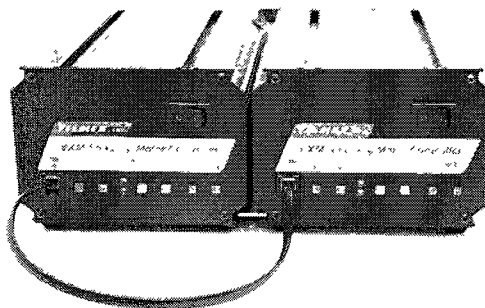


Figure 3.14: Motion controller [90]

Connect To		Disconnect	
Motor	Gauss Meter	Motor or (and) Gauss Meter	
1D Scans			3D Scan
X	Y	Z	XYZ
2D Scans			
XY	XZ	YZ	
Distances & Steps			
	X	Y	Z
Distance In cm	0	0	0
Step Size In cm	0	0	0

Figure 3 15:  $\vec{B}_0$  field mapping software

### 3.4 NMR measurement calibration

The initial step of the NMR experiment was discovering the RF pulse width that will give the strongest NMR signal. Using mineral oil sample and procedure recommended by the spectrometer manufacturer, the SPS device was prepared for measurement by adjusting all the necessary parameters to stable operating conditions and tuning to correct the  $90^0$  and  $180^0$  pulse lengths for 4.55 MHz resonance condition. After experimenting with various  $90^0$  RF pulse lengths, the  $8\mu\text{s}$  pulse with 0db attenuation produced the tallest time domain signal meaning the strongest signal.

### 3.5 Observing NMR signal

In order to ensure proper operation of the measurement setup, several simple NMR experiments were performed, using figure 3.16 arrangement.

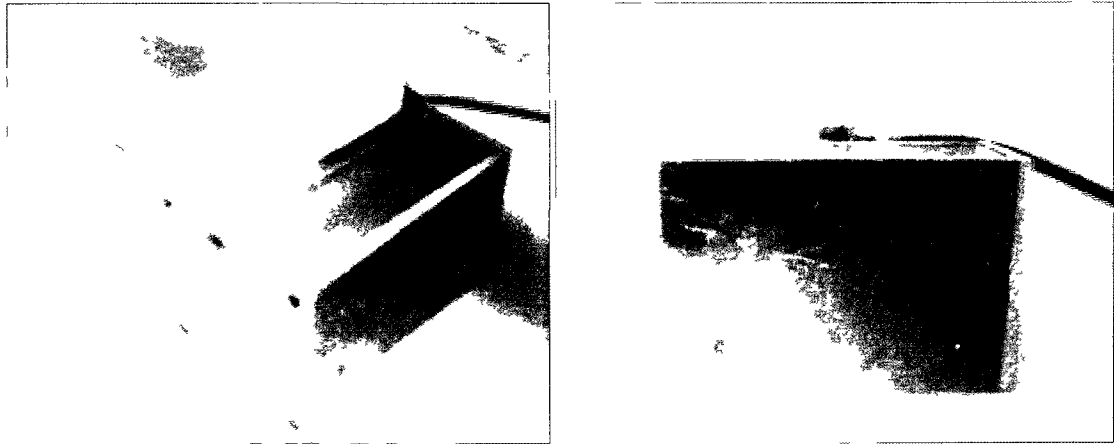


Figure 3.16: Measurement setup using relatively homogeneous field magnets

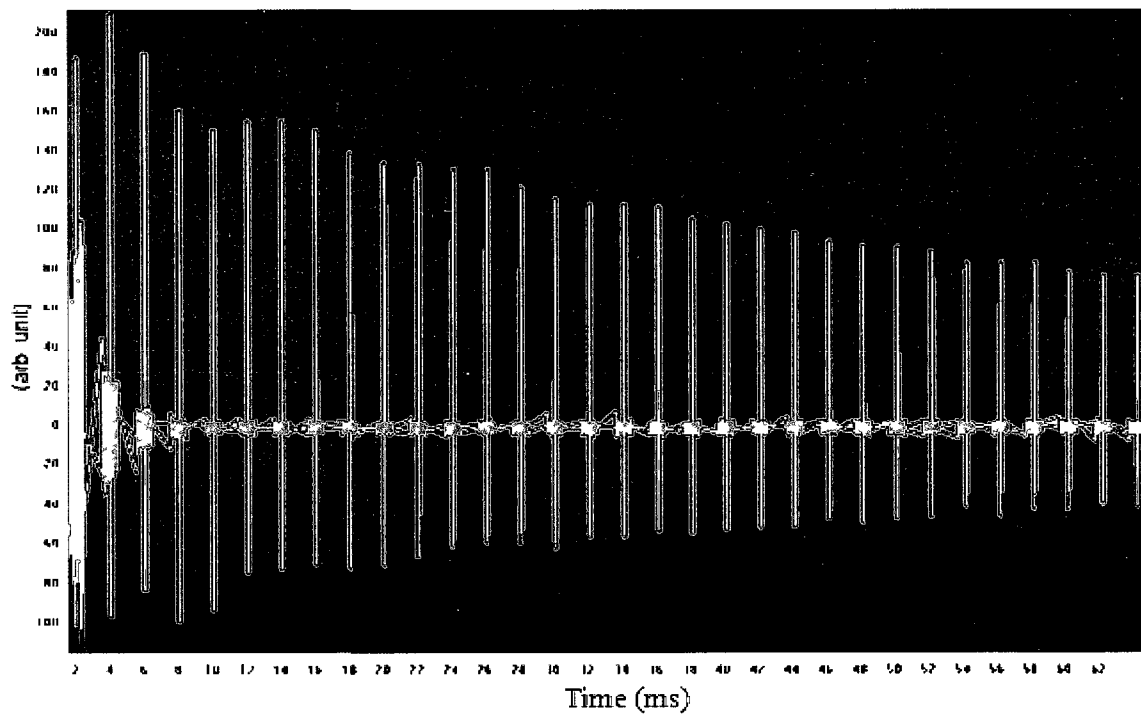


Figure 3.17: The CPMG of mineral oil sample. The real part of the signal is shown in red and the imaginary in yellow

Figure 3.17 shows a time series recorded from a CPMG measurement of mineral oil. The experimental parameters were pulse width =  $8\mu\text{s}$ , echo time =  $0.04\text{ms}$ , acquisition time =  $0.01\text{ms}$ , recycling delay =  $0.1\text{s}$ , attenuation =  $0\text{db}$ , NMR frequency =  $4.55\text{MHz}$ , data points = 1024, number of echoes = 32, and number of scans = 256. The individual spin echoes intensity decline is related to  $T_2^*$ , while the CPMG decay corresponds to  $T_2$ .

In order to eliminate undesirable signal contributions, the real and imaginary parts of the data were filtered with custom made low pass filter and cutoff frequency of 125 kHz. Ensemble averaging technique was also employed to give single representative echo. Figure 3.18 and figure 3.19 describe the real and imaginary parts, and magnitude plot of the averaged echo respectively.

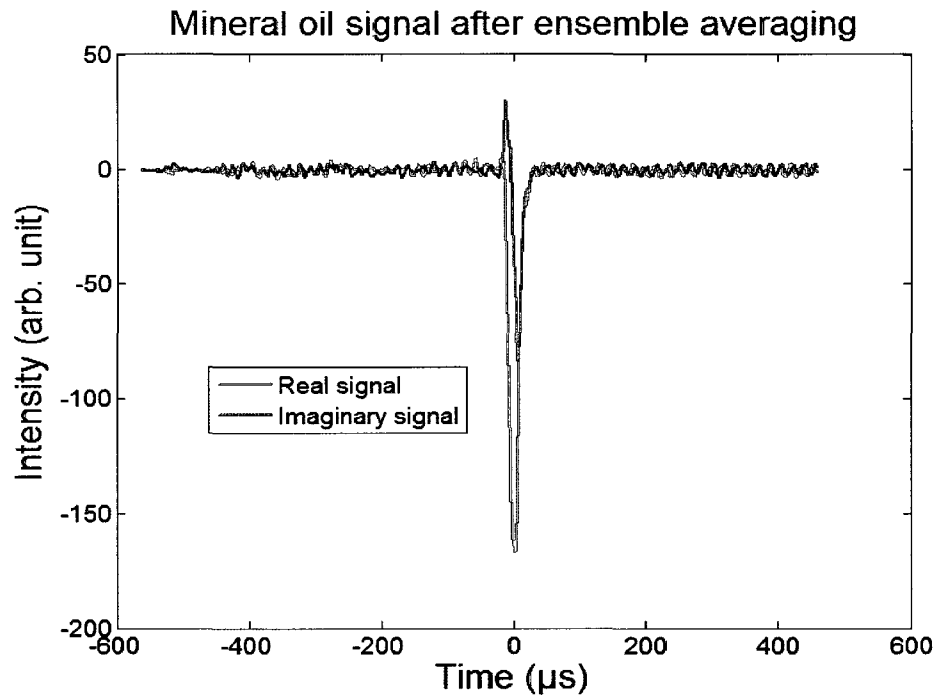


Figure 3.18: Mineral oil signal after ensemble averaging

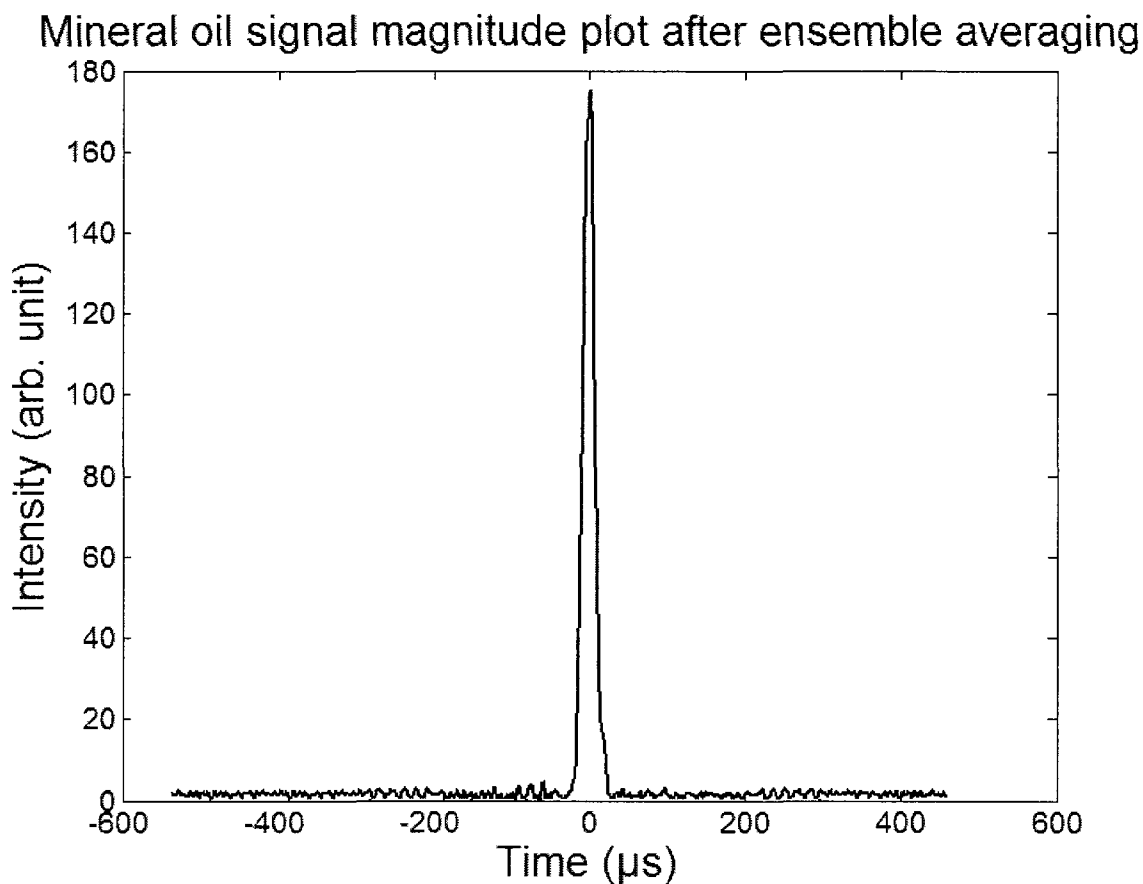


Figure 3.19: Mineral oil magnitude plot after ensemble averaging

### 3.6 Finding the gradient of homogeneous field magnets

Although the magnetic field is nominally homogeneous at the centre of the sensitive spot, it does vary with position as seen in figure 3.4. The spatial inhomogeneity of the field can be characterized by an effective gradient. Knowledge of this gradient is necessary to understand the NMR signal characteristics, for example when measuring liquid self diffusion. The simplest way to find this gradient information would be through reverse process in which a diffusion measurement can be carried out for a water sample using the already known  $2.4 \times 10^{-5} \text{ cm}^2 \text{ s}^{-1}$  water diffusion coefficient and SGSE's

normalized signal attenuation equation 2.19. Afterwards diffusion experiments can be performed for any types of sample once the G estimate is established.

A diffusion study was conducted using CPMG procedure, so as to find the NMR signal intensity  $\ln(I)$  of a water sample. The initial measurement started for  $\tau$  equals 0.2 ms and the operation was repeated while incrementing the  $\tau$  value by 0.05 ms up to and including 0.75ms. During each  $\tau$  assessment the CPMG signals were filtered and ensemble averaged to represent the observed signals with a single echo and the maximum value of this echo was taken as the intensity  $\ln(I)$ . The Figure 3.20 plot  $\ln(I)$  versus  $\tau^3$  symbolizes equation 3.3 where  $\ln(I_0)$  is y intercept and  $-2/3\gamma^2 G^2 D$  the slope.

$$\ln(I) = -2/3\gamma^2 G^2 \tau^3 D - \ln(I_0) \quad (3.3)$$

$$-2/3\gamma^2 G^2 D = \text{The slope of the diffusion curve} \quad (3.4)$$

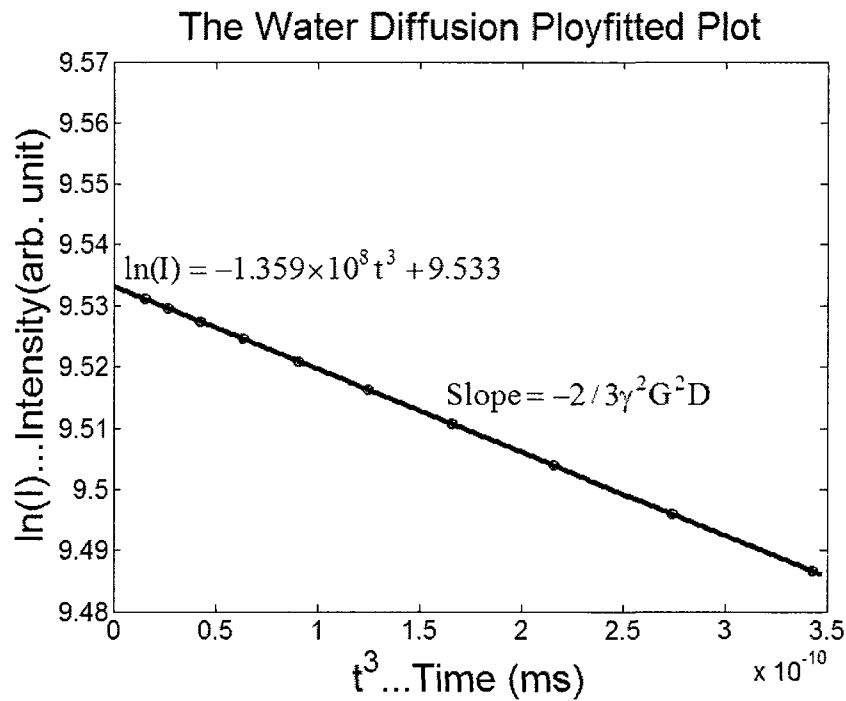


Figure 3.20: Diffusion measurement of water

The gradient  $G$  is calculated using equation 3.4 and the already known values of  $\gamma$ ,  $D$  and figure 3.20 diffusion curve slope, thus the result reveals the SPS's gradient to be 1.09 T/m.

### **3.7 Pulse width effects**

The excitation profile of the SPS was modeled using mineral oil sample and various width of rectangular pulse; comparison between selective and nonselective excitation can be made on the basis of the plots in figure 3.21. As the plots indicate a short RF pulse excites wide frequency band while the long pulse is capable of exciting a narrow frequency region. During the calibration process the  $8\mu\text{s}$  pulse generated the strongest signal, therefore the excitation experiment started at this pulse width. The procedure was repeated up to and including  $512\mu\text{s}$  pulse by doubling the pulse width while adding 6db to the previous attenuation value, to halve the pulse intensity. The other experimental parameters were echo time = 0.9ms, acquisition time = 0.3ms, recycling delay = 0.12s, NMR frequency = 4.55MHz, data points = 1024, number of echoes = 64, and number of scans = 256. In each of the measurement the observed spin echoes were filtered and ensemble averaged to find the single echo that best represents the particular pulse width. The time domain plot signifies the width of sample excitation grew with increase in RF pulse width, conversely the corresponding frequency domain exhibits the  $512\mu\text{s}$  RF pulse have the narrowest frequency band.

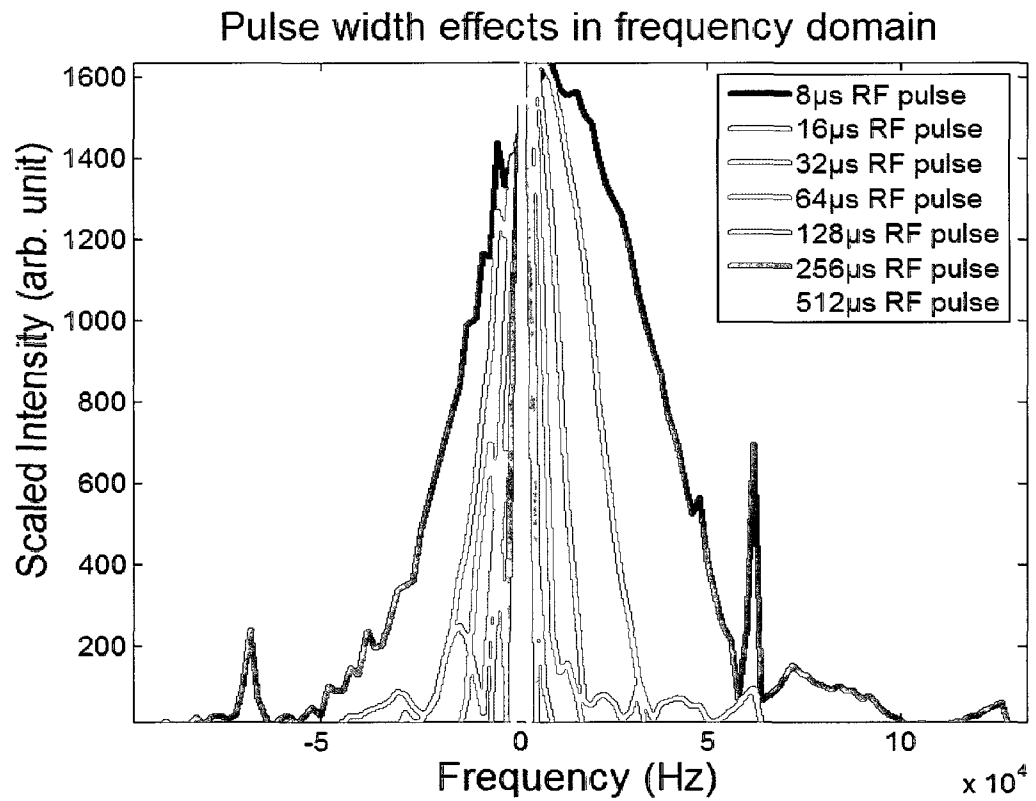
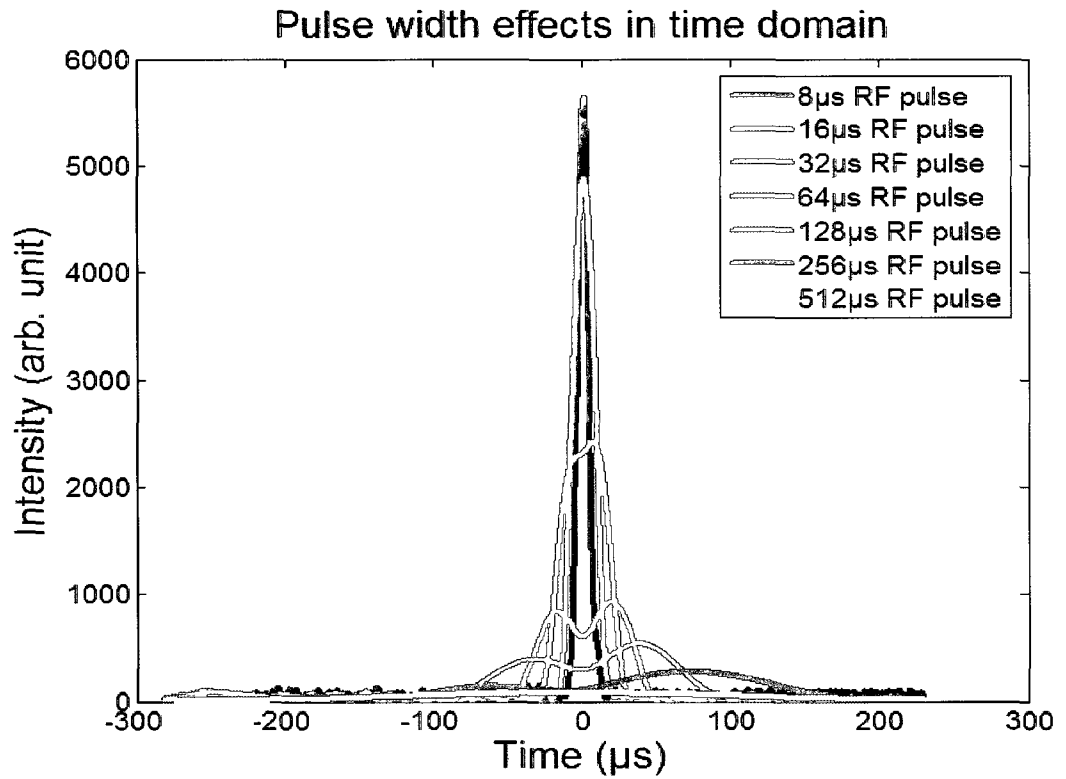


Figure 3.21: The excitation profile of SPS

## Chapter 4.0 Experimental results

The imaging section discusses how to find spatial resolution of homogeneous field magnets. The spectroscopy section on the other hand discusses multi-frequency selective excitation and presents the experimental results of single and multi-frequency selective excitation.

### 4.1 Imaging

A goal of this thesis was to use shaped pulses to improve the spatial resolution of imaging scans performed with the SPS. A 1D imaging scenario is illustrated in figure 4.0 the sample, in this case a bottle of mineral oil, is moved incrementally across the scanner. With perfect resolution, we expect no signal for all points measured before the mineral oil is over the probe and a constant signal level once the mineral oil is on the top. Thus, the ideal image profile would be a step function as shown in the following figure.

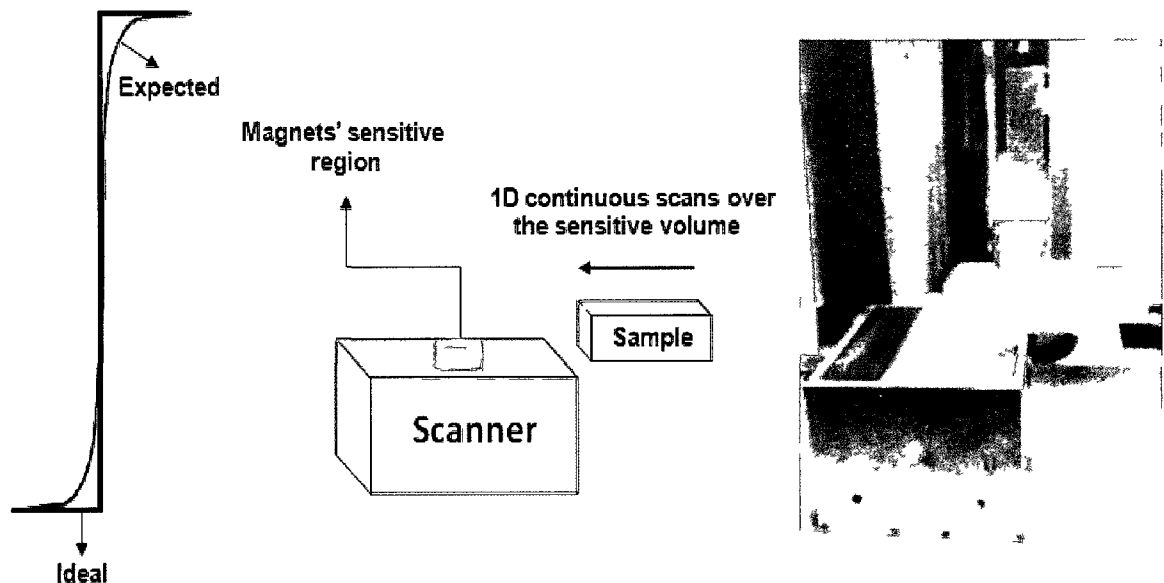


Figure 4.0: The ideal, expected edge response plot and 1D continuous scan

In reality, the sensitive area of the scanner has a finite size. This size is governed by the inhomogeneity in the static field, and the bandwidth of the excitation. For example as figure 4.1 indicates a short 8  $\mu\text{s}$  pulse will have relatively high bandwidth and will therefore excite a large region of space than a longer 64 $\mu\text{s}$  pulse.

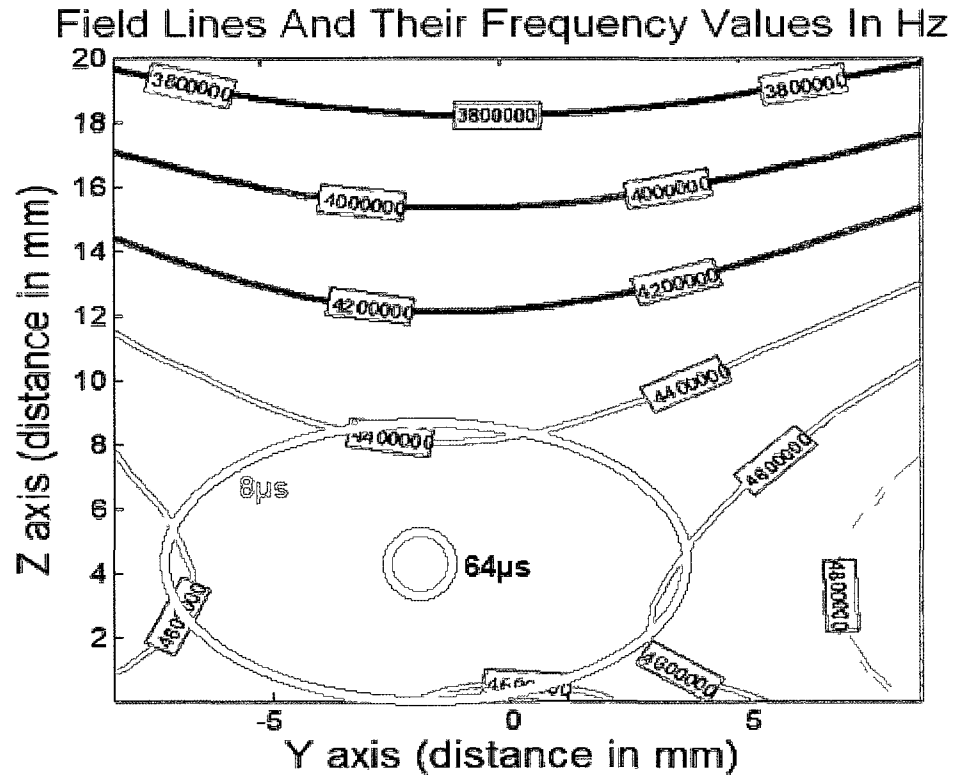


Figure 4.1: Contours corresponding to two different pulse lengths

The effect of the excitation area size is a blurring of the step function profile. There will be a transition region where the sample is partially in the sensitive volume, and the profile will have a rise time equal to the width of this volume. Longer pulses will excite a smaller volume, resulting in a higher resolution. The tradeoff is a lower SNR, as the amount of signal available depends on the excitation volume.

The figure 4.2 exhibits edge response plots for different RF pulse widths. For each pulse length experiment a total of 37 measurements were performed, where each

measurement had experimental parameters such as echo time = 0.15ms, acquisition time = 0.04ms, recycling delay = 0.1s, NMR frequency = 4.55MHz, number of echoes = 64, and number of scans = 256. The 8 $\mu$ s pulse was assigned 0db attenuation and whenever the pulse length was doubled the new attenuation setting equals the previous attenuation value plus 6db. A low pass filter is designed based on the size of the RF pulse width to eliminate undesirable signal contributions and the real and imaginary parts of the spin echoes were ensemble averaged to find the maximum signal intensity of individual measurements. As the graph indicates the edge response curves got steeper as the pulse width increased. In the case of 8 $\mu$ s pulse (red) we see a broad response, however for a much longer 64 $\mu$ s pulse (cyan), the transition is much sharper although it is noted that the noise level has increased significantly.

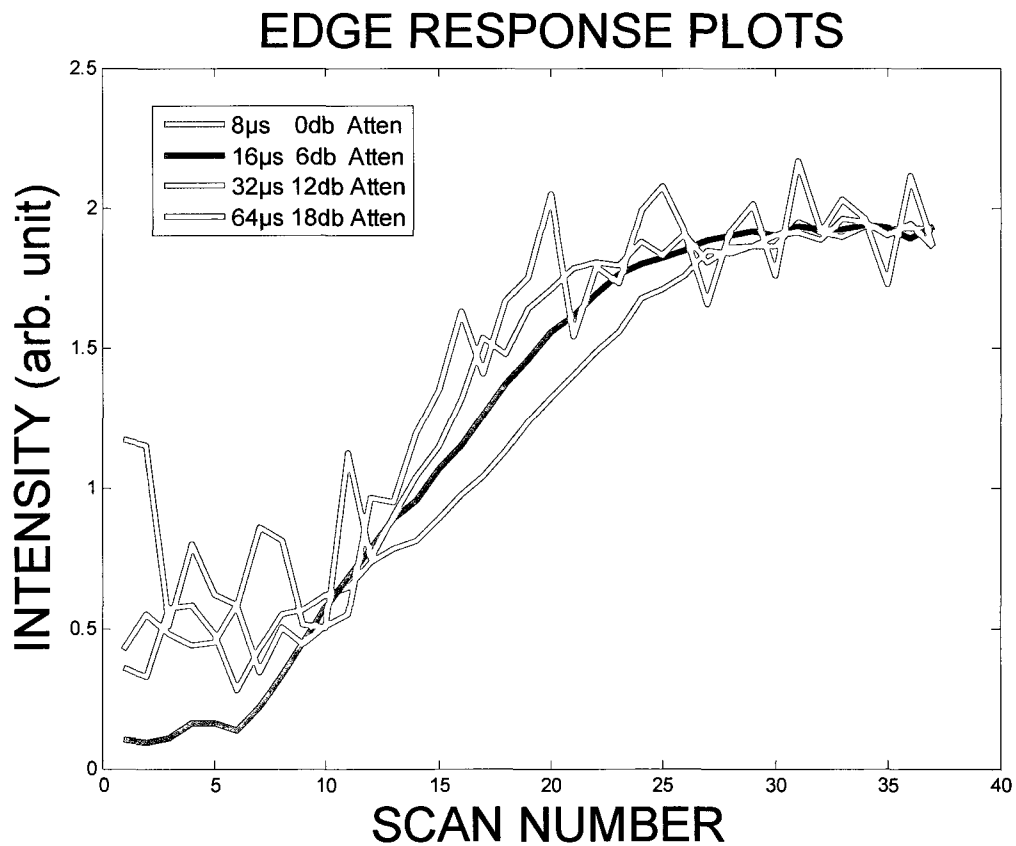


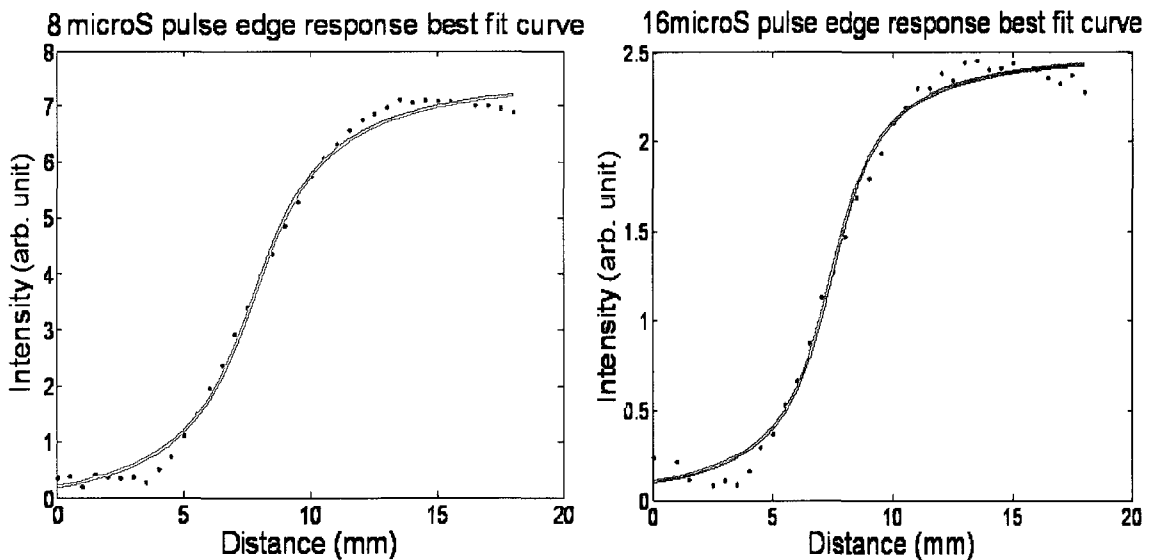
Figure 4.2: The not best fitted edge response curves

It is common in NMR data analysis to assume that signal spectra have a Lorentzian distribution. Using this approximation, the profiles recorded would follow an inverse tangent function. Custom made curve fitting software was designed using equation 4.0. The amplitude and baseline offset A and D are obtained from the collected NMR data, on the other hand B and C are found by solving equation 4.1

$$y = A \tan^{-1}(B(x - C)) + D \quad (4.0)$$

The least squares criterion has important statistical interpretations, if reasonable probabilistic assumptions about the underlying error distributions are made the least squares give rise to the maximum likelihood estimate of the parameters. The technique entails summing all the square of the distances from each data point to the curve and the plot that minimizes the summation result is then chosen to fit the data points [91, 92]; hence the least square error method of equation 4.1 can be applied to find the unknown variables. The figure 4.3 and 4.4 are the best fit curves for edge response data.

$$[BC; B]=\text{Inv}([n, \sum xi; \sum xi, xi^2]) * ([\sum \tan((y_i - D)/A); \sum (xi * \tan((y_i - D)/A))]) \quad (4.1)$$



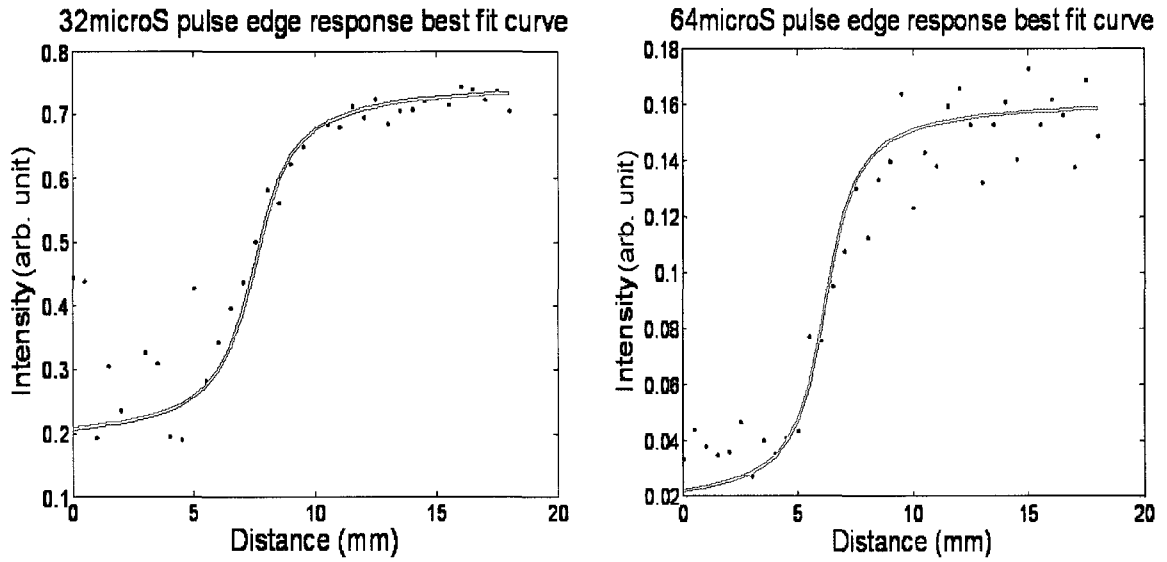


Figure 4.3: Mineral oil edge response best fit curves

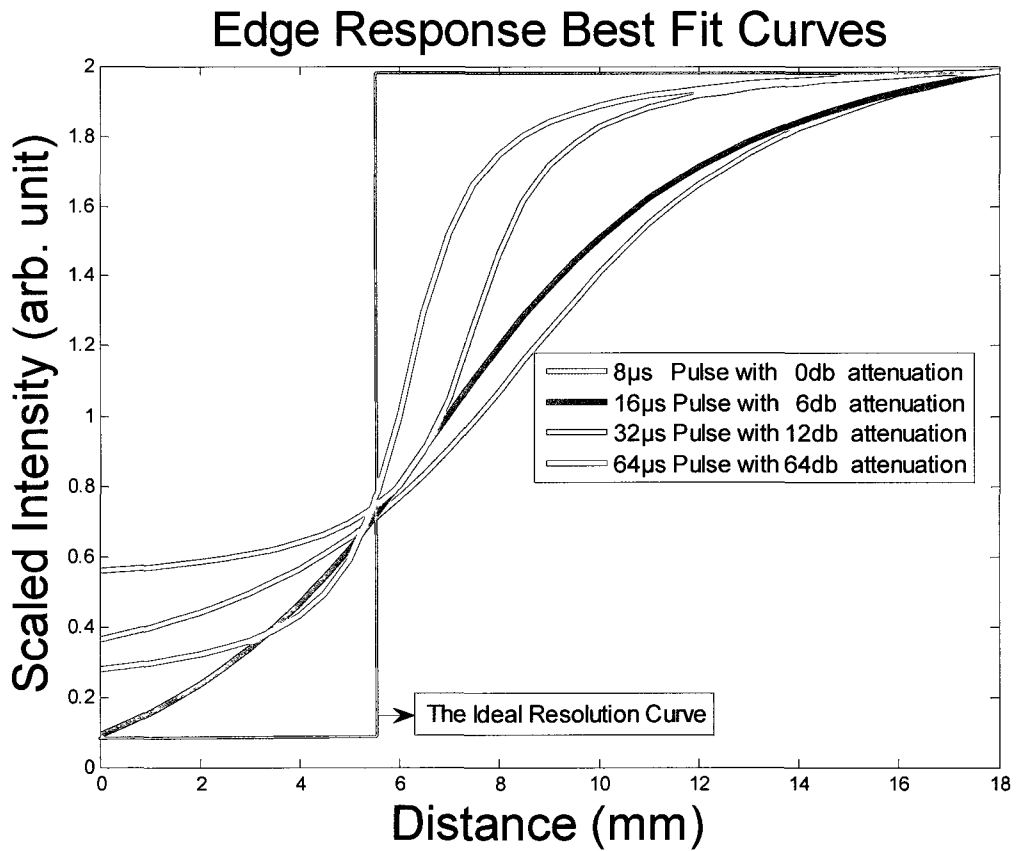


Figure 4.4: Mineral oil edge response best fit curves put together

### 4.1.1 Finding spatial resolution of homogeneous field magnets

Equation 4.2 is the first derivative of the arc-tangent and it represents the Point Spread Function (PSF), the usual descriptor of image resolution.

$$y' = \frac{A(1/B)}{(x-C)^2 + (1/B)^2} \quad (4.2)$$

This Lorentzian distribution describes resonance behavior similar to those found in mechanical or electron oscillator, besides the NMR spectra that are typically displayed as an absorption spectrum have Lorentzian shape. It is conventional to normalize the Lorentzian function according to

$$L = \frac{A}{\pi} \frac{\Gamma/2}{(\omega - \omega_0)^2 + (\Gamma/2)^2} \quad (4.3)$$

The normalized Lorentzian function is given by equation 4.3, where parameter  $\Gamma$  specifies FWHM and  $\omega_0$  the resonant frequency [93]. Spatial resolution of SPS can be found analytically using the PSF; once constants B and C are found using the least square error method the next step would be to formulate the PSF. Equation 4.4 and 4.5 reflects the 64 $\mu$ s pulse edge response best fit curve and PSF respectively.

$$y = 0.047014 \tan^{-1}(1.0382(x - 6.4237)) + 0.088864 \quad (4.4)$$

$$y' = 0.047014 (1/1.0382) / (x - 6.4237)^2 + (1/1.0382)^2 \quad (4.5)$$

The equation 4.5 can be correlated to the normalized Lorentzian function to yield FWHM.

$$\Gamma/2 = 1/1.0382; \quad \Gamma = 1.9\text{mm}$$

FWHM can also be found from figure 4.5 by measuring the width at half height.

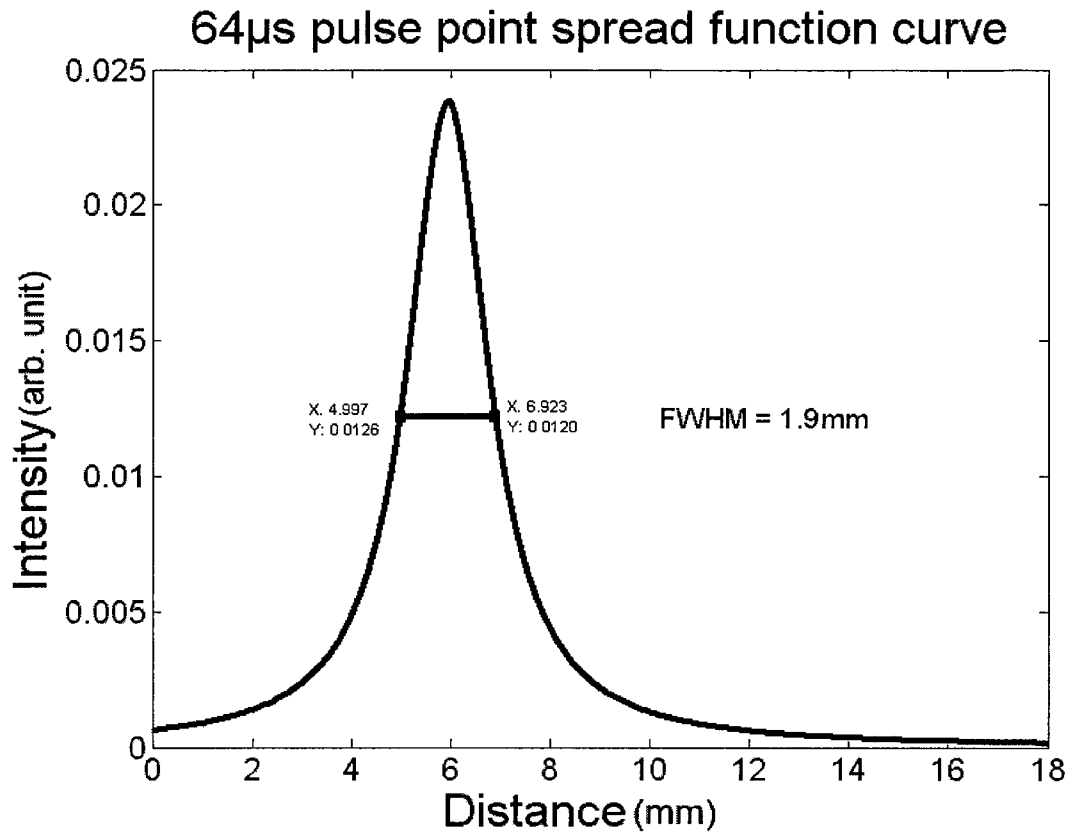


Figure 4.5: Point Spread Function of 64µs pulse

Because the sensitive region is defined by  $\vec{B}_0$ , the size of the RF coil is not a factor, as long as it excited an area larger than that defined by the static field. However, it is still possible to further enhance the spatial resolution of the scanner by improving the sensitivity of the RF coils. The following table 4.0 summarizes the spatial resolution of SPS for various RF pulse widths.

Pulse width (µs)	FWHM (mm)
8	6.7
16	5.2
32	2.2
64	1.9

Table 4.0: Spatial resolution for various RF pulse widths

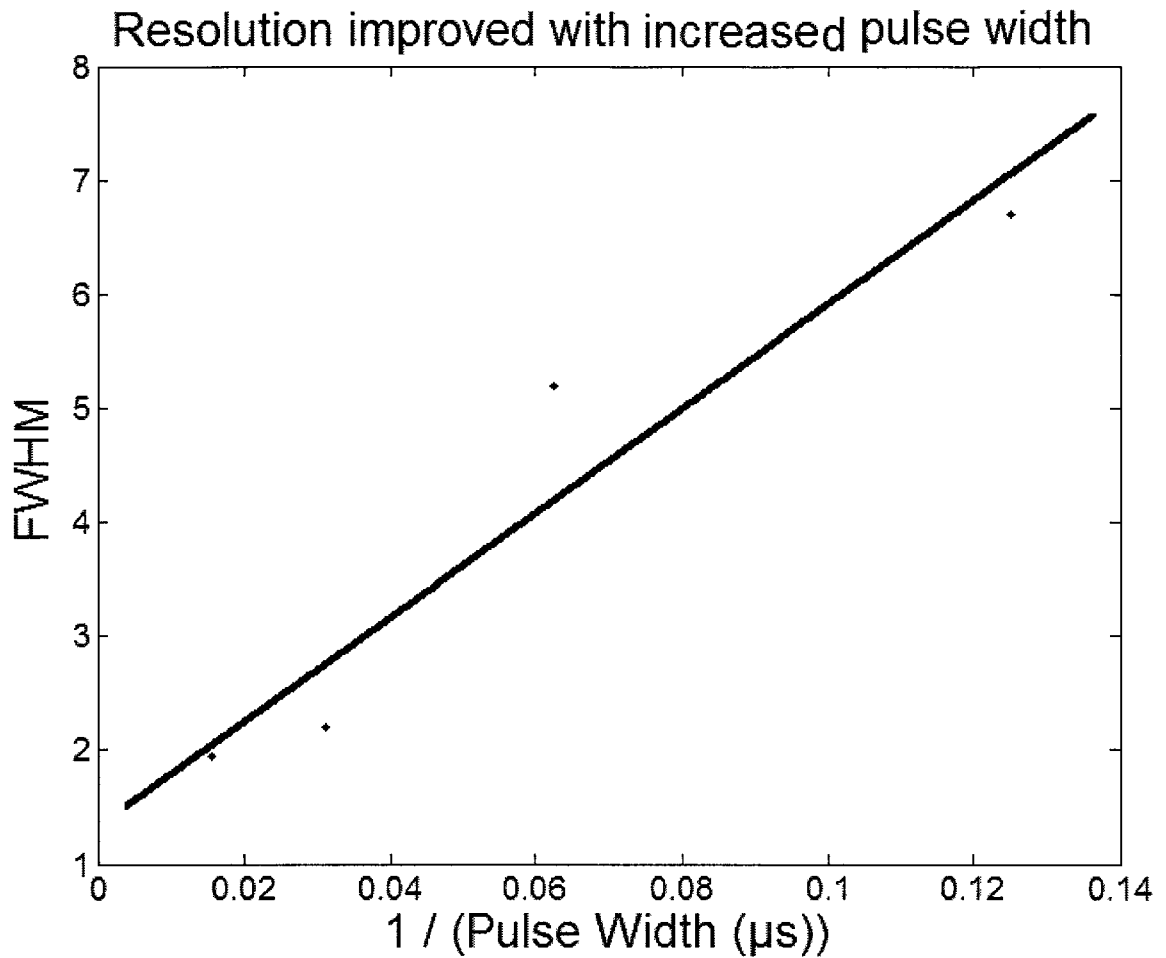


Figure 4.6: The plot of spatial resolution versus pulse length

We can see that as the pulse length increases, so does the spatial resolution. This is expected, as the excitation bandwidth is inversely proportional to the pulse length. Figure 4.6 indicates that there is an apparent linear relationship between the PSF FWHM and the inverse pulse length. Nevertheless, in order for this finding to be valid, the magnetic field gradient is assumed as being constant within the sensitive volume. This result indicates that increasingly high resolution is possible by decreasing the excitation bandwidth. However, as pulse length increases, the image SNR decreases. This could be

compensated by increasing the number of scans, but would result in prohibitively long experiments at very high resolutions.

It is most desirable to decrease the bandwidth while preserving the high SNR associated with shorter pulse lengths. One possible method is to excite many narrow bandwidth spectra, each with a distinct center frequency, simultaneously, and average them in frequency domain. The result is one narrow spectrum, but with an SNR commensurate with a much wider excitation bandwidth. While this is not possible in an imaging context, the idea is well suited to spectroscopy, as discussed next.

## **4.2 Spectral resolution**

This chapter discusses excitation strategies of very narrow frequency bands and in order to assess the efficiency of the newly developed sinusoidal composite pulse sequence, the SNR of single frequency is compared with the multi-frequency selective method; in both of these two experiments a water / oil emulsion (margarine) sample has been examined.

### **4.2.1 NMR excitation by multi-frequency selective pulse**

We have seen previously that in the inhomogeneous field of the NMR sensor being used, a pulse will excite a bandwidth inversely proportional to its length. The resulting NMR signal will be short lived, on the order of the length of the pulse; as a result, any phenomena, for example diffusion or chemical shift, which occur on a time scale much longer than the pulse, cannot be observed. In the frequency domain, this means that the frequency resolution is limited to the pulse bandwidth.

In order to observe phenomena that change slowly with time (low frequency), it is advantageous to excite a very narrow frequency strip compared to a wide band. Of course this will significantly diminish the measurement SNR. In order to dramatically improve the SNR of MR systems it is quite beneficial to excite many narrow frequency regions simultaneously. This thesis's multi-frequency selective pulse sequence could produce measurement results that represent step forward towards those of traditional scanners.

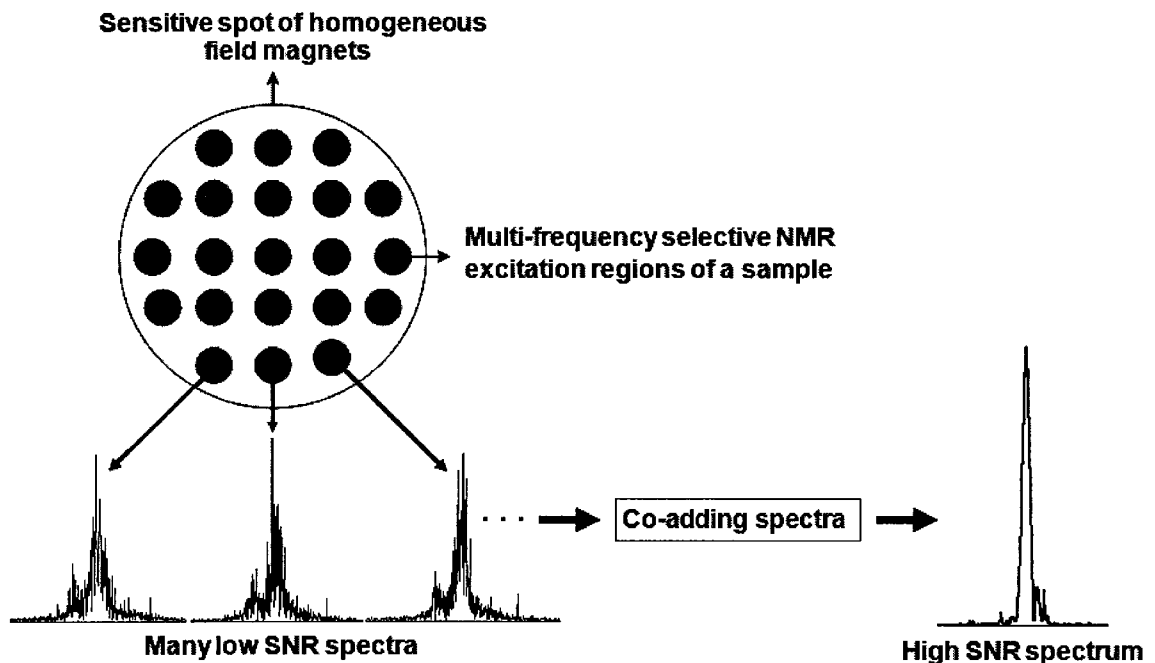


Figure 4.7: Illustration of multi-frequency selective NMR excitation

Narrow frequency bands (dark circles) are excited at many positions, corresponding to several different center frequencies. Each spectrum is noisy, due to the limited sample volume being excited. The individual spectra are then co-added, resulting in a single, narrow spectrum, with increased SNR.

Figure 4.7 illustrates the concept of multi-frequency excitation. In a regular measurement, a short pulse would simultaneously excite the entire bandwidth (large circle) giving a short lived echo with broad spectrum. In the multi frequency technique, the entire bandwidth is still used, preserving the SNR advantage of a short pulse.

However the excitation volume is divided into a large number of narrow bandwidth regions, each corresponding to a distinct center frequency, and a spectrum is simultaneously recorded from each. These spectra are individually narrow yet noisy. Co-adding signal spectra produces a narrow, yet high SNR spectrum. The shape of the measured spectrum provides vital sample information and this technique preserves spectral shape, while improving SNR.

#### 4.2.2 Graphical illustration of frequency shifted NMR excitation

The following graphical illustrations describe the theory behind the multi-frequency selective NMR excitation. As it was discussed in chapter 2.8.2 the oscillator in the spectrometer generates high power RF signal, subsequently this signal is multiplied by an appropriate finite duration signal to form the desired shaped pulse. The equation 4.6 and figure 4.8 demonstrate how a sinusoidal signal is being multiplied by rectangular function to produce a shaped RF pulse;  $f_m$  is the resonance frequency,  $T$  the pulse width,  $A_m$  and  $A_r$  are amplitudes of the cosine and rectangular pulses respectively.

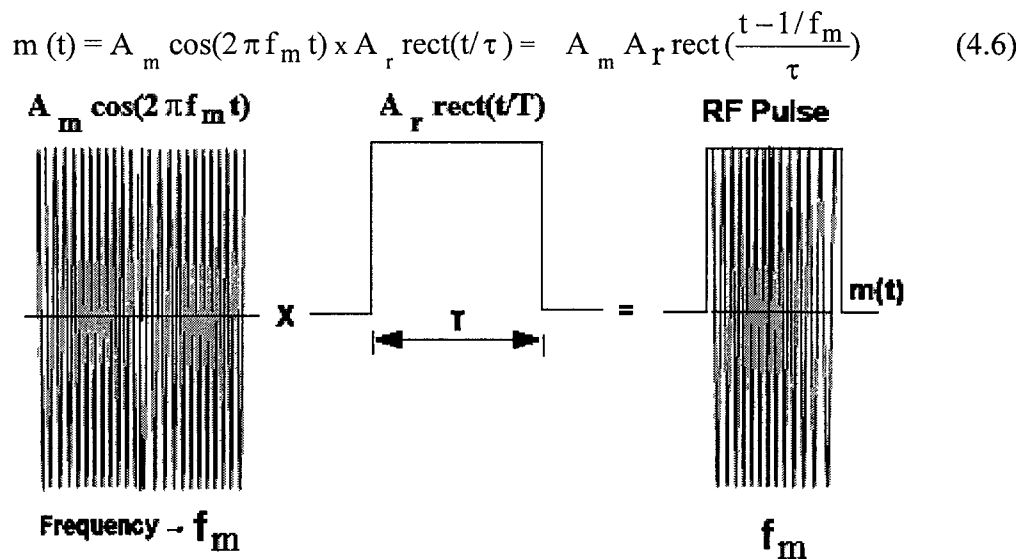


Figure 4.8: The rectangular RF pulse

The fundamental principle behind frequency shifting is to relocate the resonance frequency anywhere within the sample volume to cause multiple NMR excitations. This theory can be exemplified by equation 4.7 and figure 4.9, where the carrier signals  $c(t)$  is amplitude modulated by the rectangular pulse of width  $\tau$ . The expected modulation outcome will be a high frequency sinusoidal with an envelope  $c(t)$ .

$$y(t) = m(t) \times c(t) = A_m A_r \text{rect}\left(\frac{t-1/f_m}{\tau}\right) \times A_c \cos(2\pi n f_c t) \quad (4.7)$$

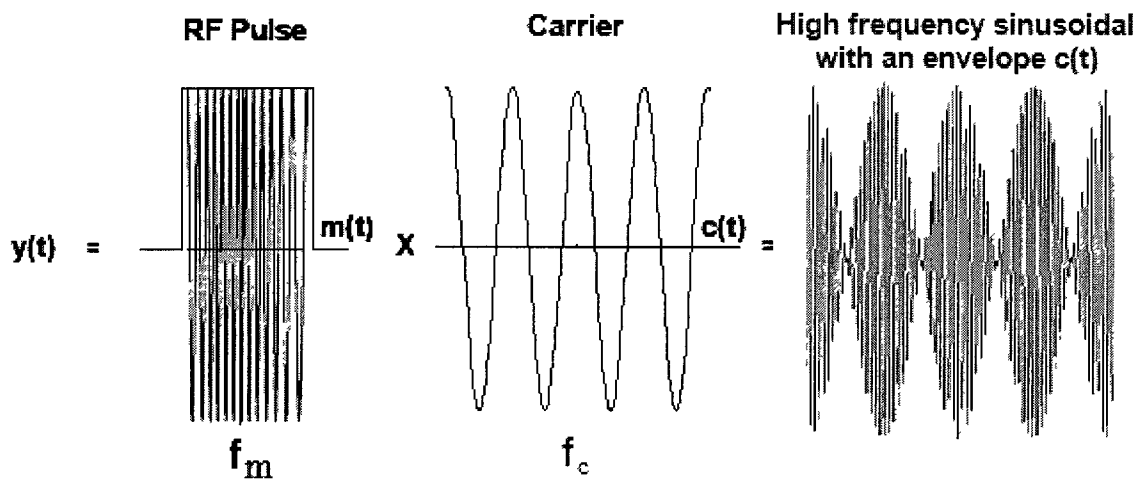


Figure 4.9: Message transmission through variations in the carrier's amplitude

The signals generated by multi-frequency excitation can be more easily explained in the frequency domain. The equation 4.8 and figure 4.10 describe the transformation of the previous time domain signal into the corresponding frequency spectra when the frequency shift multiplier  $n = 1$ . As shown in figure 4.11, the initial NMR excitation occurs at frequency  $f_m$  when  $n = 0$ , likewise when  $n = 1$  after shifting the resonance frequency by  $f_c$ , the same excitation phenomenon is exhibited at  $f_m - f_c$  and  $f_m + f_c$ .

$$Y(f) = A_m A_r T \text{sinc}(\pi f \tau) e^{-j\omega f_m} * \frac{A_c}{2} [\delta(f + f_c) + \delta(f - f_c)] \quad (4.8)$$

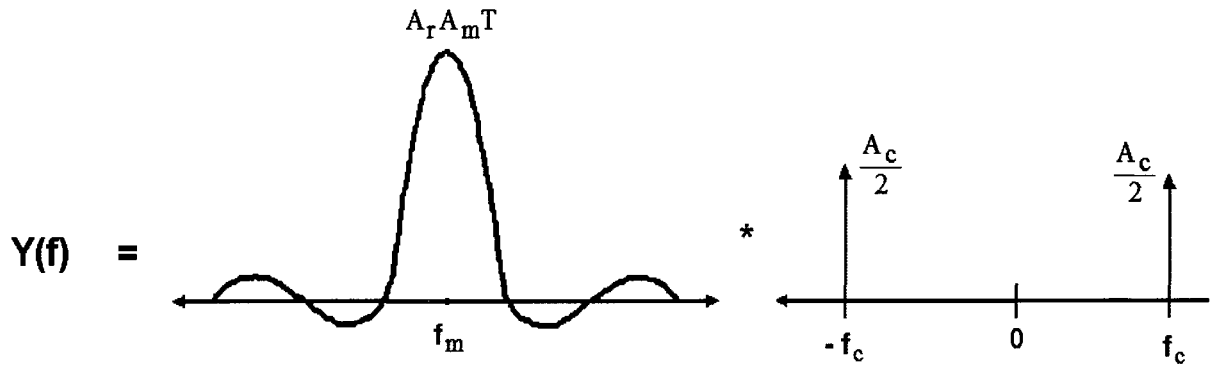


Figure 4.10: Convolution of the rectangular function with a cosine carrier signal

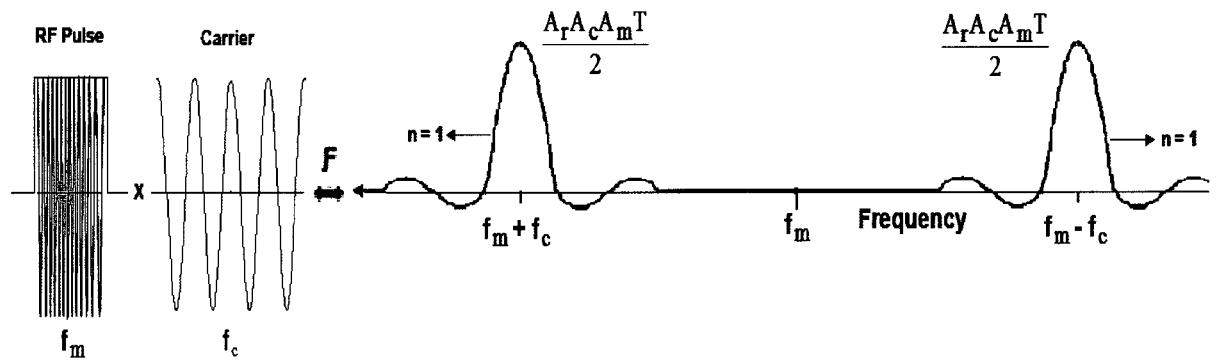


Figure 4.11: NMR excitation by frequency shifts when  $n = 1$

The equation 4.9 and figure 4.12 describe the total spectra, as shown excitations occur at NMR frequency  $\pm n \cdot f_c$ , where  $f_c$  is the distance between two adjacent spectra and multiplier  $n = 0, 1, 2, 3 \dots M$ .

$$Y(f) = A_m A_r T \text{sinc}(\pi f \tau) e^{-j\omega f_m} * [A_c \delta(f) + \frac{A_c}{2} (\delta(f + f_c) + \delta(f - f_c)) + \frac{A_c}{2} (\delta(f + 2f_c) + \delta(f - 2f_c)) + \dots] \quad (4.9)$$

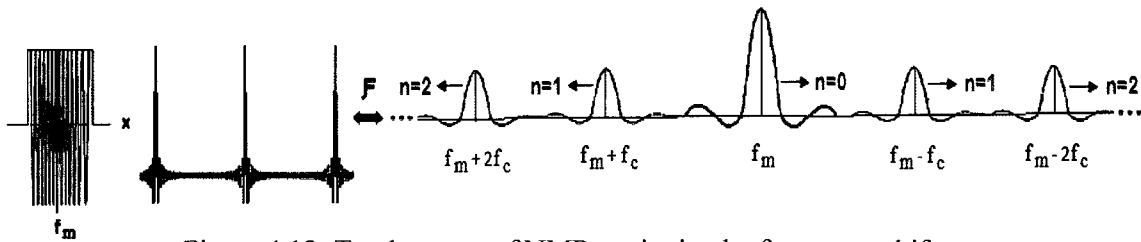


Figure 4.12: Total spectra of NMR excitation by frequency shifts

The system is linear and therefore many carrier frequencies  $c(t)$  can be superimposed the result is comb-like spectrum, consisting of multiple pairs of peaks. Assuming a homogeneous sample, each of the peaks will be identical, and can therefore be co-added. As discussed in the next section, an important pre-requisite to co-adding signal spectra is phase correction, ensuring that each of the complex spectra recorded has identical phase to ensure that they add constructively when put together.

### 4.2.3 Phase correction of NMR spectra

As shown in figure 4.13, the phase of the NMR signal after FT depends on how the echo is centered in the acquisition window [94], and the absolute phase of the oscillators used in demodulation. The Lorentzian distribution is represented by an absorption spectrum of  $0^0$  phase. As shown in figure 4.14 for purpose of phase analysis and correction, any spectra that differ from the base angle of  $0^0$  are classified as spectra with phase errors. The FT of the observed signals is required to have same phase so that the spectra do not cancel out due to phase difference upon co-adding of signal spectra.

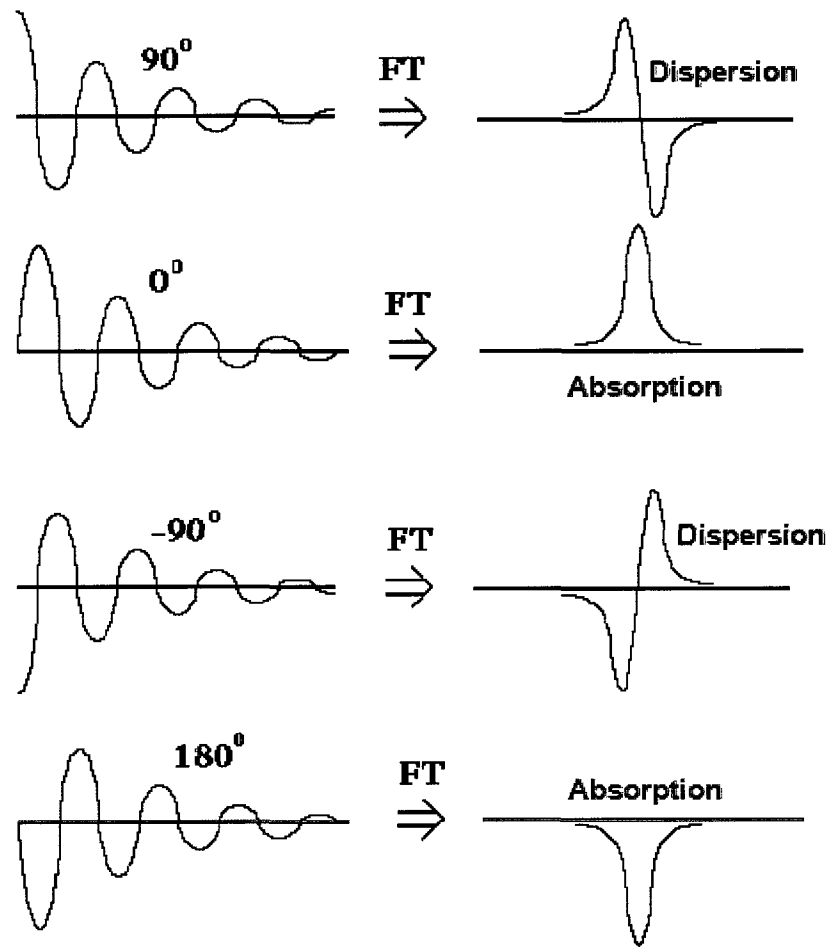


Figure 4.13: Relationship between echo and the phase of a signal [94]

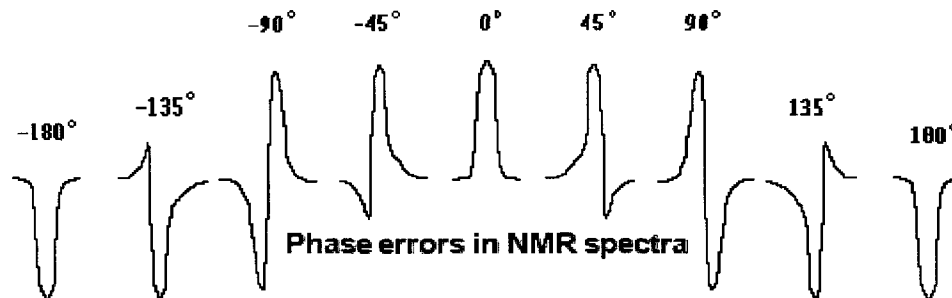


Figure 4.14: Phase errors in NMR spectra [94]

There are fundamental root causes of phase variations in the spectra. Zero and first order are two relatively distinct types of phase correction techniques. The Zero order

error originates due to phase difference between the magnetization vectors and the receiver, this deviation invokes the phase of all resonances to be shifted independent of frequency; the solution is to apply additional constant phase to all spectra in the same manner [95]. Although there are various reasons why the first order phase error occurs, however this frequency dependent error is often unavoidably introduced due to physical delays in the acquisition hardware, electronics noise [87] and spin dynamics related to field inhomogeneity. The first order error can be corrected by introducing additional frequency dependent phase amount that increases linearly with the distance to the reference signal.

There are several approaches to phase correction spectra. The time consuming method of phase correction is the trial and error in which parameters of phase correction are determined diligently to get the desired absorption line shapes. Phase errors are initiated by many sources; thereby it is challenging to come up with a single reliable phase correction algorithm that works at all time on various spectral data. Methods such as maximization or minimization of peak areas [96] and the dispersion versus absorption representation technique that was introduced by Marshall and Roe [97] involves complicated algorithm and is unreliable. Brown et al. proposed a fully automated phase adjustment technique based on baseline optimization [98] and in their paper the authors reported the algorithm occasionally fails during their experiment, and the optimizer that was employed to determine the zero and first order phase values was unreliable. Li Chen and associates [99] proposed an algorithm for automatic phase correction of NMR spectra that is based on entropy minimization. In this method the optimal zero order and first order phase correction estimates are determined by minimization of entropy and the

objective function is designed using Shannon entropy measures, however this algorithm requires chemical shift information to efficiently correct phase errors. The spectrometer that was used in this thesis does not provide chemical shift data and for that reason this method was not implemented. The de Brower method [100] evaluates several approaches including manual phase correction, area minimization, peak height maximization, negative peak minimization and baseline correction. The author concludes none of these techniques were found to be capable of phasing NMR spectra with sufficient robustness and high enough accuracy and the paper suggests one single approach would not lead to acceptable results and combination of proposals are required in line with the process of manual phase correction. The above discussed literature review techniques could not be applied directly to the type of NMR data the spectrometer in our lab collects. Therefore, this thesis's phase correction algorithm will employ the following information to phase correct the spectra.

The complex valued NMR spectra are expressed as  $Z_j = r_j e^{i\phi_j}$  conversely the phase corrected spectra can be formulated as  $\hat{Z}_j = Z_j e^{-i\phi_j}$  where  $Z_j$  is the original spectra. In the  $\hat{Z}_j$  equation  $\phi_j$  indicates the repair angle. In this thesis a phase correction algorithm was developed to correct zero and first order phase errors so that the spectra possess  $0^0$  phase. Beforehand the detected time domain NMR signal is analyzed to determine the zero order phase angle  $\phi_{01}$  and  $\phi_{02}$ . Afterwards the zero order phase correction is applied to all spectra in the same manner using equation 4.10

$$\text{Re}(\hat{Z}_{0j}) = \text{Re}(Z_j) e^{-i\phi_{01}}, \quad \text{Im}(\hat{Z}_{0j}) = \text{Im}(Z_j) e^{-i\phi_{02}} \quad (4.10)$$

The number of data points in each spectrum can be determined from equation 4.11, where  $n$  is the number of data points in a spectrum and  $\Delta f$  being the selected frequency spacing of two adjacent spectra. During multi-frequency selective experiment  $\Delta f$  and the acquisition time was selected to be 4000Hz and 4ms respectively.

$$n = \Delta f * \text{acquisitiontime} \quad (4.11)$$

Based on the parameter setting within the duration of data acquisition time 1024 data points were collected. Equation 4.11 also provides how many data points each spectrum contains. Furthermore, in the multi-frequency composite cosine pulse, the DC component spectrum when  $c(t) = 1$  should be found around the center of the 1024 data points. In order to apply the first order phase correction to the spectra, this thesis's custom made software isolates each spectrum using these above listed information to determine the spectrum angle. Subsequently the frequency dependent phase fixation is applied to each real and imaginary part of the spectra using equation 4.12 to impel the spectra contain  $0^0$  phase.

$$\text{Re}(\widehat{Z}_{1j}) = \text{Re}(\widehat{Z}_{0j})e^{-i\phi_{11j}}, \quad \text{Im}(\widehat{Z}_{1j}) = \text{Im}(\widehat{Z}_{0j})e^{-i\phi_{12j}} \quad (4.12)$$

In this equation  $-\phi_{11j}$  and  $-\phi_{12j}$  denotes the phase correction angle,  $\text{Re}(\widehat{Z}_{1j})$  and  $\text{Im}(\widehat{Z}_{1j})$  are the real and imaginary  $j^{\text{th}}$  data point estimates of the first order phase corrected spectra, whereas  $\text{Re}(\widehat{Z}_{0j})$  and  $\text{Im}(\widehat{Z}_{0j})$  signifies the  $j^{\text{th}}$  values of the real and imaginary parts of the zero order phase corrected spectra.

#### 4.2.4 Experimental results of single frequency excitation

Selection of single excitation frequency occurs when a rectangular pulse envelope is used, in other words  $c(t) = 1$ , and excitation occurs at SPS's NMR center frequency of 4.55MHz. Figure 4.15 shows an echo resulting from rectangular pulse with 1024  $\mu\text{s}$  duration. This margarine sample echo is the result of ensemble averaging of spin echoes in a CPMG train. The experimental parameters were echo time = 4ms, acquisition time = 1ms, recycling delay = 0.2s, attenuation = 42db, NMR frequency = 4.55MHz, acquired data points = 1024, number of echoes = 32, and number of scans = 256.

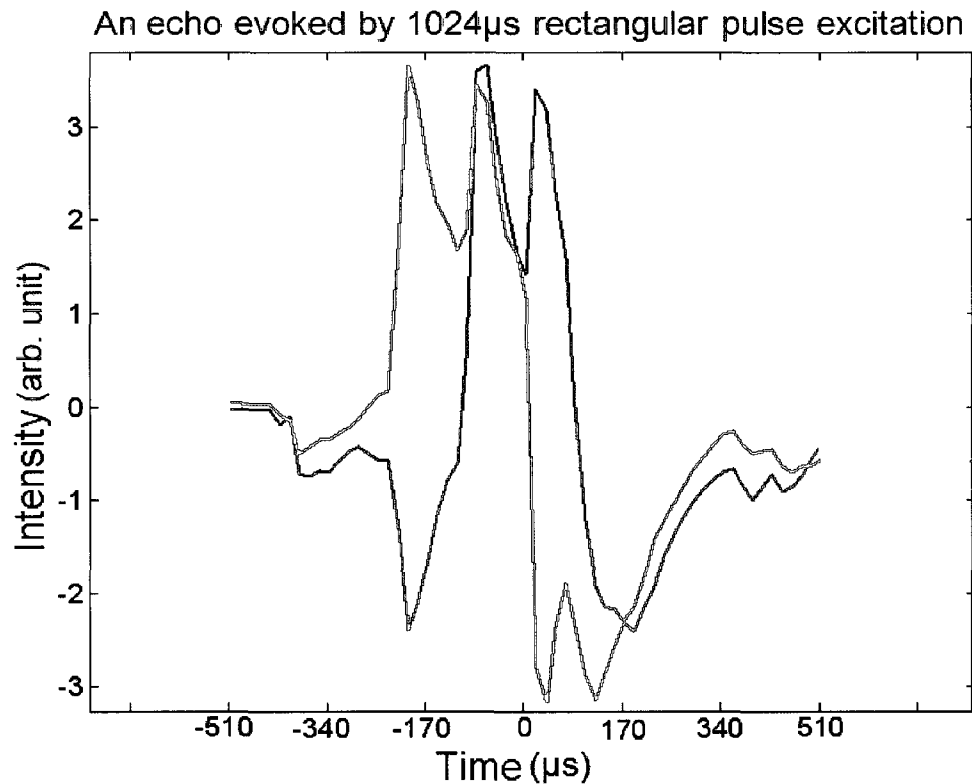


Figure 4.15: An echo evoked by single frequency rectangular RF pulse excitation

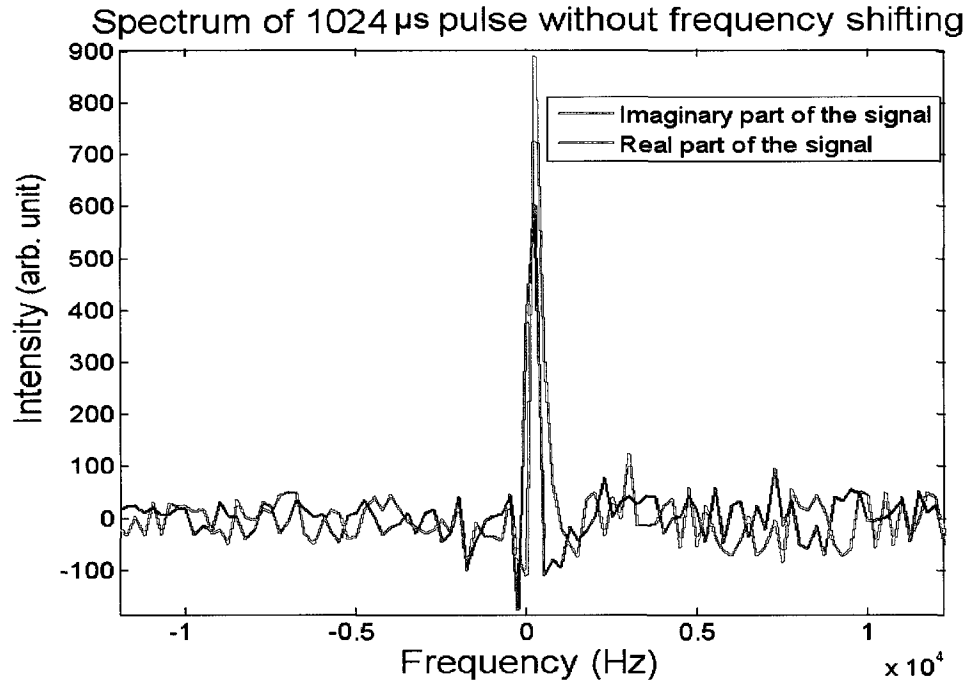


Figure 4.16: The spectrum of single frequency excitation

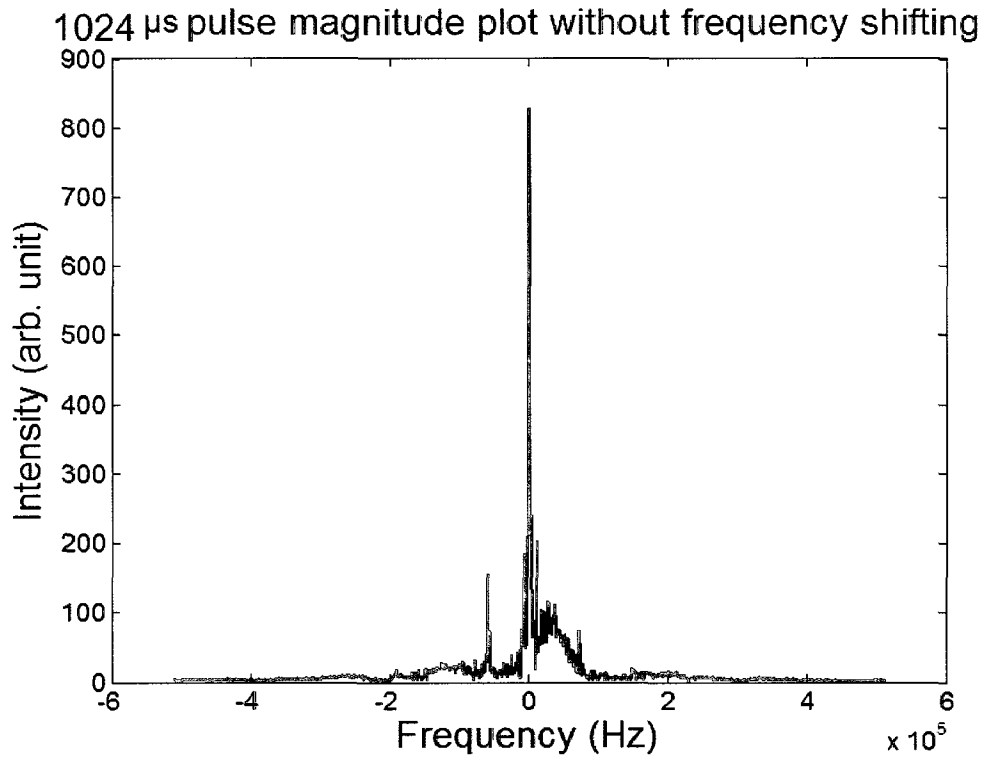


Figure 4.17: Single frequency excitation magnitude plot

Figure 4.16 is the spectrum of single frequency excitation, whereas figure 4.17 exhibits the magnitude plot of single frequency excitation, the result of this plot will be used at the end of this chapter to compare the SNR of single frequency with multi-frequency excitation. In single frequency experiments decreasing the excitation band tend to produce low SNR signal. Solution is to excite many narrow bandwidth spectra, each with a distinct center frequency, simultaneously, and the spectra are then co-added to find the maximum signal intensity; this is discussed in details the following section.

#### **4.2.5 Experimental results of multi-frequency selective excitation**

The multi-frequency shifted pulses can be combined with existing methods of selective excitation so as to produce single or multiple frequency selective pulses [101]. This section presents the experimental results of multi-frequency composite cosine pulse sequence. In order to analyze the relationship between frequency shift increase and SNR of the observed signals, the experiments were performed for several frequency shifts using margarine sample, 1024 $\mu$ s composite cosine RF pulse and 4000Hz separation between two neighboring spectra picks. Frequency spacing is selected so that two adjacent spectra do not overlap and are easily distinguishable. In this experiment the spacing that was chosen is about four times that of the RF pulse length employed. The scanner's sensitive region is confined within  $\pm 100$  kHz frequency strip; therefore the maximum number of spectra that will be excited is limited by this relatively homogeneous region. Hence, depending on the number of frequency shifts, excitations could occur at  $4.55\text{MHz} \pm n \cdot 4000\text{Hz}$ , where the multiplier  $n = 0, 1, 2, 3 \dots M$ . However, equation 4.9 implies the existence of pulse amplitude scaling. In ExpSpel programming

environment, the code below generates multi-frequency composite carrier signal and the cosine term in this code causes amplitude scaling.

```
count = 0 ;
while (count < steps)
    c2 = 4;
    x = count*step*0.000001;
    y[count] = 0;
    while (c2 < 128)
        y[count] = y[count] + 1/32*cos(2*PI*c2*1000*x);
        c2 = c2+4;
    endwhile
    count = count + 1;
endwhile
y[count] = SHAPE_END;
```

Figure 4.18 shows the pulse envelope  $c(t)$  for the excitation. The single-frequency sinusoid present is responsible for a single shifted pair of frequencies, and the DC component also excited a peak at zero frequency offset. Figure 4.19 presents the experimentally observed time domain signal when the frequency shift multiplier  $n = 0, 1$ .

The figure 4.21 indicates spectra are observed at 4.55 MHz as well as 4.55MHz  $\pm 4000$  Hz. The experimental parameters were echo time = 8ms, acquisition time = 2ms, recycling delay = 0.5s, NMR frequency = 4.55MHz, acquired data points = 1024, number of echoes = 32, and number of scans = 256. The  $90^\circ$ , and  $180^\circ$  attenuation equals 36db and 30db respectively. The central peak is approximately twice the amplitude of the satellite peaks, due to factor of  $\frac{1}{2}$  in equation 7.10. Figure 4.20 shows the echo spectrum wherein the central and shifted peaks are clearly visible. The phase problem is readily apparent in this plot. Although the peaks have similar character, their phase differs, and co-adding the spectra would result in cancellation. The zero and first order phase correction procedure is applied to figure 4.20 to generate phase corrected spectra of figure 4.21. It can now be seen that the peaks are in phase, and identical, aside from

amplitude changes. The peaks are subsequently ensemble averaged, resulting in the single peak show in figure 4.22.

### Composite cosine RF pulse envelope: 3-frequency excitation

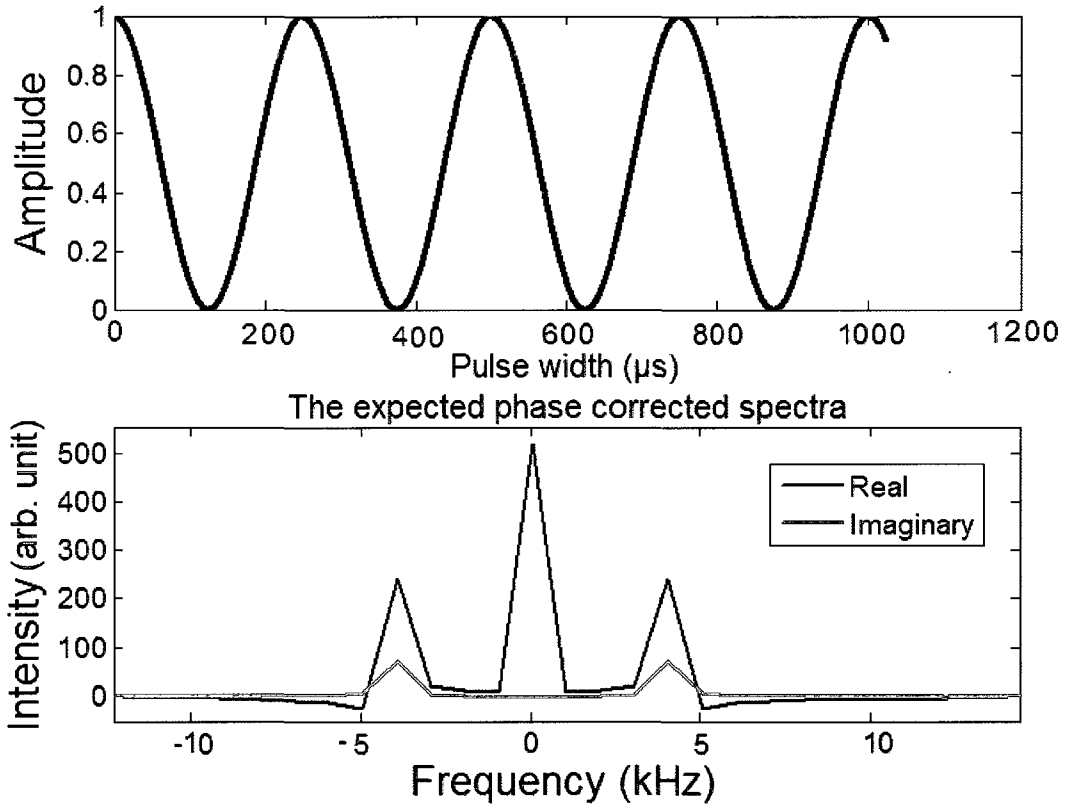


Figure 4.18: Simulation result: The 3-frequency excitation

First plot represents the 1024 $\mu\text{s}$  composite (two carrier cosine signals are added) RF pulse envelope. The second figure exhibits excitation at three frequencies, it shows the phase corrected spectra having a DC component at 0 as well as spectra centered at  $\pm 4000\text{Hz}$ .

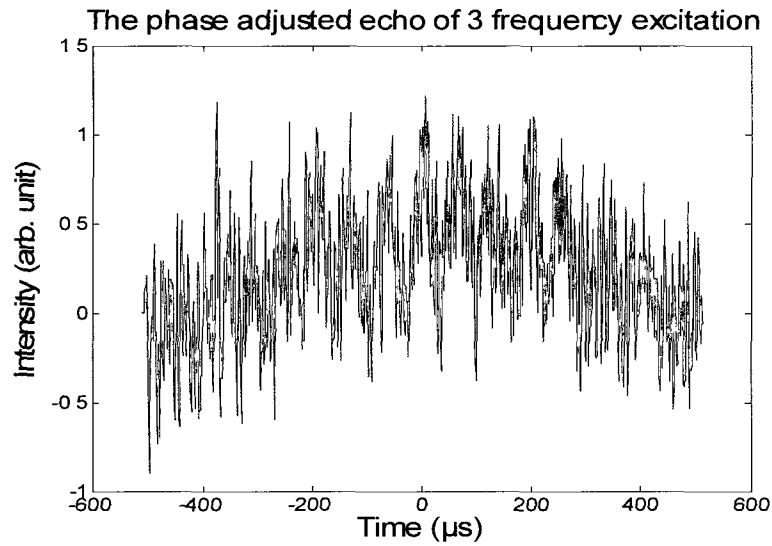


Figure 4.19: Experimental result: The 3-frequency phase adjusted echo.

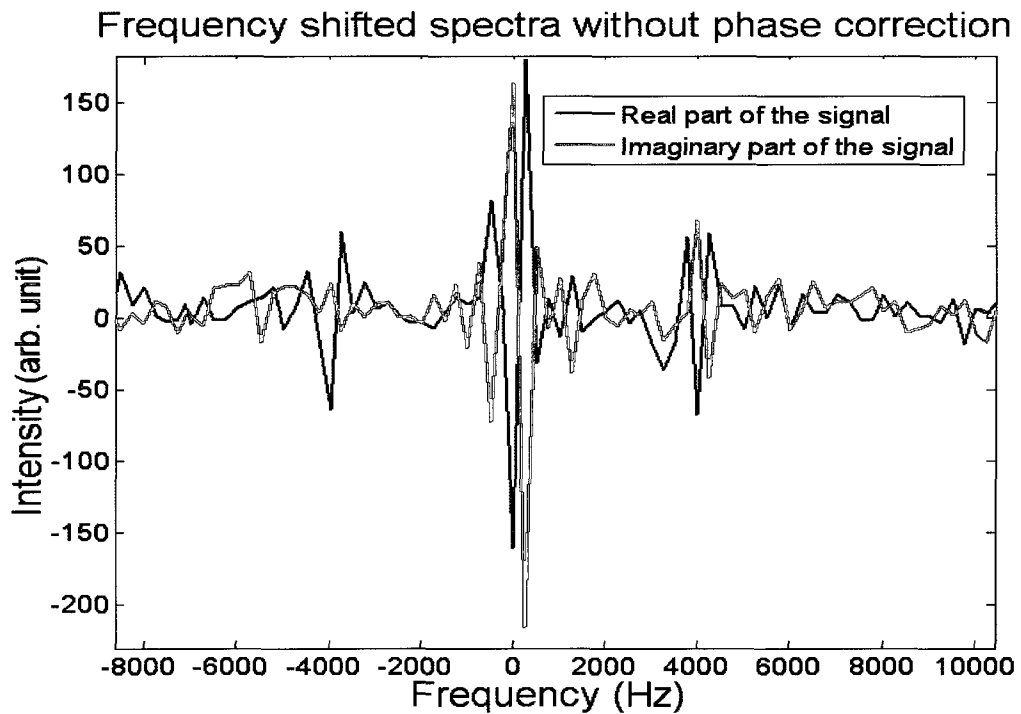


Figure 4.20: Experimental result: The 3-frequency not phase corrected spectra. Spectra here are seen to be out of phase due to phase error, however excitation is shown to occur at 0 as well as  $\pm 4000$ Hz.

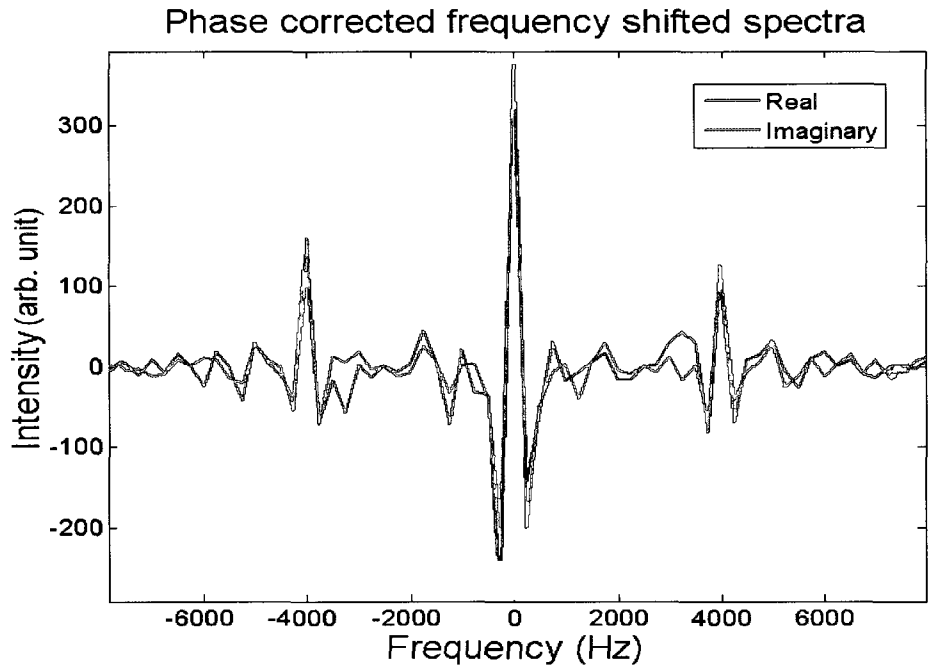


Figure 4.21: Experimental result: The 3-frequency phase corrected spectra. Spectra have  $0^0$  phase and excitation is shown to occur at 0 as well as  $\pm 4000$ Hz.

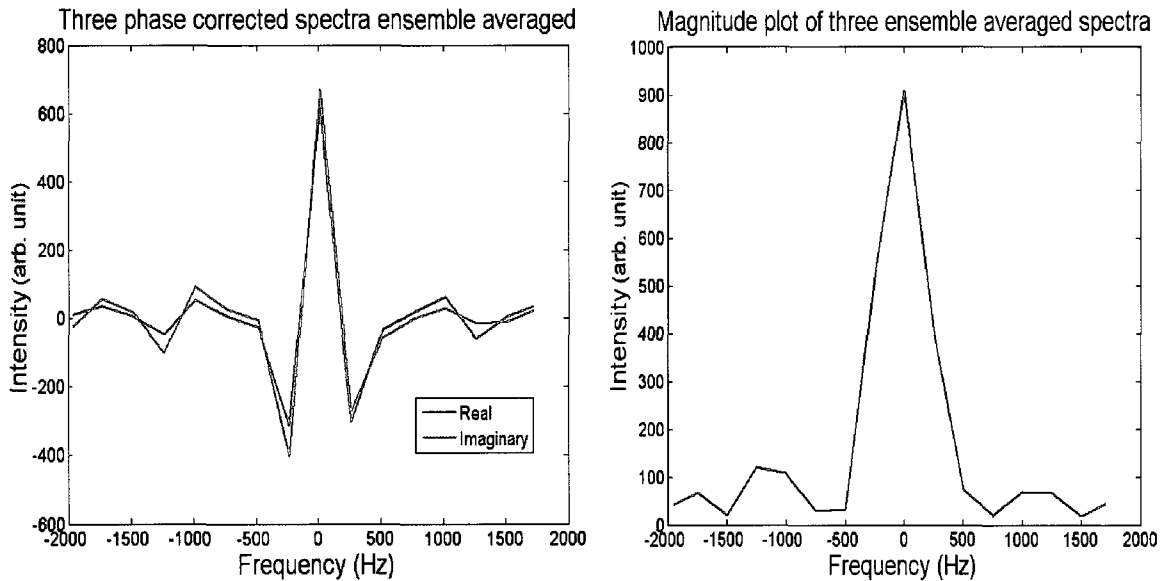


Figure 4.22: Experimental result: Three spectra co-added Single spectrum and magnitude plot representation of 3-frequency excitation.

For the case of the frequency shift multiplier  $n = 0, 1, 2, 3$ , the pulse envelope and simulated spectra are plotted in figure 4.23, whereas the actual experimentally obtained spectra are shown in figure 4.25. In this case, six satellite peaks are present. The figure 4.24 shows the echo obtained using this pulse shape. The experimental parameters in this study were the same as in the previous case except the  $90^\circ$ , and  $180^\circ$  attenuation equals 30db and 24db respectively. The figure 4.26 shows the phase corrected spectra, whereas figure 4.27 exhibits the result of spectral ensemble averaging. Figure 4.26 reveals spectra are observed at  $4.55\text{MHz} \pm n*4000\text{Hz}$ , where  $n = 0, 1, 2, 3$ .

Noteworthy, the simulation spectral outcome slightly differs from that of the experimental result; the variation in amplitude observed in the peaks results from variations in spatial sensitivity of the RF coil used in the measurements,

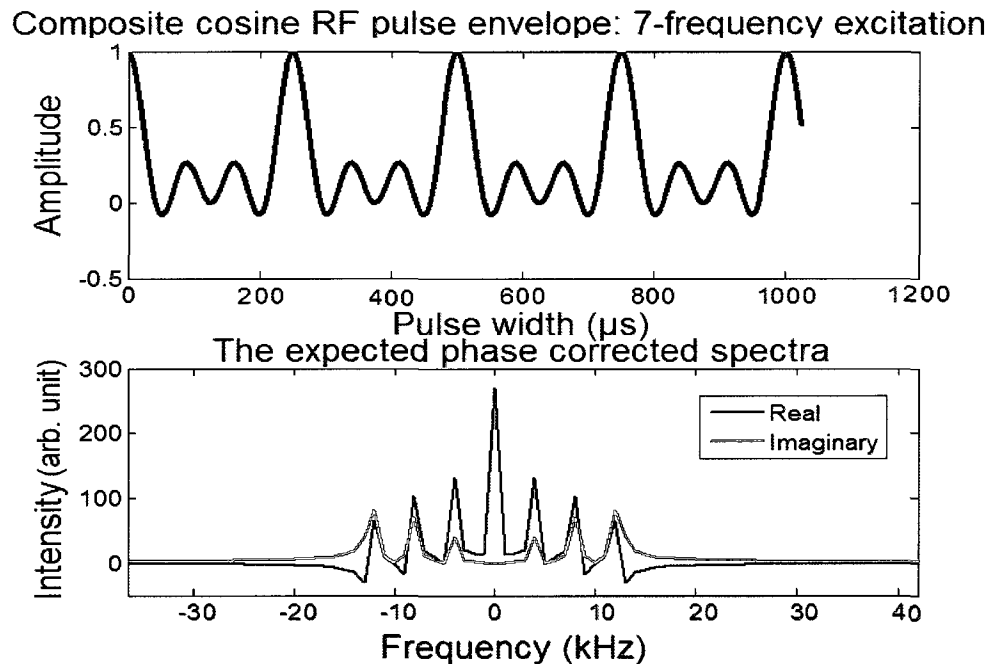


Figure 4.23: Simulation result: The 7-frequency excitation  
 First plot represents the  $1024\mu\text{s}$  composite (four carrier cosine signals are added) RF pulse envelope. The second figure exhibits excitation at seven frequencies, it shows the phase corrected spectra are centered at  $\pm n4000\text{Hz}$ , where  $n = 0, 1, 2, \text{ and } 3$ .

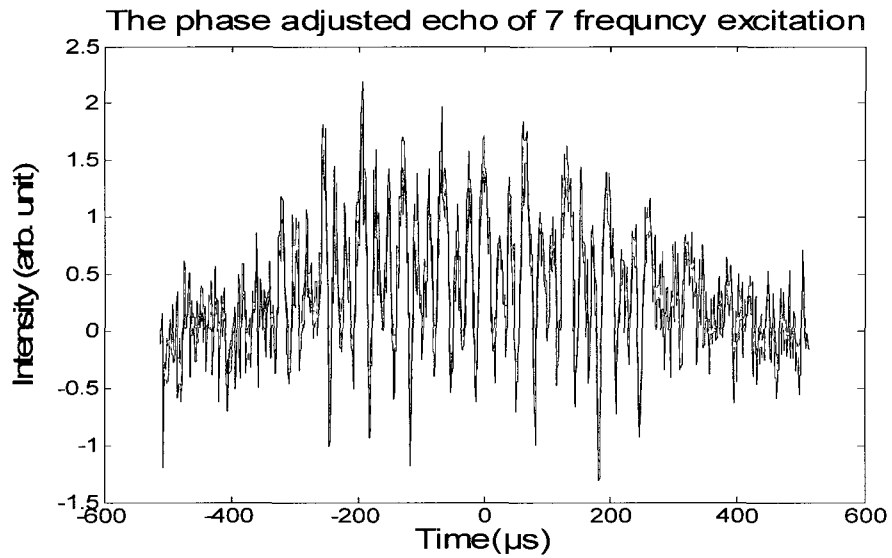


Figure 4.24: Experimental result: The 7-frequency phase adjusted echo.

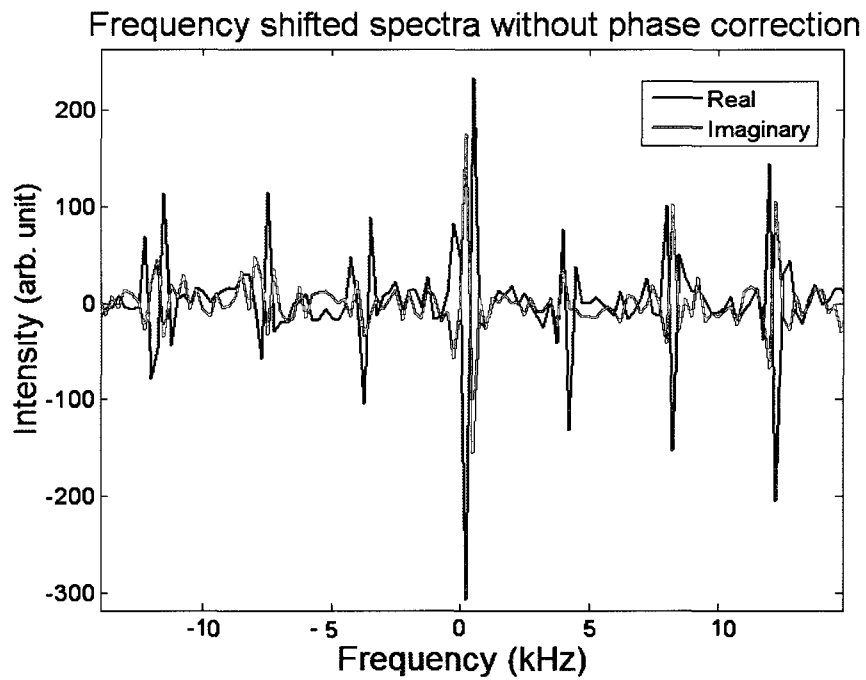


Figure 4.25: Experimental result: The 7-frequency not phase corrected spectra. Spectra are out of phase because of phase error, as we can see here excitation occurred at  $\pm n4000\text{Hz}$ , where  $n = 0, 1, 2,$  and  $3$ .

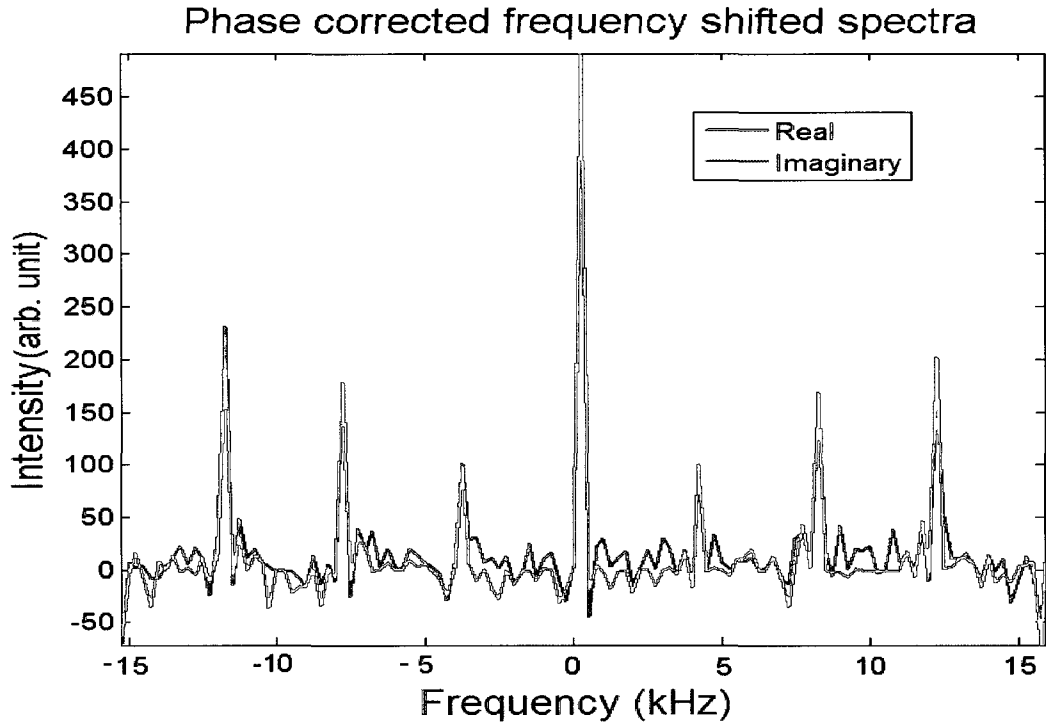


Figure 4.26: Experimental result: The 7-frequency phase corrected spectra. Spectra have  $0^0$  phase and excitations are centered at  $\pm n4000\text{Hz}$ , where  $n = 0, 1, 2, 3$ .

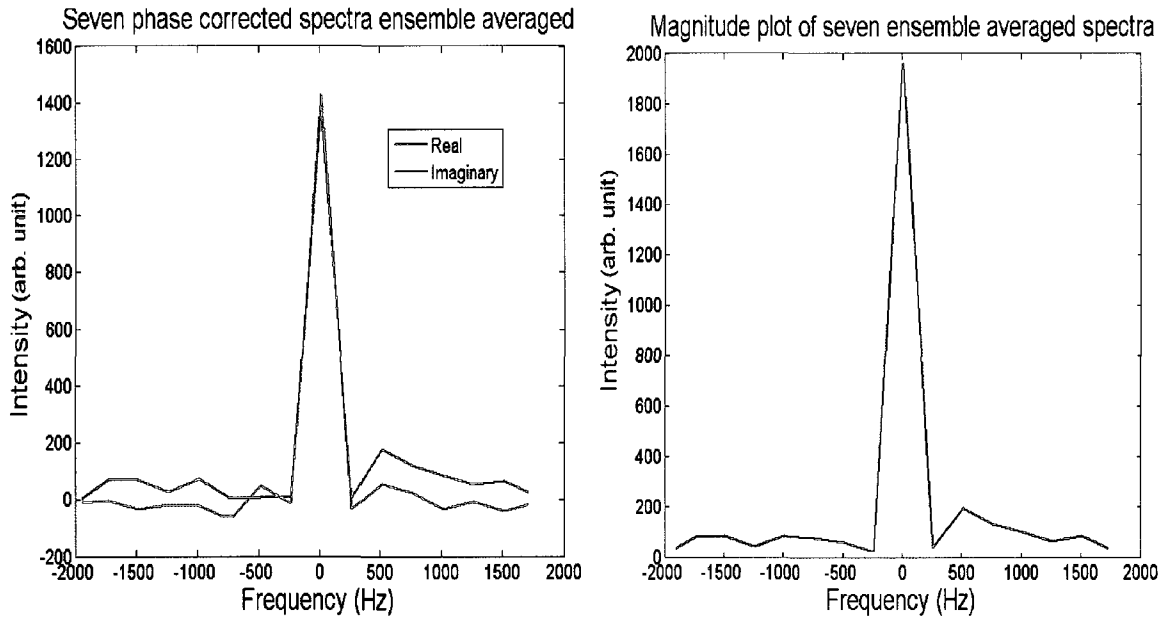


Figure 4.27: Experimental result: Seven spectra co-added  
Single spectrum and magnitude plot representation of 7-frequency excitation.

The procedure was repeated for seven sinusoids superimposed in the pulse shape and the results can be seen in figures 4.28-4.32. Again the experimental parameters in this case were the same as the initial multi-frequency experiment except the  $90^0$ , and  $180^0$  attenuation are set to equal 24db and 18db respectively. Figure 4.29 shows the time domain signals. The phase corrected spectra in figure 4.31 demonstrates spectra are observed at  $4.55\text{MHz} \pm n \cdot 4000\text{Hz}$ , where  $n = 0, 1, 2 \dots 7$ .

### Composite cosine RF pulse envelope: 15-frequency excitation

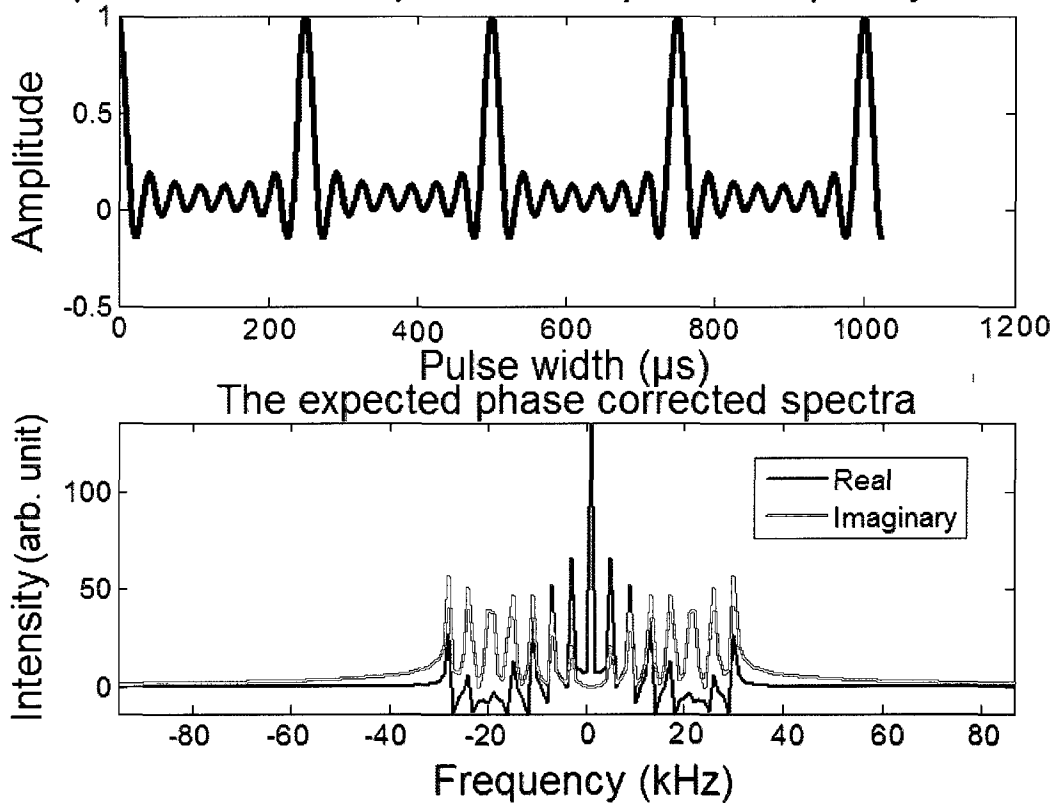


Figure 4.28: Simulation result: The 15-frequency excitation  
 First plot represents the  $1024\mu\text{s}$  composite (eight carrier cosine signals are added) RF pulse envelope. The second figure exhibits excitation at fifteen frequencies, it shows the phase corrected spectra are centered at  $\pm n \cdot 4000\text{Hz}$ , where  $n = 0, 1, 2 \dots 7$ .

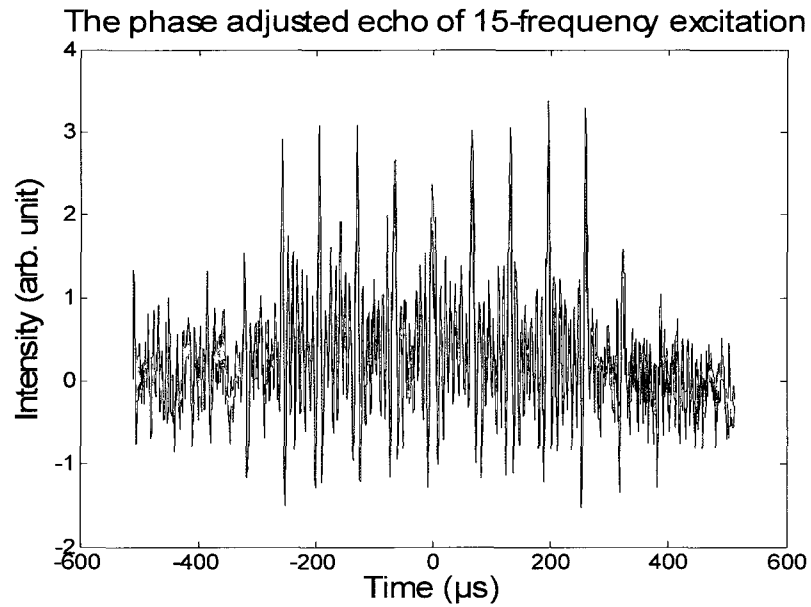


Figure 4.29: Experimental result: The 15-frequency phase adjusted echo.

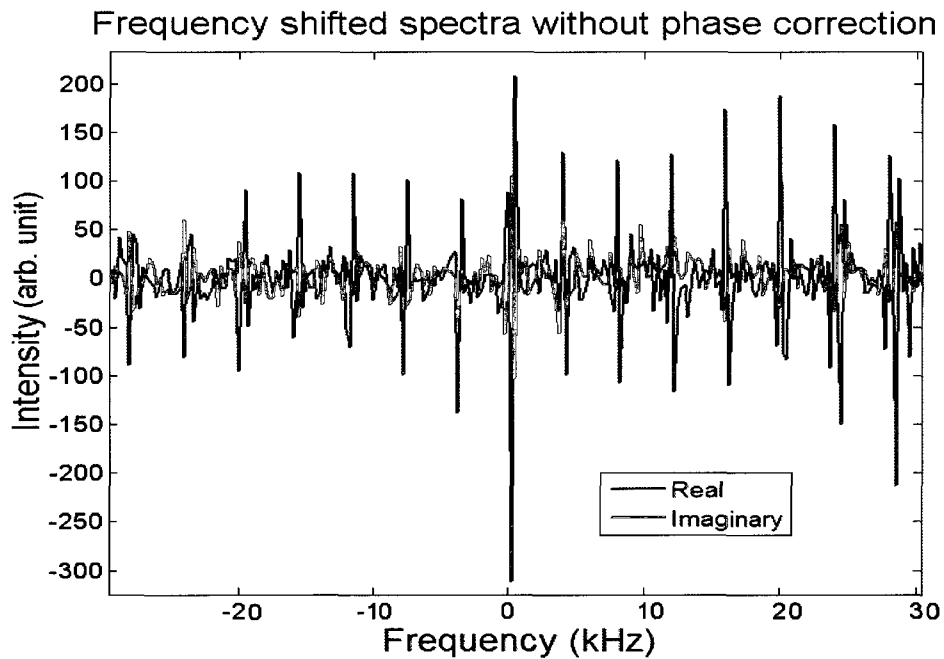


Figure 4.30: Experimental result: The 15-frequency not phase corrected spectra. Even though spectra are out of phase, however we can see clearly excitation occurred at  $\pm n4000\text{Hz}$ , where  $n = 0, 1, 2, \dots, 7$ .

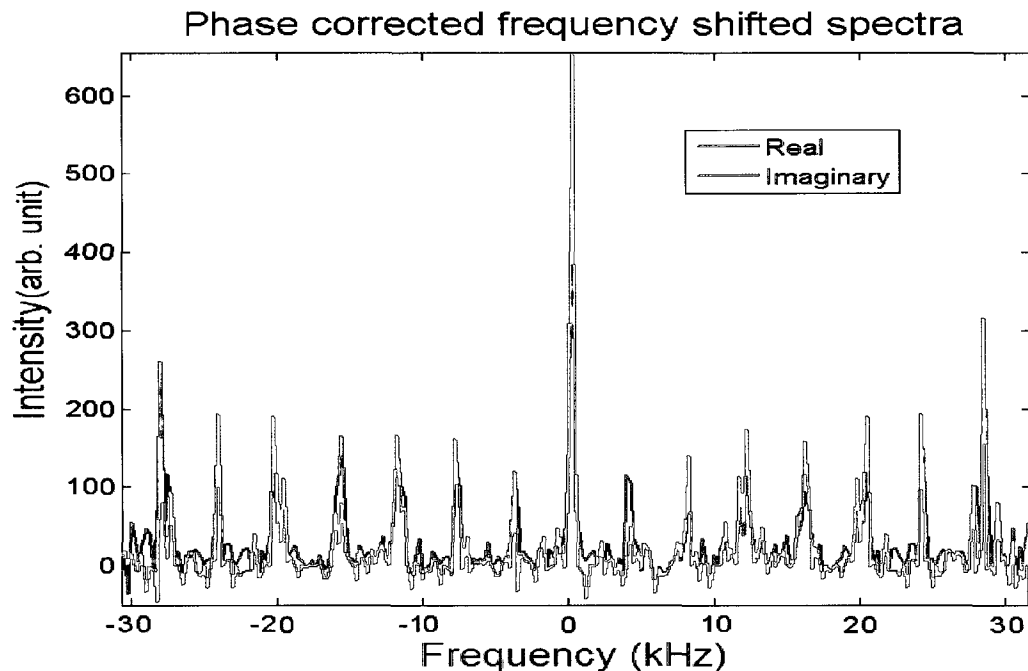


Figure 4.31: Experimental result: The 15-frequency phase corrected spectra. After phase correction, spectra here is shown to having  $0^0$  phase and the NMR excitations are centered at  $\pm n4000\text{Hz}$ , where  $n = 0, 1, 2 \dots 7$ .

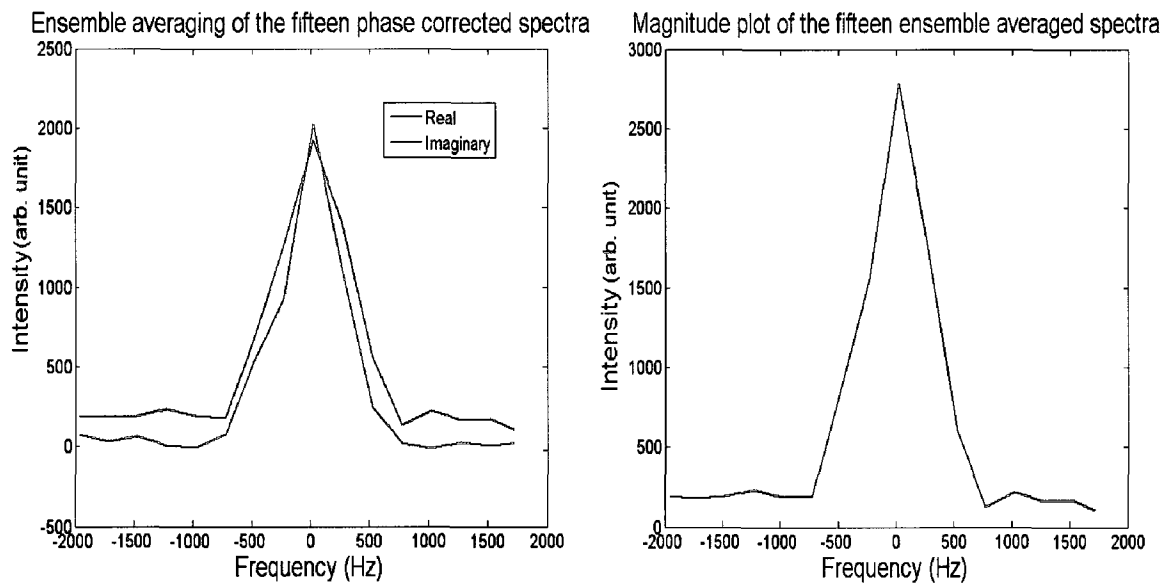


Figure 4.32: Experimental result: The fifteen spectra co-added Single spectrum and magnitude plot representation of 15-frequency excitation.

To examine the effect of frequency increase in SNR, the experiment was repeated for 31-frequencies and the results are exhibited in figures 4.32-4.37. The experimental parameters were left the same as in the previous experiments except the  $90^0$ , and  $180^0$  attenuation equals 18db and 12db respectively. The figures 4.34 presents the time domain signal, on the other hand the phase corrected spectra in figure 4.36 manifests spectra are detected at  $4.55\text{MHz} \pm n*4000\text{Hz}$ , where  $n = 0, 1, 2 \dots 15$ .

### Composite cosine RF pulse envelope: 31-frequency excitation

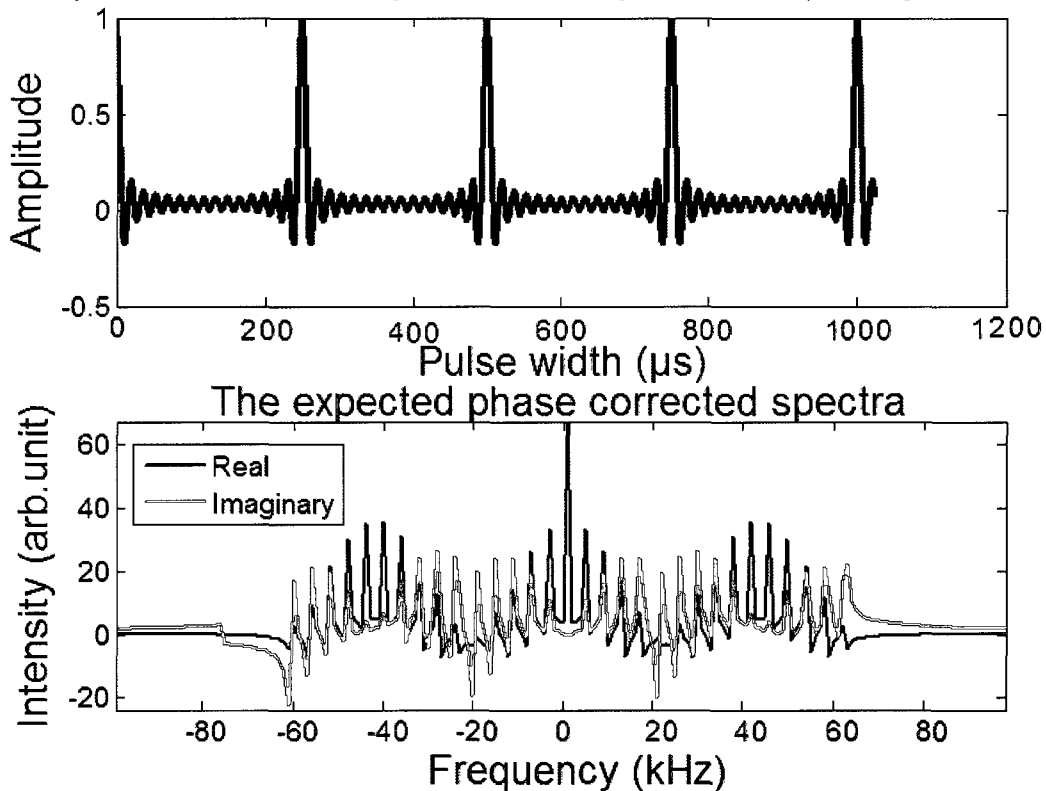


Figure 4.33: Simulation result: The 31-frequency excitation

First plot represents the  $1024\mu\text{s}$  composite (sixteen carrier cosine signals are added) RF pulse envelope. The second figure exhibits RF excitation at thirty-one frequencies, it shows the phase corrected spectra are centered at  $\pm n4000\text{Hz}$ , where  $n = 0, 1, 2 \dots 15$ .

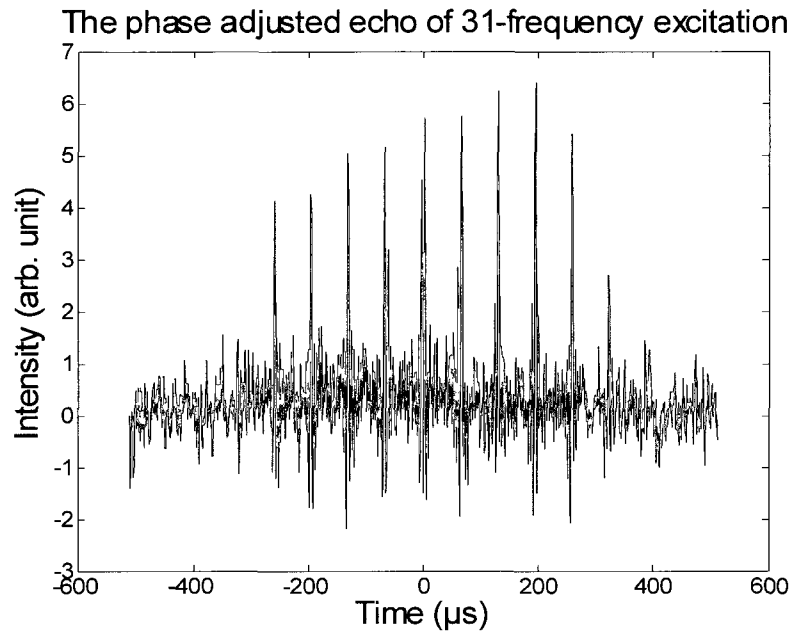


Figure 4.34: Experimental result: The 31-frequency phase adjusted echo.

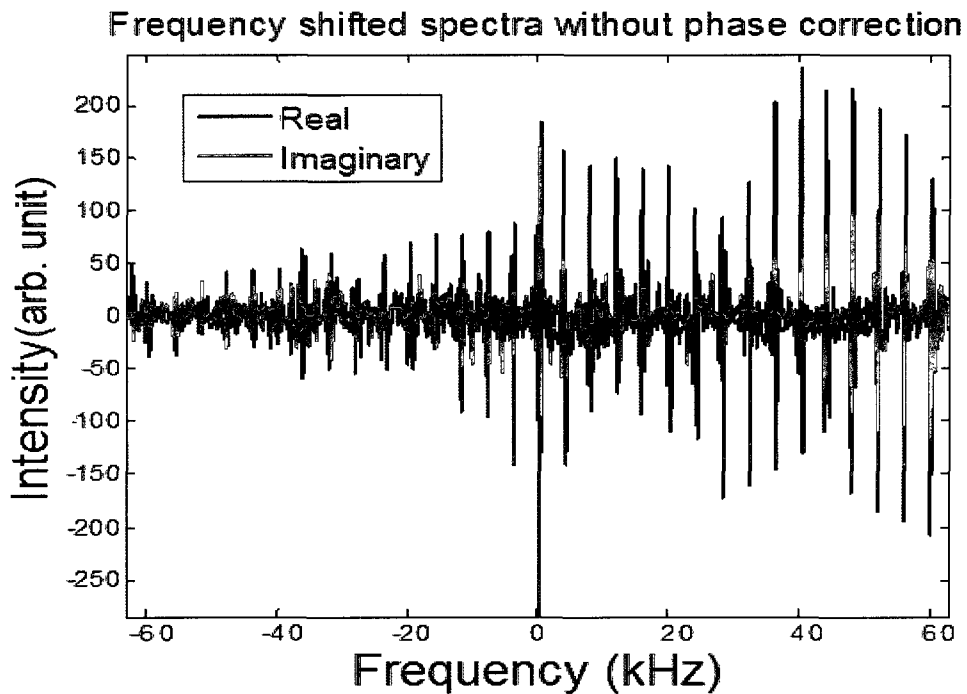


Figure 4.35: Experimental result: The 31-frequency not phase corrected spectra. Due to zero and first order error, spectra are out of phase, however excitation is shown to occur at frequency of  $\pm n4000\text{Hz}$ , where  $n = 0, 1, 2 \dots 15$ .

### Phase corrected frequency shifted spectra

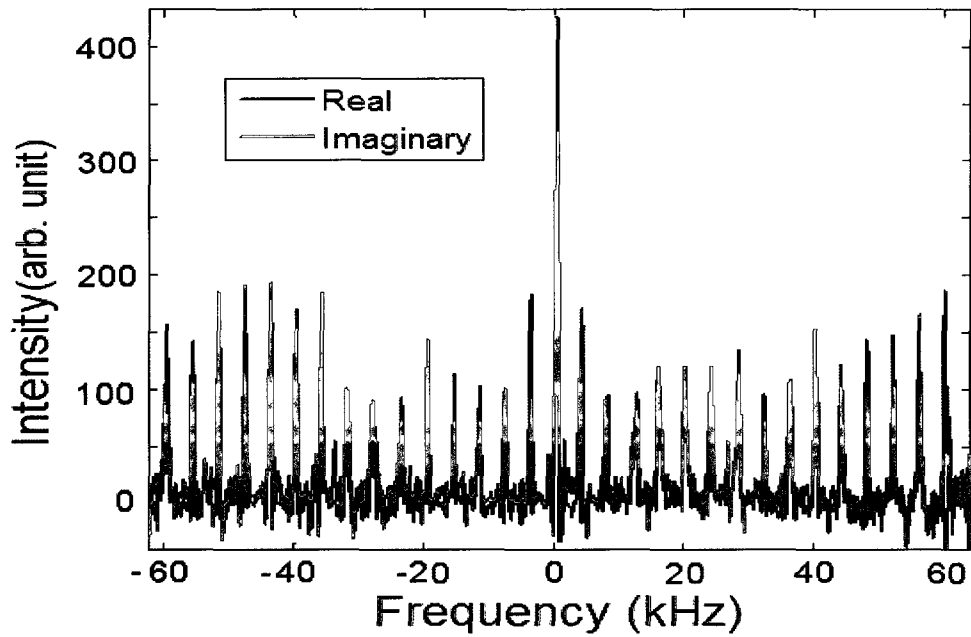


Figure 4.36: Experimental result: The 31-frequency phase corrected spectra. Spectra possess  $0^0$  phase and excitation occurred at  $\pm n4000\text{Hz}$ , where  $n = 0, 1, 2 \dots 15$ .

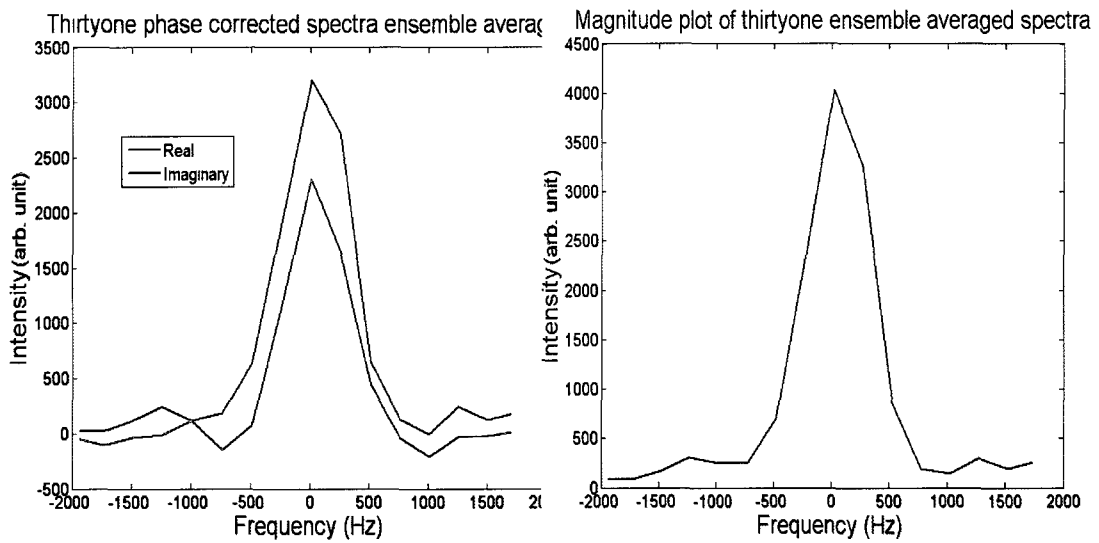


Figure 4.37: Experimental result: Thirty-one spectra co-added. Single spectrum and magnitude plot representation of 31-frequency excitation.

Figures 4.38-4.43 are the results of 63-frequency excitation, in this experiment most of the parameters setting stayed the same as in the earlier experiments, however the  $90^0$ , and  $180^0$  attenuation values were chosen to be 12db and 6db respectively. The figure 4.39 displays the observed time domain signal when sixty three NMR frequencies were excited. Figure 4.40 introduces spin echoes recorded from a CPMG measurement of margarine sample. The figure 4.42 discloses spectra are detected at  $4.55\text{MHz} \pm n \cdot 4000\text{Hz}$ , where  $n = 0, 1, 2, \dots, 31$ . Even though the 63-frequencies were excited within the 248 kHz bandwidth, after co-adding the spectra the final spectrum only had a narrow frequency band of that is approximately 1500Hz while preserving spectral shape.

### Composite cosine RF pulse envelope: 63-frequency excitation

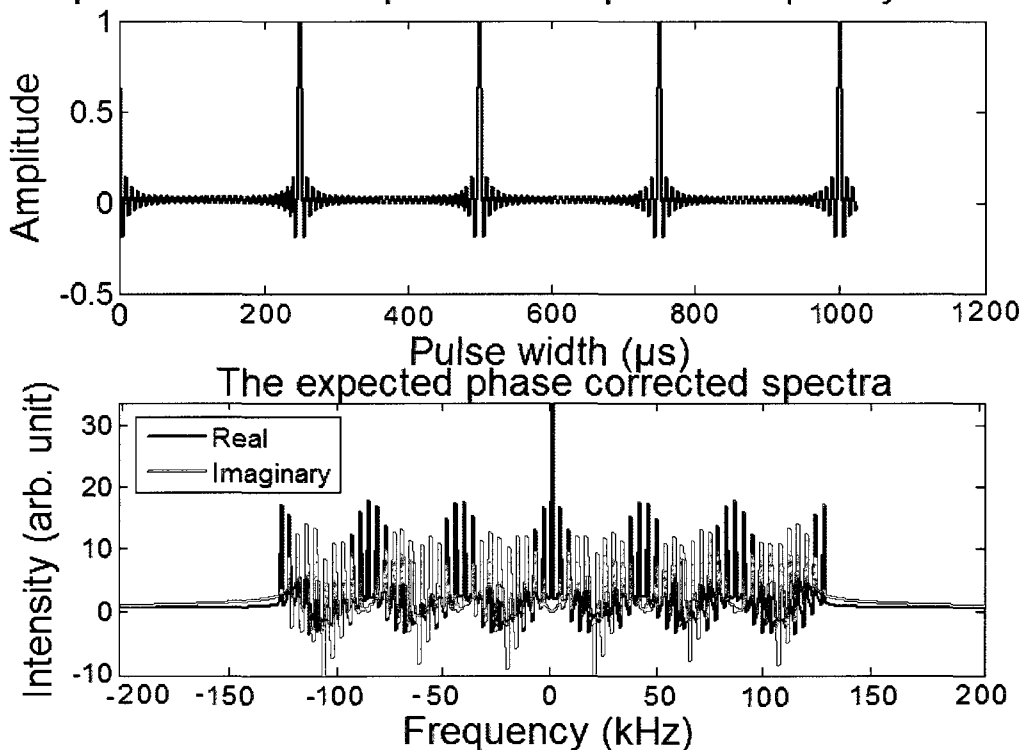


Figure 4.38: Simulation result: The 63-frequency excitation

First plot represents the  $1024\mu\text{s}$  composite (thirty-two carrier cosine signals are added) RF pulse envelope. The second figure exhibits RF excitation at sixty-three frequencies, it shows the phase corrected spectra are centered at  $\pm n \cdot 4000\text{Hz}$ , where  $n = 0, 1, 2, \dots, 31$ .

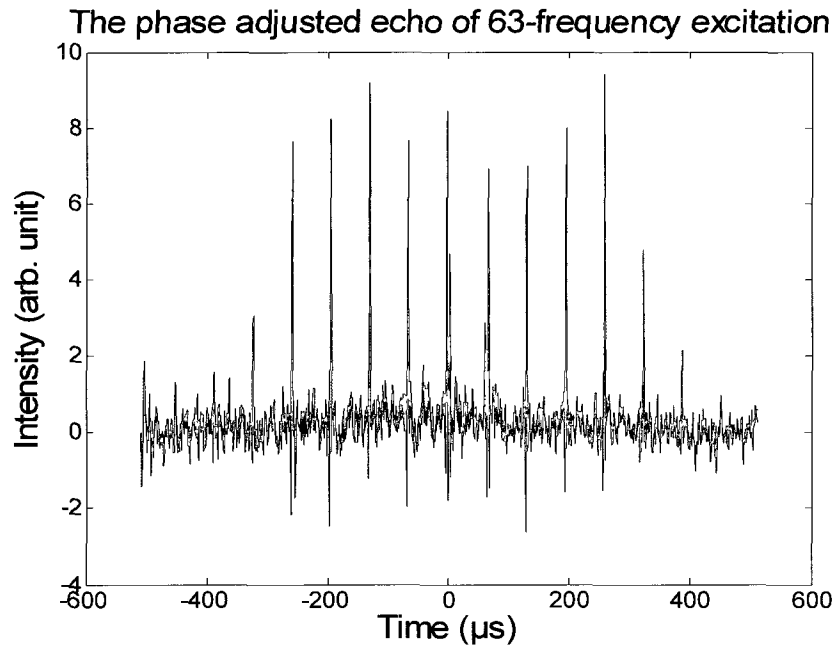


Figure 4.39: Experimental result: The 63-frequency phase adjusted echo.

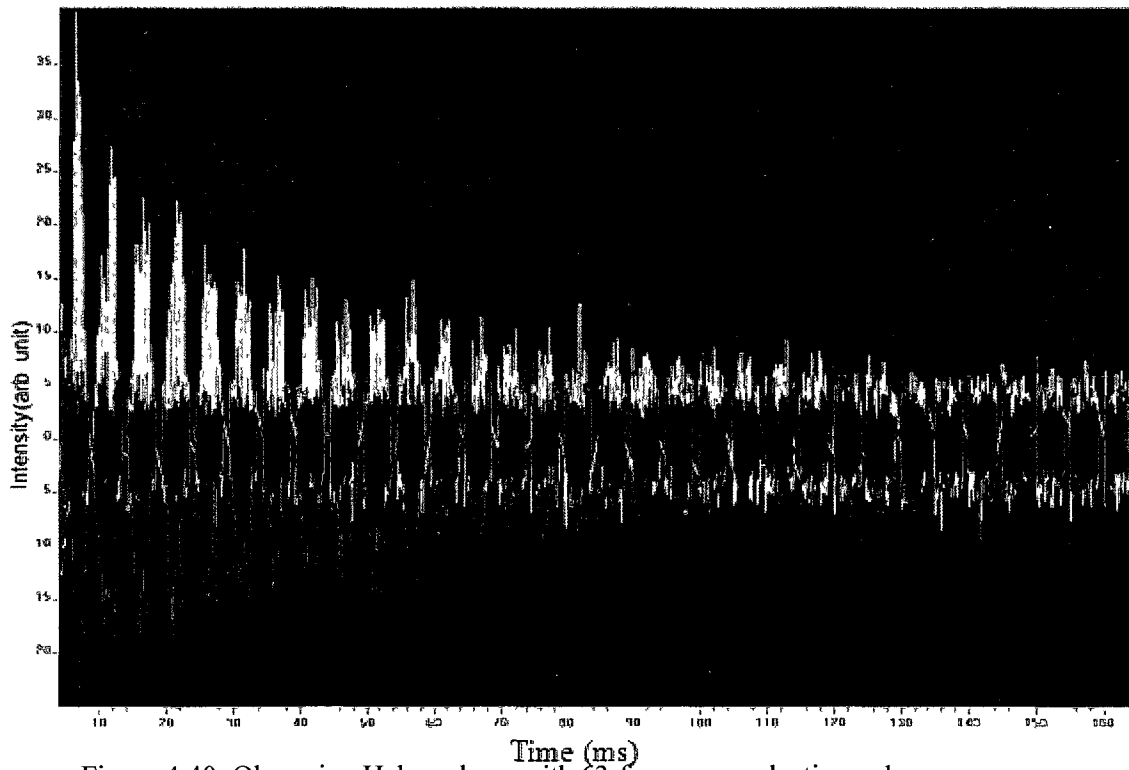


Figure 4.40: Observing Hahn echoes with 63-frequency selective pulse sequence.

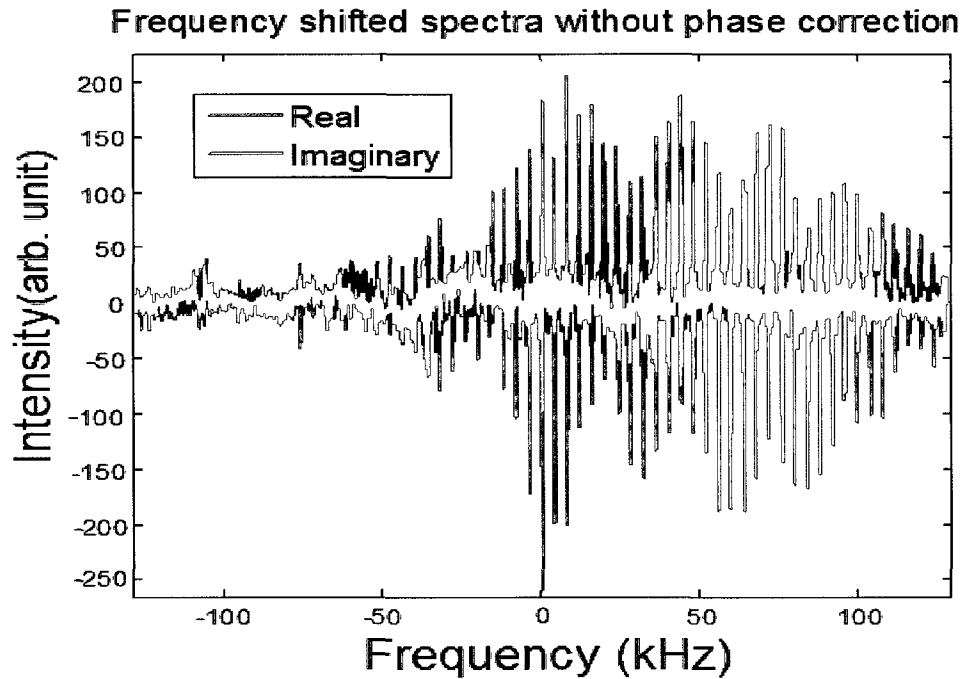


Figure 4.41: Experimental result: The 63-frequency not phase corrected spectra. Although spectra are out of phase, as we can see, excitation occurred at  $\pm n4000\text{Hz}$ , where  $n = 0, 1, 2 \dots 31$ .

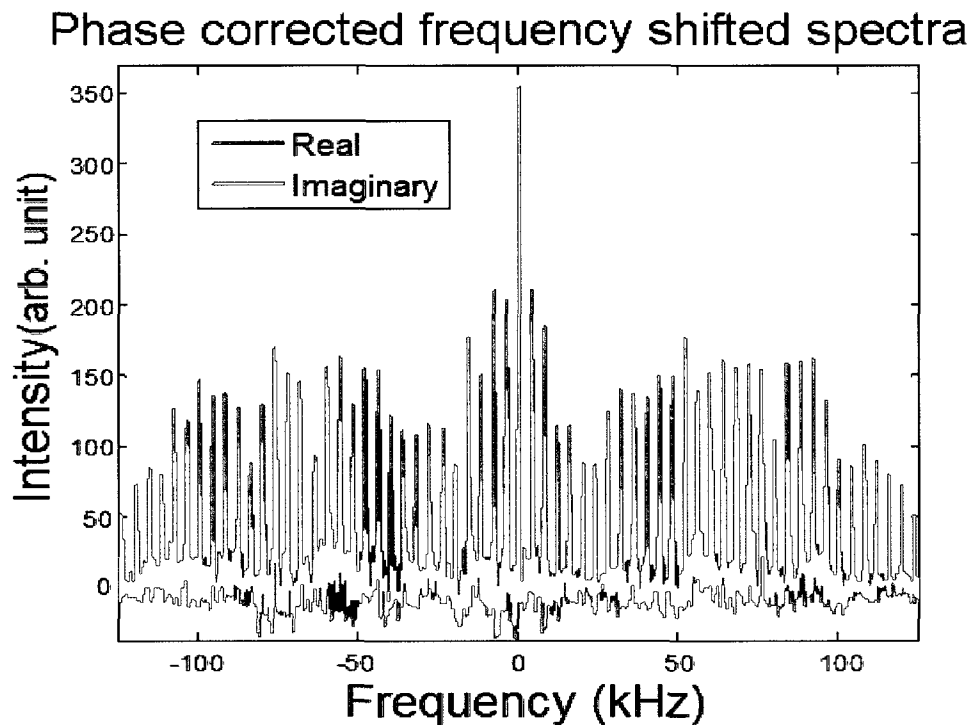


Figure 4.42: Experimental result: The 63-frequency phase corrected spectra. These phase corrected spectra are centered at  $\pm n4000\text{Hz}$ , where  $n = 0, 1, 2 \dots 31$ .

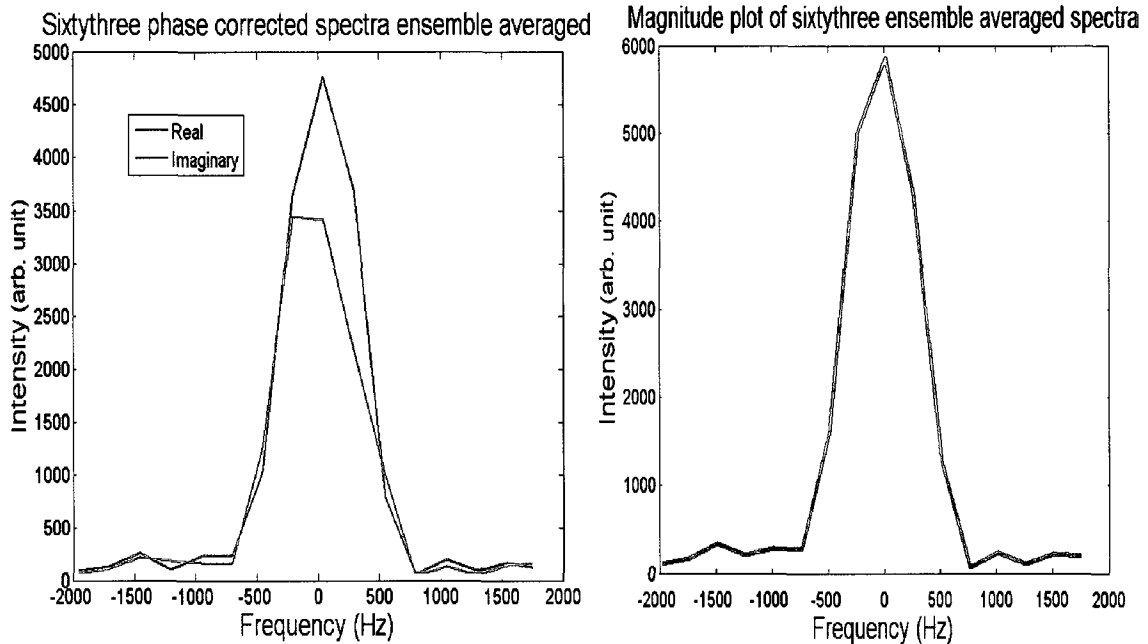


Figure 4.43: Experimental result: The sixty-three spectra co-added  
Single spectrum and magnitude plot representation of 63-frequency excitation

The tables 4.1 and 4.2 contain single and multi-frequency maximum signal intensity data respectively. Besides results from table 4.2 indicates multi-frequency method performed better than the single frequency counterpart. The multi-frequency data signifies the value of maximum signal strength intensified as the number of frequency excitation increased. The figure 4.44 exhibits, the increase in signal intensity is roughly linear with the number of spectra added. Assuming each spectrum is corrupted with additive Gaussian white noise, this would indicate that the SNR of the measurement increases with the square root of the number of spectra, as discussed in Chapter 2. In conclusion multi-frequency selective excitation improved the SNR of the detected signals quite dramatically. The multi-frequency pulse sequence that was developed for this thesis can be employed to acquire high SNR MR measurement.

Excitation by rectangular shaped RF pulse	
Number of frequencies excited	Maximum signal intensity
1	830.20

Table 4.1: Single frequency excitation: Maximum signal intensity data

Excitation by composite cosine shaped RF pulse	
Number of frequencies excited	Maximum signal intensity
3	906.30
7	1985.01
15	2783.10
31	4049.02
63	5869.07

Table 4.2: Multi-frequency excitation: Maximum signal intensities data

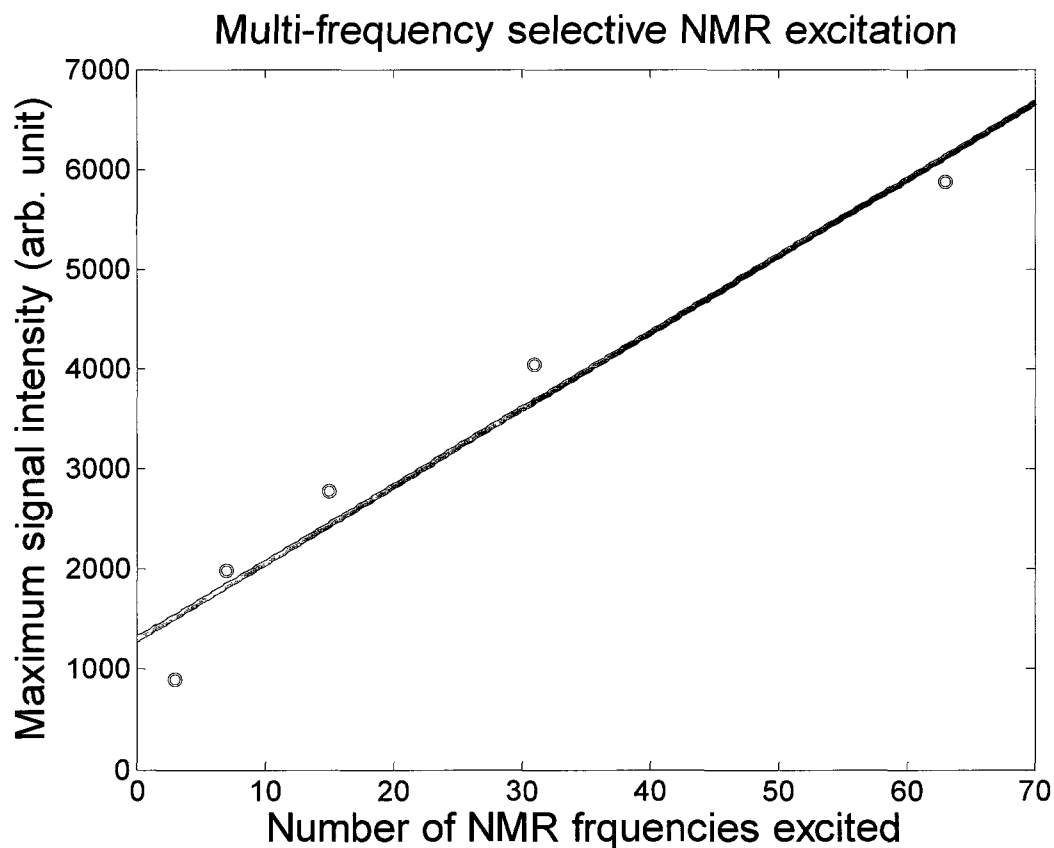


Figure 4.44: Maximum signal intensity versus number of frequencies excited

#### **4.2.6 Measuring diffusion with multi-frequency selective pulse**

The effect of magnetic field inhomogeneity on NMR spectra is a broadening of spectral lines. In theory, increasing the excitation period is necessary to improve resolution, however due to field variations and the presence of gradients during the excitation process, the nuclei that are observed displaces over the experimental time scale. An example of a phenomenon which cannot be observed in a usual echo experiment is liquid self diffusion. The slow random molecular motion of a liquid will cause spins excited at one frequency to be detected at another, and will cause spectral broadening. However, this process occurs on a timescale of milliseconds or longer, and cannot be observed in the short echoes recorded by traditional experimental techniques.

Spectra broadening due to random motion of particles have been examined by increasing the width of the composite cosine RF pulse. The multi-frequency composite pulse sequence along with mineral oil sample has been employed to investigate this spectral broadening. The experiment was performed for various pulse widths and the co-added spectra magnitude plots are put together to exhibit diffusion phenomenon as shown in figure 4.45. In this experiment sixty three NMR frequencies were excited. Most of the experimental parameters were left the same as in the 63-frequency excitation study, except were echo time = 12ms, acquisition time = 4ms, recycling delay = 0.8s. A 4 kHz frequency spacing value was employed in all of the three pulse length diffusion measurements.

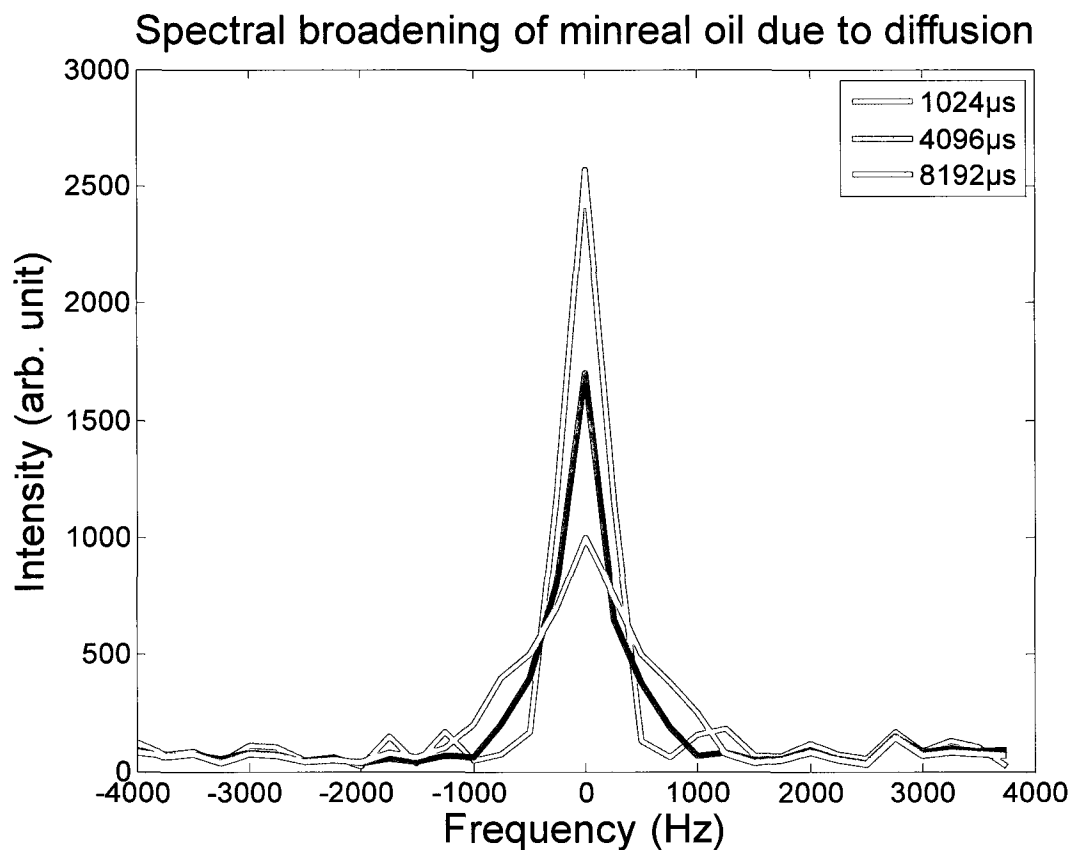


Figure 4.45: Spectral broadening due to diffusion.  
Observing molecular mobility in mineral oil sample when 8192 $\mu$ s RF pulse is applied

We have demonstrated spectral broadening NMR diffusometry technique by exciting several narrow frequency bands. This proposed technique is beneficial to analyze molecular mobility of liquid samples.

In the section 3.6 diffusion study, in order to fit the diffusion curve several NMR measurements were needed for various  $\tau$ , however this section's spectral broadening method have a significant advantage, since it only requires few simple NMR measurements to study diffusion in a sample.

## **Chapter 5.0 Conclusions and future work**

### **5.1 Conclusions**

Conventional MR scanners are quite costly and large, whereas the compact mobile unilateral MR scanner cheap, easy to use and it has a definite potential in spectroscopic applications as well as imaging. These types of devices can be employed for non-destructive testing of small and bulky materials. It was desirable to improve the SNR of SPS so that the measurement results represent progress towards those of traditional scanners.

The thesis has constructed a single sided scanner based on an existing magnet design method [67]. The presence of inhomogeneous magnetic field in this type of system obscures measurement information. To overcome these problems this thesis proposed a combination of hardware and experimental techniques. This thesis contributes to a building unilateral NMR scanner through magnetic field profile analysis. As it was discussed in this paper early on, the 1D profile of SPS was extensively analyzed to help find the middle magnet height that will produce a larger relatively homogeneous field region above the RF coils. This thesis also contributes to designing NMR probe and building transmitter-receiver protection circuitry.

This thesis major contribution is designing a new composite pulse sequence for multi-frequency selective NMR excitation. Even though, as it was discussed in the background section various selective excitation techniques already exist, this thesis new sinusoidal composite pulse sequence works unlike any other method by shifting the resonance frequency much like in AM radio allowing excitation of narrow spectra at specific frequency. Along with this pulse sequence, a phase correction technique was

developed which allowed co-adding of spectral peaks, resulting in a significant SNR advantage over rectangular RF pulse. This pulse sequence was applied to examine spectral broadening due to diffusion.

This thesis also developed a new experimental technique that prove single sided NMR scanners are capable of performing high resolution imaging, the procedure presented various pulse length edge response plots and results indicate, as the pulse width increased the edge response plot got closer to the ideal image profile.

Other minor thesis contributions includes: creating software for 2D MR imaging, developing curve fitting method for edge response data, designing GUI interface for magnetic field measurement, developing software for data collection and processing.

## **5.2 Future work**

SNR and spatial resolution have an inverse relationship and the MR imaging system that attempts to improve spatial resolution may suffer from low SNR at some pulse width level. Therefore, the proposed imaging method can be applied to find the maximum achievable spatial resolution of single sided NMR devices. On the other hand the multi-frequency selective pulse sequence could be employed in spectroscopy measurements to observe time dependent phenomenon such as diffusion, transversal relaxation time, velocity measurements even possibly a chemical shift.

In theory, spectra could be much narrower if longer pulses were used; however there are some limiting factors. The section 4.2.5 experimental results indicate the multi-frequency pulse sequence produced high SNR outcome, nevertheless in section 4.2.6 we learned very long pulses generated broader spectra due to diffusion. These limitations

may be minimized by finding ways to enhance the sensitivity of the NMR probe and homogeneous field magnets, or even by experimenting with other magnet design setups.

During spectral analysis the custom made phase correction algorithm provided good solutions when the frequency shift multiplier  $n = 0, 1, 2 \dots 7$ , however as the number of frequency shift multiplier increased to 15 and 31 the algorithm have missed phase correcting few of the spectra; hence manual adjustment was needed to get the desired results, thereby steps could be taken to improve the phase correction technique.

## References

- [1] Estermann I., Simpson C. O. and Stern O. "The Magnetic Moment of the Proton," *Phys. Rev.*, 52, 535-545, 1937.
- [2] Rabi I. I., Millman S., P. Kusch P. and Zacharias J. R. "The Molecular Beam Resonance Method for Measuring Nuclear Magnetic Moments." *The Magnetic Moments of  $^3\text{Li}6$ ,  $^3\text{Li}7$  and  $^9\text{F}19$* , *Phys. Rev.*, 55, 526-535, 1939.
- [3] Purcell E. M., Torrey H. C. and Pound R. V. "Resonance Absorption by Nuclear Magnetic Moments in a Solid," *Phys. Rev.* 69, 37-38, 1946.
- [4] Bloch F. "Nuclear Induction," *Phys. Rev.*, 70, 460-474, 1946.
- [5] Shaw T. M., Elsken R. H. "NMR Absorption in Hygroscopic Materials," *Jour. Chem. Phys.*, 18, 1113, 1950.
- [6] Odebald E. and Lindstrom G. "Some preliminary observations on the proton magnetic resonance in biological samples," *Acta. Radiol.*, 43, 469-476, 1955.
- [7] Ernst R. R. and Anderson W. A. "Applications of Fourier transform spectroscopy to magnetic resonance," *Review of Scientific Instruments*, 37, 93-102, 1966.
- [8] Damadian R. "Tumour detection by nuclear magnetic resonance," *Science*, 171, 1151-1153, 1971.
- [9] Lauterbur P. C. "Image formation by induced local interactions." Examples employing nuclear magnetic resonance, *Nature*, 242, 190-191, 1973.
- [10] Mansfield P. and Grannell P. K. "NMR diffractions in solids," *Jour. Phys. C: Solid State Physics*, 6, L422-L426, 1973.
- [11] Slichter C. P. "Principles of Magnetic Resonance," Springer-Verlag Berlin Heidelberg, Third enlarged and updated edition, 1990.
- [12] DeGraaf A. Robin. "In vivo NMR spectroscopy: principles and techniques," John Wiley & sons Ltd, Second edition, 2007.
- [13] Claridge D.W. Timothy. "High resolution NMR techniques in organic chemistry," Elsevier Ltd, Tetrahedron organic chemistry series volume 19, 1999.
- [14] Gemmecker G. "Basic principles of FT NMR." Sensitivity, Lecture materials, 1999.
- [15] Van Dommelen L. "Fundamental Quantum Mechanics for Engineers," 2009.

- [16] Levitt M. H. "Spin dynamics." Basics of Nuclear Magnetic Resonance, John Wiley & Sons Inc., 2008.
- [17] Jacobsen N. E. "NMR Spectroscopy explained." Simplified theory, applications and examples for organic chemistry and structural biology, John Wiley & Sons Inc., pp. 292-294, 2007.
- [18] Carr H. Y. and Purcell E. M. "Effects of Diffusion on Free Precession in Nuclear Magnetic Resonance," Phys. Rev., 94, 630-638, 1954.
- [19] Bakhutov V. I. "Practical NMR Relaxation for chemists," John Wiley & Sons, Ltd, 2004.
- [20] Bloch F., Hansen W. W., and Packard M. E. "The Nuclear Induction Experiment," Phys. Rev., 70, 474-485, 1946.
- [21] Hahn E. L. "Free Nuclear Induction," Physics Today, 6, 1-9, 1953.
- [22] Hahn E. L. "Spin Echoes," Phys. Rev., 80, 580-594, 1950.
- [23] Meiboom S. and Gill D. "Modified Spin-Echo Method for Measuring Nuclear Relaxation Times," Rev. Sci. Instrum., 29, 668-691, 1958.
- [24] Prince W. S. "NMR studies of translational motion: principles and applications," Cambridge university press, 2009.
- [25] Tavel L., Guichard E. and Moreau C. "Annual reports on NMR spectroscopy." Contribution of NMR spectroscopy to flavor release and perception, Elsevier, 2008.
- [26] Singer J. R. "NMR diffusion and flow measurements and an introduction to spin phase graphing," J. Phys. E: Sci. Instrum., 11, 281-291, 1978.
- [27] Mackenzie K. J. D. and Smith M. E. "Multinuclear Solid-State NMR of inorganic materials, Elsevier, 2002.
- [28] Abraham R. J. and Mobli M. "Modelling <sup>1</sup>H NMR spectra of organic compounds: Theory, applications and NMR prediction software," John Wiley and Sons, Ltd, 2008.
- [29] Stejskal O. E. and Tanner J. E. "Spin diffusion measurements." spin echoes in presence of a time dependent field gradient, J. Chem. Phys., 42, 288-292, 1965.
- [30] Tanner J. E. "Use of the stimulated echo in NMR diffusion studies," J. Chem. Phys., 52, 2523-2526, 1970.

- [31] Callaghan P. T. Principles of Magnetic Resonance Microscopy, Oxford: Clarendon Press, 1991.
- [32] Rita D. G., Casanova F., Perlo J., Demco D. E. and Blümich B. "Self diffusion measurements by a mobile single sided NMR sensor with improved magnetic field gradient," Jour. of Mag. Res. 180, 229-235, 2006.
- [33] Klein M., Fechete R., Demco D. E. and Blümich B. "Self diffusion measurements by a constant relaxation method in strongly inhomogeneous magnetic fields," Jour. of Mag. Res., 164, 310-320, 2003.
- [34] Cohen Y., Avram L. and Frish L. "Diffusion NMR Spectroscopy in Supramolecular and Combinatorial Chemistry: An Old Parameter-New Insights," Wiley-VCH Verlag GmbH & Co. KGaA, Weinheim, 44, 520-554, 2005.
- [35] Wang P. C. and Chang S. J. "Nuclear magnetic resonance imaging of wood," Wood Fiber Sci., 18, 308-314, 1986.
- [36] Olson J. R., Chang S. J. and Wang P. C. "Nuclear magnetic resonance imaging." A non-invasive analysis of moisture distributions in white oak lumber, Canadian Journal of Forest Research, 20, 586-591, 1990.
- [37] Hall L. D. and Rajanayagam V. "Thin-Slice, Chemical-Shift Imaging of Oil and Water in Sandstone Rock at 80 MHz," Jour. Mag. Res., 74, 139-146, 1987.
- [38] Blackland S. and Mansfield P. "Diffusion in liquid-solid systems by NMR imaging," Jour. Phys. C: Solid State Phys., 19, L49-L52, 1986.
- [39] Rothwell W. P. and Vinegar H. J. "Petrophysical applications of NMR Imaging," Applied Optics, 24, 3969-3972, 1985.
- [40] Tipler P. "Physics for Scientists and Engineers: Electricity, Magnetism, Light, and Elementary Modern Physics," W. H. Freeman, 2004, 5th edition.
- [41] Blümich B. "NMR Imaging of Materials," Clarendon press, 2000.
- [42] Nishimura D. G. "Principles of Magnetic Resonance Imaging," Palo Alto: Stanford University Department of Electrical Engineering, 1996.
- [43] Filippi M., De Stefano N., Dousset V., and McGowan J. C. "MR Imaging in White Matter Diseases of the Brain and Spinal Cord," Springer:Verlag Berlin, 2005, pp. 16.
- [44] Atlas S. W. "Magnetic Resonance Imaging of the Brian and Spine," Lippincott Williams & Wilkins, 4<sup>th</sup> edition, Vol.2, 2009, pp. 152.

- [45] Casanova F., Perlo J., Blümich B. and Kremer K. "Multi-echo imaging in highly inhomogeneous magnetic fields," *Jour. of Mag. Res.*, 166, 76-81, 2004.
- [46] Zeeman P. On the influence of magnetism on the nature of the light emitted by a substance. *Astrophys. J.*, 5, 332, 1897.
- [47] Loudon G. M. "Organic Chemistry," Roberts and Co, 5<sup>th</sup> edition, 2009.
- [48] Lister T. and Renshaw J. "Essential A2 Chemistry," Nelson Thomas Ltd, 2004, pg. 59, 60.
- [49] Callaghan P. T. and Eccles C. D. "Sensitivity and resolution in NMR imaging," *Jour. Mag. Res.*, 71, 426-445, 1987.
- [50] Perlo J., Demas V., Casanova F., Meriles C. A., Reimer J., Pines A., Blümich B. "High-resolution spectroscopy with a portable single-sided sensor," *Sci.*, 308, 1279, 2005.
- [51] Johnson C.S., Jr. "Diffusion ordered nuclear magnetic resonance spectroscopy." principles and applications, *Prog. Nucl. Magn. Reson. Spectrosc.*, 34, 203–256, 1999.
- [52] Sigmund E. E. and Halperin W. P. "Hole-burning diffusion measurements in high magnetic field gradients," *Jour. of Mag. Res.* 163, 99-104, 2003.
- [53] Todica M. and Blümich B. "Hole-burning NMR in strongly inhomogeneous fields," *Solid State Nuclear Magnetic Resonance*, 32, 66–70, 2007.
- [54] Magee T., Shapiro M. and Williams D. "Comparison of High-Field-Strength Versus Low-Field-Strength MRI of the Shoulder," *American Roentgen Ray Society*, 181, 1211–1215, 2003.
- [55] Blümich B., Perlo J. and Casanova F. "Mobile single-sided NMR." *Progress in Nuclear Magnetic Resonance Spectroscopy*, 52, 197–269, 2008.
- [56] Prince J. L. and Links J. M. "Medical Imaging Signals and Systems," NJ: Pearson Education Inc. , 2006.
- [57] Barton F. E. II and Windham W. R. "Determination of acid detergent fibre and crude protein in forages by near infrared reflectance spectroscopy." Collaborative study, *Journal of the Association of Official Analytical Chemists*, 71, 1162-1167, 1988.

- [58] Hayes C. E., Edelstein W. A., Schenck J. F., Mueller O. M., and Eash M. "An efficient highly homogeneous radiofrequency coil for whole-body NMR imaging at 1.5T," *Jour. Magn. Reson.* 63, 622-628, 1985.
- [59] Doty F. D., Entzminger G. Jr., Hauck C. D., and Staab J. P. "Practical Aspects of Birdcage Coils," *Journal of Mag. Reson.* 138, 144-154, 1999.
- [60] Marble A. E. "Magnets for Unilateral Magnetic Resonance." PHD Thesis, The University of New Brunswick, April, 2007.
- [61] Ernst R. R. and Anderson W. A. "Application of Fourier Transform Spectroscopy to Magnetic Resonance," *Rev. Sci. Instrum.*, 37, 93-102, 1966.
- [62] Herrmann V., Unseld K., Fuchs H.- B. and Blümich B. "Molecular Dynamics of Elastomers investigated by DMTA and the NMR-MOUSE," *Colloid & Polymer Science*, 280, 758-764, 2002.
- [63] Todt H., Guthausen G., Burk W., Schmalbein D. and Kamlowski A. "Water/moisture and fat analysis by time-domain NMR," *Food chemistry*, vol. 96, issue 3, 436-440, 2006.
- [64] Hurlimann M. D., and Griffin D. D. "Spin dynamics of Carr-Purcell-Meiboom-Gill like sequences in grossly inhomogeneous  $B_0$  and  $B_1$  fields and application to NMR well logging," *Jour. of Mag. Res.*, 143, 120-135, 2000.
- [65] Samoilenko A. A., Artemov D. Y. and Sibeldina L. A. "Formation of sensitive layer in experiments on NMR subsurface imaging of solids," *JETP Letters*, 47, 417-419, 1988.
- [66] Benson T. B. and McDonald P. J. "Profile amplitude modulation in stray-field magnetic-resonance imaging," *Jour. of Mag. Res.*, A 112, 17-23, 1995.
- [67] McDonald P. J. "Stray field magnetic resonance imaging," *Progress in Nuclear Magnetic Resonance Spectroscopy*, 30, 69-99, 1997.
- [68] McDonald P. J. and Newling B. "Stray field magnetic resonance imaging," *Rep. Prog. Phys.*, 61, 1441-1493, 1998.
- [69] Godward J., Ciampi E., Cifelli M., and McDonald P. J. "Multidimensional Imaging Using Combined Stray Field and Pulsed Gradients," *Journal of Magnetic Resonance* 155, 92-99, 2002.
- [70] Eidmann G., Savelsberg R., Blumler P. and Blümich B. "The NMR MOUSE: A mobile universal surface explorer," *Jour. Mag. Res.*, A122, 104-109, 1996.

- [71] Perlo J., Casanova F. and Blümich B. “Ex situ NMR in highly homogeneous fields:  $^1\text{H}$  spectroscopy,” *Science*, 315, 1110-1112, 2007.
- [72] Perlo J., Casanova F., Blümich B. “Profiles with microscopic resolution by single sided NMR,” *J. Magn. Reson.*, 176, 64-70, 2005.
- [73] Freeman R. “Shaped radiofrequency pulses in high resolution NMR,” *Progress in Nuclear Magnetic Resonance Spectroscopy*, 32, 59-106, 1998.
- [74] Warren W. S. and Silver M. S. “The art of pulse crafting: applications to magnetic resonance and laser spectroscopy,” *Adv. Mag. Res.*, 12, 247-384, 1988.
- [75] Freeman R. “High resolution NMR using selective excitation,” *Journal of Molecular Structure*, 266, 39-51, 1992.
- [76] Alexander S. ”Spin-echo method for measuring relaxation times in two-line NMR spectra,” *Rev. Sci. Instrum.*, 32, 1066-1067, 1961.
- [77] Redfield A. G. and Gupta R. K. J. “Pulsed Fourier Transform NMR Spectrometer for use with H<sub>2</sub>O solutions,” *Chem. Phys.* 54, 1418-1419, 1971.
- [78] Tomlinson B. L. and Hill H. D. W. “Fourier synthesized excitation of nuclear magnetic resonance with application to homonuclear decoupling and solvent line suppression,” *Jour. Chem Phys.* 59, 1775-1784, 1973.
- [79] Morris G. A. and Freeman R. “Selective excitation in Fourier transform nuclear magnetic resonance,” *Jour. of Mag. Res.*, 29, 433-462, 1978.
- [80] Todica M., Fechete R. and Blümich B. “Selective NMR excitation in strongly inhomogeneous magnetic fields,” *Jour. of Mag. Res.*, 164, 220-227, 2003.
- [81] Blümich B., Gong Q., Byrne E. and Greferath M. “NMR with excitation modulated by Frank sequences,” *Jour. of Mag. Res.*, 199, 18–24, 2009.
- [82] Reichert D, Mizuno T., Takegoshi K., Terao T. “Narrowband Excitation of  $^2\text{H}$  Powder Pattern and Its Application to  $^2\text{H}$  1D Exchange Sample-Turning NMR,” *Jour. Magn. Reson.*, 139, 308-313, 1999.
- [83] Schick F. “Excitation of narrow frequency bands with reduced relaxation related signal losses: Methodology and preliminary application,” *Magnetic resonance Imaging*, 17, 527-536, 1999.
- [84] Bruker Optics. “The minispec TD-NMR Analyzers,” <http://www.brukeroptics.com/minispec.html?L=0>, Bruker Optik GmbH, 2011.
- [85] LakeShore. “Model 460 3-Channel Gaussmeter,” Lake Shore Cryotronics, Inc.

- [86] Marble A. E., Mastikhin I. V., Colpitts B. G. and Balcom B. J. "A compact magnet array with a remote homogeneous field," *Jour. of Mag. Res.*, 186, 100-104, 2007.
- [87] Fukushima E. and Roeder S. B. W. "Experimental Pulse NMR: A Nuts and Bolts Approach," Addison-Wesley, Reading, MA, 1981.
- [88] Bradshaw K. M. "Development of Magnetic Resonance Technology For Noninvasive Boron Quantification," EG&G Idaho, Inc., 1990.
- [89] Jones D. W. "Stepping Motor Types," The University of Iowa, Department of Computer Science, 1998.
- [90] User's Manual. "VXM Stepping Motor Controller," Velmex Inc., 2002.
- [91] Wolberg J. "Data Analysis Using the Method of Least Squares, Extracting the Most Information from Experiments," Springer-Verlag Berlin Heidelberg, 2006
- [92] Ledvij M. "Curve Fitting Made Easy," *Industrial Physicist*, 9, 24-27, 2003.
- [93] Thomsen J. S. "A Simple Graphical Method for Locating the Peak of a Lorentzian Curve," *Journal of Applied Physics*, vol. 37, 5004, 1966.
- [94] Department of chemistry and Biochemistry. "Nuclear Magnetic Resonance Spectroscopy," NMR Data Processing, The University of Arizona, [www.chem.arizona.edu/facilities/nmr/process.pdf](http://www.chem.arizona.edu/facilities/nmr/process.pdf).
- [95] Sotak C. H., Dumoulin C. L. and Newsham M. D. "Automatic phase correction of Fourier transform NMR spectra Based on the Dispersion versus Absorption (DISPA) line analysis," *Jour. of Mag. Res.*, 57, 453-462, 1984.
- [96] Cieslar C., Clore G. M. and Gronenborn A. M. "Automatic phasing of pure phase absorption two-dimensional NMR spectra," *Jour. Mag. Res.*, 79, 154-157, 1988.
- [97] Marshall A. G. and Roe D. C. "Dispersion versus Absorption." *Spectral Line Shape Analysis for RF and Microwave Spectroscopy*, *Anal. Chem.*, 50, 756-763, 1978.
- [98] Brown D. E. , Campbell T. W. and Moore R. N. "Automated Phase Correction of FT NMR Spectra by Baseline Optimization," *Jour. of Mag. Res.*, 85, 15-23, 1989.
- [99] Chen L., Weng Z., Goh L. Y. and Garland M. "An efficient algorithm for automatic phase correction of NMR spectra based on entropy minimization," *Jour. of Mag. Res.*, 158, 164-168, 2002.

- [100] De Brouwer H. "Evaluation of algorithms for automated phase correction of NMR spectra," *Jour. of Mag. Res.*, 201, 230-238, 2009.
- [101] Patt S. L. "Single and Multiple Frequency Shifted Laminar Pulses," *Jour. of magn. Reson.*, 96, 94-102, 1992.